# The ELECTROCHEMICAL ENGINEERING of ANODIC PEROXIDE PRODUCTION in Alkaline Water Electrolysis

Sohan A. Phadke

# The Electrochemical Engineering of Anodic Peroxide Production in Alkaline Water Electrolysis

## Dissertation

for the purpose of obtaining the degree of doctor
at Delft University of Technology
by the authority of the Rector Magnificus,
Prof. dr. ir. H. Bijl,
chair of the Board for Doctorates
to be defended publicly on
Wednesday, the 8th of July 2026, at 17:30

by

**Sohan Abhay PHADKE**

This dissertation has been approved by the promotors.

Composition of the doctoral committee:

| | |
|---|---|
| Rector Magnificus, | chairperson |
| Prof. dr. ir. W. de Jong, | Delft University of Technology, *promotor* |
| dr. ir. J. W. Haverkort, | Delft University of Technology, *promotor* |
| *Independent members:* | |
| Prof. dr. ir. A. Urakawa | Delft University of Technology |
| Prof. dr. G. Mul | University of Twente |
| Prof. dr. P. Pescarmona | University of Groningen |
| dr. ir. M. D. M. Pérez-Fortes | Delft University of Technology |
| Prof. dr. ir. J. T. Padding | Delft University of Technology, *reserve member* |

The work contained herein was funded by the NWO-AES Crossover program under project number 17621 (RELEASE).




*Keywords:* Anodic $H_2O_2$, Hydrogen Peroxide, Electrochemical Engineering, Green Hydrogen, Alkaline Water Electrolysis, Boron-Doped Diamond

*Printed by:* Ridderprint

*Cover by:* Sohan A. Phadke and Laura Bianca Donk



ISBN 978-94-6518-374-9
An electronic version of this dissertation is available at
https://repository.tudelft.nl/.

*“One of these days, thought Winston with sudden deep conviction, Syme will be vaporized. He is too intelligent. He sees too clearly and speaks too plainly. The Party does not like such people.”*

- George Orwell, *1984*

# CONTENTS


**Summary** ix

**Samenvatting** xiii

**Nomenclature** xix

**1 Introduction** 1
- 1.1 Motivation . . . 1
  - 1.1.1 The Need for Sustainable Chemicals Production . . . 1
  - 1.1.2 Alkaline Water Electrolysis for $H_2$ Production . . . 1
  - 1.1.3 Lowering the Levelized Cost of $H_2$ . . . 3
  - 1.1.4 Anodically Produced $H_2O_2$ . . . 3
- 1.2 Background . . . 4
  - 1.2.1 Electrochemistry of Anodically Produced $H_2O_2$ . . . 4
  - 1.2.2 Electrochemical Engineering of Anodic $H_2O_2$ . . . 6
- 1.3 Aims and Outline . . . 9

**2 Practical Limitations in Generating Hydrogen Peroxide** 11
- 2.1 Introduction . . . 12
- 2.2 Methods . . . 13
  - 2.2.1 Experimental Setup . . . 13
  - 2.2.2 Experimental Measurement . . . 16
  - 2.2.3 Numerical Model Development . . . 17
- 2.3 Results and Discussion . . . 21
  - 2.3.1 Experimental-Simulation Agreement . . . 21
  - 2.3.2 Simulation Results for Electrolyte Depletion . . . 22
  - 2.3.3 $H_2O_2$ Formation . . . 25
  - 2.3.4 Gaseous $CO_2$ Evolution . . . 26
  - 2.3.5 Considerations for Scale-Up . . . 27
- 2.4 Conclusion . . . 28
- 2.A Appendix - Additional Simulation Results . . . 29
  - 2.A.1 Reservoir Volumes . . . 29
  - 2.A.2 Current Breakdown by Reaction . . . 29
  - 2.A.3 Reservoir Concentrations . . . 30
  - 2.A.4 Mesh Refinement Study . . . 30
  - 2.A.5 Current Profiles Without $CO_2$ Stripping . . . 31
- 2.B Appendix - Simulation Details . . . 34
  - 2.B.1 Model Geometry and Operating Parameters . . . 34

2.B.2 Model Homogeneous Reaction Kinetics . . . 34
2.B.3 Model Initial Concentrations . . . 36
2.B.4 Model Electrochemistry . . . 36
2.B.5 Model Species Transport . . . 37
2.B.6 Model $CO_2$ Stripping . . . 40

**3 Accumulating Hydrogen Peroxide at Laboratory Scale 43**
3.1 Introduction . . . 44
3.2 Analytical Model for $H_2O_2$ Accumulation . . . 45
3.2.1 List of Symbols . . . 45
3.2.2 Mole Balance Equations . . . 46
3.2.3 Assumptions . . . 47
3.2.4 Solutions . . . 48
3.3 Methods . . . 49
3.3.1 Materials . . . 49
3.3.2 $H_2O_2$ Quantification . . . 50
3.3.3 Determination of Generation Rate, $S$ . . . 51
3.3.4 Determination of Bulk Disproportionation Rate Constant, $k_b$ . . . 52
3.3.5 Numerical Fitting of Anodic Decomposition Rate Constant, $k_a$ 52
3.4 Results and Discussion . . . 53
3.4.1 $H_2O_2$ Generation Values . . . 53
3.4.2 $H_2O_2$ Loss via Bulk Disproportionation . . . 53
3.4.3 Full System - Fitting Data to Find $k_a$ . . . 53
3.4.4 Exclusion of Crossover Effects . . . 55
3.4.5 Extension to Literature Data . . . 56
3.4.6 Model Validation and Implications for Scaled-Up Operation . . . 57
3.5 Conclusions . . . 61
3.A Appendix - Low Flow Rate Solution to Analytical Model . . . 63
3.B Appendix - High Flow Rate Justification . . . 64

**4 Process Design to Separate and Sell Hydrogen Peroxide 65**
4.1 Introduction . . . 66
4.2 Process Design . . . 68
4.2.1 Co-production of $H_2O_2$ and $H_2$ in the Electrolyzer . . . 68
4.2.2 Electrolyzer Structure . . . 69
4.2.3 $H_2$ Separation . . . 70
4.2.4 Challenges in $H_2O_2$ Separation . . . 70
4.2.5 Design Basis and Assumptions . . . 70
4.2.6 Valorization of Hydrogen Peroxide to Sodium Percarbonate . . . 71
4.2.7 Excess Water Removal . . . 71
4.2.8 Adjustment of pH . . . 72
4.2.9 Excess Sodium Carbonate Removal . . . 72
4.2.10 Sodium Percarbonate Formation and Crystallization . . . 73
4.3 Techno-economics . . . 73
4.4 Sensitivity Analysis . . . 77
4.4.1 Breakeven Point Analysis . . . 78

4.4.2 IRR and NPV Analyses . . . 79
4.4.3 Overview of the Sensitivity Analysis . . . 82
4.5 Multi-Parameter Sensitivity Analysis . . . 83
4.5.1 Effect of Changing Faradaic Efficiency and SPC Price . . . 83
4.5.2 Effect of Changing Anode Price and SPC Price . . . 83
4.5.3 Effect of Changing Anode Price and Faradaic Efficiency . . . 85
4.5.4 Overview of the Multi-Parameter Sensitivity Analysis . . . 86
4.5.5 Scenarios' Likelihood Evaluation . . . 86
4.6 Conclusions . . . 87
4.A Appendix - Process Design Details . . . 89

**5 Concluding Remarks** **95**
5.1 Conclusions . . . 95
5.2 Recommendations . . . 97

**Bibliography** **99**

**Acknowledgements** **113**

**Curriculum Vitæ** **117**

**List of Publications** **119**

# SUMMARY

With increasing climatic changes due to greenhouse gas accumulation, there is an urgent need for sustainability improvements across many sectors of society, including chemicals manufacturing. One ubiquitous chemical feedstock in need of a cleaner production method is hydrogen ($H_2$), commonly produced by the environmentally unfriendly steam-methane reforming reaction. The production of $H_2$ could be made far more sustainable by instead using alkaline water electrolysis powered by renewable energy, but the process economics are unfavorable, with so-called "green" hydrogen from water electrolysis costing much more than less sustainable "gray" hydrogen. The majority of the costs of green hydrogen arise from the balance of plant surrounding the electrolyzer, and recent research has made only incremental progress in improving the efficiency of either the balance of plant or the electrolyzer itself. Driving down the cost of green hydrogen will require a more innovative approach. Electrolysis splits water into high-value $H_2$ but also low-value oxygen ($O_2$). A creative approach to lowering costs would be to replace the anodic reaction producing low-value $O_2$ with a reaction to produce high-value hydrogen peroxide ($H_2O_2$). The $H_2O_2$ could then be separated and sold, offsetting the higher cost of the green hydrogen produced at the cathode. This method of paired electrolysis to simultaneously produce $H_2$ and $H_2O_2$ has been the subject of much study with respect to its electrochemistry, but very little with regards to the electrochemical engineering. If we are to scale this reaction and offset the cost of green hydrogen by co-production of a valuable side product, we also need to understand the electrochemical engineering of the reaction, from the scale of operational devices to the complete process plant.

This dissertation begins by addressing the frequently overlooked problem of anodic species depletion when using (bi)carbonate electrolyte. Because $H_2O_2$ appears to have higher production rates and to be more stable in (bi)carbonate solutions rather than 30 wt% KOH solutions, most studies in literature use (bi)carbonate-based electrolytes. But due to the lower conductivity of (bi)carbonate electrolyte, the hydroxide ($OH^-$) anion flux from cathode to anode is too low, and this leads to dramatic changes in pH and conductivity across the separator as electrolysis continues. At lab-scale, this issue is sometimes side-stepped by flowing fresh electrolyte past the anode, or is delayed by simply using a large excess of anolyte volume. But industrial processes typically run with recirculating flows and using too much anolyte volume dilutes the produced $H_2O_2$. Therefore, we examined ion transport and electrolyte depletion in (bi)carbonate electrolytes through experiments and simulations in an industrially relevant case. We found that the transport rate of $OH^-$ anions through the separator is severely limiting, leading to the carbonate equilibrium shifting in the anolyte to provide $OH^-$ reactant. The first equilibrium shift from carbonate

to bicarbonate occurs readily, but the second shift from bicarbonate to carbon dioxide ($CO_2$) is mediated by the physical gas stripping of dissolved $CO_2$ by oxygen bubbles generated at the anode. This "active" removal of $CO_2$ is what allows the system to continue depleting reactants. While the anolyte is depleting, the current through the system is steadily dropping, lowering the yield of both $H_2$ and $H_2O_2$. Before the anolyte was fully depleted and a limiting current value was reached, the experiments were stopped due to electro-osmotic flow causing a significant loss of anolyte volume. The changing pH levels, changing conductivities, and changing volumes would all significantly affect any scaled-up process and must be accounted for.

Next, we show results of operating a setup with the specific focus of producing $H_2O_2$ in an industrially relevant manner, meaning we used recirculating electrolyte, high electrolyte flow rates, maintenance of anolyte pH, and the introduction of sodium silicate ($Na_2SiO_3$) as a chemical stabilizer for $H_2O_2$. The $H_2O_2$ concentration profiles over time begin by linearly increasing and then leveling off to a steady state value, a result consistent with a stable generation process in competition with concentration-dependent decomposition. An analytical model was formulated using mole balances with descriptions of the three key reactions of $H_2O_2$ generation, $H_2O_2$ decomposition at the anode, and $H_2O_2$ decomposition in the bulk. Straightforward experimentation was used to find the generation rate at different current densities and the bulk decomposition rate constant in electrolyte. The final decomposition rate constant was then fitted to experimental results using the derived analytical expressions. In our experimental setup, the anodic decomposition was always found to be the dominant loss mechanism compared to bulk decomposition, and was also shown to be a significant term in other works from literature. The analytical equations were then used to make predictions about scaling up such a system, which show expected results, such as that a decrease in anolyte volume will lead to higher $H_2O_2$ steady state concentrations achieved more quickly. But the analytical equations also showed a somewhat surprising result that using large volumes of anolyte, despite the lower steady state concentrations reached at longer times, actually produce more moles of $H_2O_2$ overall. Thus, the final operational mode will be a trade-off between desired concentration, overall production rates, the capital costs of larger reservoirs, the operating costs of running electrolysis for a longer time, and all of these eventual effects on downstream separation.

With a better understanding of how the electrolyzer works to produce anodic $H_2O_2$, the separation and sale of $H_2O_2$ can be studied at the scale of a commercial factory. As it is challenging to separate the electrolyte anions from the $H_2O_2$ in solution, we designed a process to convert the anodic $H_2O_2$ to sodium percarbonate ($Na_2CO_3 \cdot 1.5\,H_2O_2$). The process was then studied in detail through a techno-economic evaluation. The process design involves first recirculating anolyte during electrolysis to reach a sufficient concentration, then removing large quantities of water, and finally exchanging most of the carbonate for chloride to crystallize out sodium percarbonate. The remaining solution is then treated and recycled back to the reservoir for further electrolysis. Techno-economic analysis revealed that the process on a 2 MW electrolyzer basis is highly unprofitable, losing over 15 M€ per

year. Single parameter sensitivity analyses revealed that faradaic efficiency, anode cost, and sodium percarbonate sale price had a large impact on the breakeven point that would allow the process to be profitable. In particular, favorable changes in any two of the these three parameters were shown to dramatically improve the process economics, and the work provides clear targets for anode material design, such as anode cost and faradaic efficiency.

The combined body of work in this dissertation indicates both limitations and considerations for scaling up the electrochemical reaction of water oxidation to $H_2O_2$. While there may be promise, the electrochemical engineering of these systems will require more careful study and advancements in technologies to become cost-competitive with traditional hydrogen and sodium percarbonate manufacturing methods.

# SAMENVATTING

Met de toenemende klimaatverandering als gevolg van de ophoping van broeikasgassen is er een dringende behoefte aan verbeteringen ten aanzien van duurzame ontwikkeling in veel sectoren van de samenleving, waaronder de chemische industrie. Een alomtegenwoordige chemische grondstof die een schonere productiemethode nodig heeft, is waterstof ($H_2$), dat doorgaans wordt geproduceerd via de milieubelastende stoomreforming van methaan. De productie van $H_2$ kan veel duurzamer worden door gebruik te maken van alkalische waterelektrolyse aangedreven door hernieuwbare energie, maar de proceseconomie is ongunstig: zogenoemde "groene" waterstof uit waterelektrolyse kost aanzienlijk meer dan de minder duurzame "grijze" waterstof. Het grootste deel van de kosten van groene waterstof komt voort uit de totale procesinstallatie rond de elektrolyser, en recent onderzoek heeft slechts incrementele vooruitgang geboekt in het verbeteren van de efficiëntie van zowel de totale procesinstallatie als de elektrolyser zelf. Het verlagen van de kosten van groene waterstof vereist een innovatievere aanpak. Elektrolyse splitst water in hoogwaardig $H_2$ maar ook in laagwaardig zuurstof ($O_2$). Een creatieve manier om de kosten te verlagen is het vervangen van de anodereactie, welke laagwaardig $O_2$ produceert, door een reactie die hoogwaardig waterstofperoxide ($H_2O_2$) produceert. De $H_2O_2$ kan vervolgens worden gescheiden en verkocht, waardoor de hogere kosten van de groene waterstof, die aan de kathode wordt geproduceerd, kunnen worden gecompenseerd. Deze methode van gekoppelde elektrolyse om gelijktijdig $H_2$ en $H_2O_2$ te produceren is uitgebreid bestudeerd vanuit elektrochemisch perspectief, maar nauwelijks vanuit de optiek van elektrochemische techniek. Als we deze reactie willen opschalen en de kosten van groene waterstof willen compenseren door coproductie van een waardevol bijproduct, moeten we ook de elektrochemische techniek van de reactie begrijpen, van het niveau van operationele apparaten tot aan de volledige procesinstallatie.

Deze dissertatie begint met het aanpakken van het vaak over het hoofd geziene probleem van anodische elektrolietuitputting bij gebruik van (bi)carbonaatelektroliet. Omdat $H_2O_2$ hogere productiesnelheden lijkt te hebben en stabieler is in (bi)carbonaatoplossingen dan in dertig gewichtsprocent KOH-oplossingen, gebruiken de meeste studies in de literatuur (bi)carbonaatgebaseerde elektrolieten. Maar door de lagere geleidbaarheid van (bi)carbonaatelektroliet is de flux van hydroxide anionen ($OH^-$) van de kathode naar de anode te laag, wat leidt tot sterke veranderingen in de pH en de geleidbaarheid over het diaphragma gedurende de elektrolyse. Op labschaal wordt dit probleem soms omzeild door vers elektroliet langs de anode te laten stromen, of wordt het uitgesteld door simpelweg een groot overschot aan anolietvolume te gebruiken. Industriële processen werken echter doorgaans met recirculerende stromen, en een te groot anolietvolume verdunt het geproduceerde

$H_2O_2$. Daarom onderzochten wij het ionentransport en de uitputting van elektroliet in (bi)carbonaatelektrolieten middels experimenten en simulaties in een industrieel relevante situatie. We ontdekten dat de transportsnelheid van $OH^-$ anionen door het diaphragma sterk beperkend is, waardoor het carbonaatevenwicht in het anoliet verschuift om $OH^-$ reactant te leveren. De eerste evenwichtsverschuiving van carbonaat naar bicarbonaat verloopt gemakkelijk, maar de tweede verschuiving van bicarbonaat naar kooldioxide ($CO_2$) wordt gefaciliteerd door het fysische strippen van opgelost $CO_2$ door zuurstofbellen die aan de anode worden gevormd. Deze “actieve” verwijdering van $CO_2$ maakt het mogelijk dat het systeem reactanten blijft uitputten. Terwijl het anoliet uitgeput raakt, daalt de stroom door het systeem gestaag, waardoor de opbrengst van zowel $H_2$ als $H_2O_2$ afneemt. Voordat het anoliet volledig was uitgeput en de limiterende stroomdichtheid werd bereikt, werden de experimenten gestopt vanwege elektro osmotische stroming die leidde tot een aanzienlijk volumeverlies van het anoliet. De veranderende pH waarden, veranderende geleidbaarheden en veranderende volumes zouden allemaal een grote invloed hebben op een opgeschaald proces en moeten worden meegenomen in het ontwerp.

Vervolgens tonen we de resultaten van een opstelling die specifiek gericht is op het produceren van $H_2O_2$ op een industrieel relevante manier, wat betekent dat we recirculerend elektroliet gebruikten, hoge elektrolietdebieten, handhaving van de anoliet pH en de toevoeging van natriumsilicaat ($Na_2SiO_3$) als chemische stabilisator voor $H_2O_2$. De $H_2O_2$ concentratieprofielen in de tijd beginnen lineair toe te nemen en vlakken vervolgens af tot een stationaire waarde, een resultaat dat consistent is met een stabiel generatieproces in competitie met concentratie afhankelijke ontleding. Een analytisch model werd opgesteld op basis van molbalansen met beschrijvingen van de drie belangrijkstereacties: $H_2O_2$ vorming, anodische ontleding van $H_2O_2$ en bulkontleding van $H_2O_2$. Eenvoudige experimenten werden gebruikt om de productiesnelheid bij verschillende stroomdichtheden en de snelheidsconstante van de bulkontleding in elektroliet te bepalen. De uiteindelijke snelheidsconstante van de ontleding werd vervolgens gefit aan experimentele resultaten met behulp van de afgeleide analytische vergelijkingen. In onze experimentele opstelling bleek de anodische ontleding altijd het dominante verliesmechanisme te zijn vergeleken met bulkontleding, en dit werd ook bevestigd in andere literatuur. De analytische vergelijkingen werden vervolgens gebruikt om voorspellingen te doen over opschaling van een dergelijk systeem. Deze voorspellingen laten verwachte resultaten zien, zoals dat een afname van het anolietvolume leidt tot hogere stationaire $H_2O_2$ concentraties die sneller worden bereikt. Maar de analytische vergelijkingen lieten ook een enigszins verrassend resultaat zien: het gebruik van grote anolietvolumes produceert, ondanks lagere stationaire concentraties en langere procestijden, uiteindelijk méér mol $H_2O_2$ in totaal. De uiteindelijke operationele modus zal dus een afweging zijn tussen gewenste concentratie, totale productiehoeveelheid, kapitaalkosten van grotere reservoirs, operationele kosten van langere elektrolyseduur en de effecten hiervan op downstream scheiding.

Met een beter begrip van hoe de elektrolyser anodisch $H_2O_2$ produceert, kan de scheiding en verkoop van $H_2O_2$ worden bestudeerd op de schaal van een com-

merciële fabriek. Omdat het lastig is om elektrolietanionen te scheiden van $H_2O_2$ in oplossing, ontwierpen we een proces om het anodisch gevormde $H_2O_2$ om te zetten in natriumpercarbonaat ($Na_2CO_3 \cdot 1.5\,H_2O_2$). Het proces werd vervolgens in detail onderzocht middels een techno-economische evaluatie. Het procesontwerp omvat eerst het recirculeren van anoliet tijdens elektrolyse tot een voldoende hoge concentratie is bereikt, vervolgens het verwijderen van grote hoeveelheden water, en ten slotte het uitwisselen van het grootste deel van het carbonaat voor chloride om natriumpercarbonaat te kristalliseren. De resterende oplossing wordt vervolgens behandeld en teruggevoerd naar het reservoir voor verdere elektrolyse. Techno-economische analyse toonde aan dat het proces, gebaseerd op een 2 MW elektrolyser, sterk verliesgevend is, met meer dan 15 miljoen euro verlies per jaar. Gevoeligheidsanalyses met steeds één parameter lieten zien dat Faraday efficientie, anodekosten en de verkoopprijs van natriumpercarbonaat een grote invloed hebben op het omslagpunt waarop het proces winstgevend zou kunnen worden. Vooral gunstige veranderingen in twee van deze drie parameters bleken de proceseconomie drastisch te verbeteren, en het werk biedt duidelijke doelen voor het ontwerp van anodematerialen, zoals anodekosten en Faraday efficiëntie.

Het geheel van dit onderzoek laat zowel beperkingen als aandachtspunten zien voor het opschalen van de elektrochemische reactie van wateroxidatie tot $H_2O_2$. Hoewel er potentie is, vereist de elektrochemische techniek van deze systemen verdere zorgvuldige studie en technologische vooruitgang om kostentechnisch te kunnen concurreren met traditionele methoden voor de productie van waterstof en natriumpercarbonaat.

# NOMENCLATURE

**Physical Constants**

| | |
|---|---|
| $\epsilon_0$ | Permittivity of free space ($8.5\times10^{-12}$ F $m^{-1}$) |
| $\mathcal{F}$ | Faraday's constant (96485 C $mol^{-1}$) |
| $g$ | Acceleration of gravity (9.8 m $s^{-2}$) |
| $R$ | Ideal gas constant (8.314 J $mol^{-1}$ $K^{-1}$) |
| $\mathcal{V}_m$ | Molar volume at 298.15 K and 1 bar (0.02479 $m^3$ $mol^{-1}$) |

**Dimensionless Numbers**

| | |
|---|---|
| Re | Reynolds number (-) |
| Sc | Schmidt number (-) |
| Sh | Sherwood number (-) |

**Greek Variables and Parameters**

| | |
|---|---|
| $\alpha_a$ | Anodic charge transfer coefficient (-) |
| $\alpha_c$ | Cathodic charge transfer coefficient (-) |
| $\varepsilon$ | Porosity (-) |
| $\epsilon_r$ | Relative permittivity (-) |
| $\zeta$ | Zeta potential (V) |
| $\eta$ | Overpotential (V) |
| $\mu$ | Electrolyte viscosity (Pa s) |
| $\mu_i$ | Electrical mobility of species $i$ ($m^2$ $V^{-1}$ $s^{-1}$) |
| $\nu_i$ | Stoichiometric ratio of species $i$ (-) |
| $\xi$ | Extent of reaction (-) |
| $\rho$ | Density (kg $m^{-3}$) |
| $\phi$ | Electrolyte potential (V) |

**Italicized Variables and Parameters**

| | |
|---|---|
| $A_{Elec}$ | Geometric electrode area ($m^2$) |
| $A_{Res}$ | Reservoir-Atmosphere interface area ($m^2$) |
| $A_{Sep}$ | Geometric separator area ($m^2$) |
| $a_g$ | Surface area to volume ratio for gas ($m^{-1}$) |
| $c_i$ | Concentration of species $i$ in the separator (mol $m^{-3}$) |
| $D_i$ | Molecular diffusivity of species $i$ ($m^2$ $s^{-1}$) |
| $D_{Eff,i}$ | Effective diffusion coefficient of species $i$ ($m^2$ $s^{-1}$) |
| $d_b$ | Gas bubble diameter (m) |
| $E$ | Electrode potential (V vs SHE) |
| $E_{eq,\ ref}$ | Equilibrium reference potential (V vs SHE) |
| $j$ | Current density (A $m^{-2}$) |
| $j_0$ | Exchange current density (A $m^{-2}$) |
| $k_a$ | $H_2O_2$ anodic decomposition rate constant (m $s^{-1}$) |
| $k_b$ | $H_2O_2$ bulk disproportionation rate constant ($s^{-1}$) |
| $k_k$ | Forward reaction rate constant of reaction $k$ ($s^{-1}$) |
| $k_{-k}$ | Forward reaction rate constant of reaction $k$ ($m^3$ $s^{-1}$ $mol^{-1}$) |
| $k_l$ | Mass transfer coefficient (m $s^{-1}$) |
| $L_{Sep}$ | Separator length (m) |
| $l_x$ | Electrode chamber thickness (m) |
| $l_y$ | Electrode chamber width (m) |
| $l_z$ | Electrode chamber height (m) |
| $\mathcal{M}$ | Electro-osmotic mobility ($m^2$ $V^{-1}$ $s^{-1}$) |
| $N_{B,i}$ | Boundary flux of species $i$ (mol $m^{-2}$ $s^{-1}$) |
| $N_{C,i}$ | Convective flux of species $i$ (mol $m^{-2}$ $s^{-1}$) |
| $N_{D,i}$ | Diffusive flux of species $i$ (mol $m^{-2}$ $s^{-1}$) |
| $N_{M,i}$ | Migratory flux of species $i$ (mol $m^{-2}$ $s^{-1}$) |
| $\dot{n}$ | Molar rate (mol $s^{-1}$) |

| | |
|---|---|
| $n_{Res,i}$ | Amount of species $i$ in the reservoir (mol) |
| $\dot{Q}$ | Volumetric flow rate ($m^3\ s^{-1}$) |
| $R$ | Resistance (Ω) |
| $r_i$ | Reaction rate involving species $i$ (mol $m^{-3}\ s^{-1}$) |
| $S$ | $H_2O_2$ generation rate (mol $s^{-1}\ m^{-2}$) |
| $T$ | Temperature (K) |
| $t$ | Time (s) |
| $u$ | Electro-osmotic velocity (m $s^{-1}$) |
| $V$ | Volume ($m^3$) |
| $W_l$ | Vertical liquid velocity (m $s^{-1}$) |
| $w_S$ | Stokes rise velocity (m $s^{-1}$) |
| $z_c$ | Critical electrode height (m) |
| $z_i$ | Ionic charge of species $i$, (-) |

**Upright Variables and Parameters**

| | |
|---|---|
| $FE_{H_2O_2}$ | Faradaic Efficiency to $H_2O_2$ (%) |
| $K_{eq,\,k}$ | Acid dissociation constant of reaction $k$ (mol $m^{-3}$) |
| n | Ratio of electrons per molecule (-) |
| pKa | Negative logarithm of the acid dissociation constant (-) |

**Abbreviations and Initialisms**

| | |
|---|---|
| BDD | Boron-Doped Diamond |
| CAPEX | Capital Expenditure (€) |
| IRR | Internal Rate of Return (%) |
| NPV | Net Present Value (€) |
| OPEX | Operational Expenditure (€) |
| ORR | Oxygen Reduction Reaction |
| SPC | Sodium Percarbonate ($Na_2CO_3 \cdot 1.5\,H_2O_2$) |
| TMC | Total Manufacturing Costs (€) |
| WOR | Water Oxidation Reaction |

# 1

# INTRODUCTION

## 1.1. MOTIVATION

### 1.1.1. THE NEED FOR SUSTAINABLE CHEMICALS PRODUCTION

The impact of climate change has been emphasized in recent years as rising sea levels, more frequent severe storms, and increases in temperature have been recorded across the planet. [1] These climatic changes are driven in large part by the accumulation of greenhouse gases such as carbon dioxide ($CO_2$) in the atmosphere. Over 50% of these greenhouse gas emissions are a result of electricity generation, heat production, and industrial usage. [2] Within industrial usage, the production of bulk materials such as steel, cement, and primary chemicals represents a significant portion of $CO_2$ emissions, with the production of methanol and ammonia alone accounting for 1.8% of global energy-related $CO_2$ emissions. [3, 4] These products require hydrogen gas ($H_2$) as a feedstock. [5]

Unfortunately, the production of $H_2$ is a major emitter of $CO_2$, because the vast majority of $H_2$ is produced by the water-gas shift reaction in steam methane reforming (SMR). This reaction uses natural gas and high temperature steam to produce $H_2$, with $CO_2$ as a byproduct that is often not captured or stored. It therefore requires direct use of fossil fuels and high energy input while simultaneously emitting greenhouse gases. Of the nearly 100 Mt of $H_2$ produced in 2024, 85% was produced from fossil fuels with no $CO_2$ mitigation and another 15% was produced as a byproduct from industrial processes. Less than 1% of $H_2$ was produced from low-emissions sources. [6] As a result, around 700 Mt of direct $CO_2$ emissions in 2024 were a result of $H_2$ production in industry, which is approximately equivalent to the total greenhouse gas emissions of Mexico. [7] In order to combat climate change, it is crucial that we find a sustainable alternative for this method of $H_2$ production.

### 1.1.2. ALKALINE WATER ELECTROLYSIS FOR $H_2$ PRODUCTION

A sustainable technology already exists to produce $H_2$ with practically zero greenhouse gas emissions. It is called water electrolysis, and involves using electrical power from renewable sources to split water into $H_2$ gas and oxygen ($O_2$) gas, as

depicted in Figure 1.1. When a potential difference is applied between the cathode and anode, two simultaneous chemical reactions occur. If performed in an alkaline medium, the first reaction is the reduction of water to $H_2$ and hydroxide ($OH^-$) anions. These anions transport through an aqueous salt solution, called the electrolyte, to the anode. At the anode, these $OH^-$ anions are oxidized to form $O_2$, releasing electrons to complete the circuit. When the electrolyte solution between the cathode and anode is a high pH solution, the process is referred to as alkaline water electrolysis.

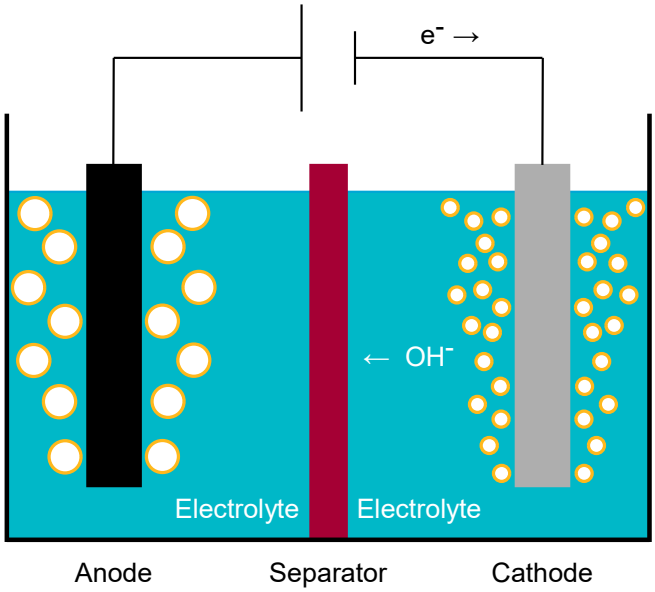


Figure 1.1: A simplified schematic of an alkaline water electrolyzer system. Electrons are transferred at the cathode where water is reduced to $H_2$ bubbles and $OH^-$ anions. These anions are transported from the cathode to the anode, where they are oxidized to form $O_2$ bubbles. The electrons released in this reaction close the circuit. A separator material is often used between the two compartments to allow $OH^-$ transport but prevent the gases from mixing and forming an explosive mixture.

A porous separator or membrane is often placed between the electrodes to prevent the mixing of $H_2$ and $O_2$ gas, which would otherwise lead to an explosion. The most commonly used porous separator in alkaline water electrolysis is Zirfon Perl UTP 500, which is a mixture of polysulfone and zirconia nanoparticles. Some examples of membranes include Nafion 117, Sustainion and Fumasep. These membranes are typically polymeric backbones with ionic functional groups that repel ions of the same charge as the functional group. For example, Nafion 117 has sulfonate groups ($SO_3^-$) which inhibit the transfer of anions across the membrane. Sustainion and Fumasep have different positively charged functional groups which inhibit the

transfer of cations across the membrane.

The technology of alkaline water electrolysis, which is the focus of this dissertation, was already commercialized over a hundred years ago by companies such as Norsk Hydro. [8] However, the cost of the $H_2$ produced this way could not compete with the (then) newly developed water-gas shift reaction, and so fell out of use. With the focus on reducing greenhouse gas emissions in the chemical industry, alkaline water electrolysis powered by renewable energy to produce so-called "green hydrogen" has regained significant interest.

### 1.1.3. LOWERING THE LEVELIZED COST OF $H_2$

Despite growing interest in green hydrogen, it is still nowhere near cost-competitive with the SMR process, with green hydrogen often selling for five to ten times the price of so-called "gray hydrogen" from SMR. [9] The overall price of $H_2$, when accounting for the complete scope of production, is referred to as the levelized cost of hydrogen. This is the minimum sale price of $H_2$ that must be set in order to recoup all capital expenses and operating costs. At the start of the decade, there was a wave of funding announced to promote research with the aim of dramatically lowering the levelized cost of green $H_2$ to \$1 or €1 per kg of $H_2$. [10, 11] But after some years of research into conventional alkaline water electrolysis using advanced materials or novel device geometries to improve the efficiency of the process, that progress has yielded only small improvements. It has even been shown that the most significant portion of the cost of green $H_2$ comes not from the electrolyzer itself, but from the surrounding equipment of the entire chemical plant, meaning that there are limits to how much the levelized cost of hydrogen can be reduced by improving alkaline water electrolysis alone. [10] We need to think more creatively in order to break past these limits.

Rather than attempting to lower the levelized cost of hydrogen of the existing process, a more innovative approach is actually to examine the other product of alkaline water electrolysis. The $O_2$ that is produced at the anode is a very low value product, and is often simply vented away as it is not worth capturing and selling. This anodic reaction represents an opportunity for changing standard alkaline water electrolysis into something potentially more economically viable. Replacing the $O_2$ product with something more valuable, then separating and selling that product, could be a pathway to lowering the cost of green $H_2$ from alkaline water electrolysis. This so-called "paired electrolysis" principle has been gaining interest in recent years for precisely this reason, that the electrolyzer could now form two valuable products instead of only one. A promising option for valuable anodic products is hydrogen peroxide ($H_2O_2$).

### 1.1.4. ANODICALLY PRODUCED $H_2O_2$

$H_2O_2$ is a highly valued commodity chemical for its use as a green oxidant, meaning that it can oxidize a substance while leaving behind exclusively water as a byproduct. $H_2O_2$ is already commonly used as an oxidant in industries such as textile processing and paper milling. [12] Similarly to $H_2$, the current industrially

practiced method of $H_2O_2$ production by anthraquinone oxidation is environmentally unfriendly. The catalytic process requires high energy inputs and a large amount of chemical solvents. [13] These high energy inputs and the need for safe disposal of organic solvents contribute to greenhouse gas emissions. As such, the production of $H_2O_2$ is also in need of a green production method. We can achieve the aims of cleaner chemical production methods for $H_2$ and $H_2O_2$ in one process by modifying a typical alkaline water electrolyzer to simultaneously produce $H_2$ and $H_2O_2$. The sale of the green $H_2O_2$ produced at the anode could then be used to offset the high levelized cost of hydrogen from typical alkaline water electrolysis and make green $H_2$ more commercially attractive.

There have already been studies of the simultaneous production of $H_2$ and $H_2O_2$ in water electrolysis, but they are mostly focused on fundamental aspects. [14–16] These studies examine the system from an electrochemist's point of view, and explore concepts such as which anode materials preferentially produce $H_2O_2$ instead of $O_2$, what the reaction mechanism to produce $H_2O_2$ is, and how the electrochemical surface behaves. Missing from the overall discussion is the viewpoint of an electrochemical engineer. The questions that need addressing are what production rates of $H_2O_2$ can be achieved, how can this $H_2O_2$ be extracted for sale, and how well could this process lower the levelized cost of hydrogen?

## 1.2. Background

### 1.2.1. Electrochemistry of anodically produced $H_2O_2$

The half-cell reactions that take place in typical alkaline water electrolysis at the cathode and anode are shown in Equations (1.1) and (1.2), respectively. The latter is sometimes referred to as the four-electron water oxidation reaction (4 $e^-$ WOR), to contrast it with the two-electron water oxidation reaction (2 $e^-$ WOR) that produces $H_2O_2$, shown in Equation (1.3). The anodic reactions are in competition with each other, and thus improving the selectivity towards $H_2O_2$ rather than $O_2$ has been the primary research concern.

$$4\,H_2O + 4\,e^- \rightarrow 2\,H_2 + 4\,OH^- \tag{1.1}$$

$$4\,OH^- \rightarrow 2\,H_2O + O_2 + 4\,e^- \tag{1.2}$$

$$2\,OH^- \rightarrow H_2O_2 + 2\,e^- \tag{1.3}$$

Much of the literature focuses on finding and testing new anode materials for anodic $H_2O_2$ production. One class of materials are metal oxide nanoparticles deposited onto a conductive substrate, which have been examined both experimentally and computationally. [17–19] Viswanathan et al. looked into the multi-step electron-transfer pathways that lead preferentially to the 2 $e^-$ WOR rather than the 4 $e^-$ WOR. [15] They performed computational chemistry calculations to show that an optimum in chemical activity towards the 2 $e^-$ WOR exists based on the anode material used.

Siahrostami et al. extended the study to identify the preferred end product of the anodic reaction based on the binding energies of reaction intermediate species. [20] They showed that there was another anodic reaction which could occur on these materials, the one-electron water oxidation reaction (1 $e^-$ WOR), shown in Equation (1.4). In this reaction, the product is a highly reactive radical species, $OH^\bullet$.

$$OH^- \rightarrow OH^\bullet + e^- \tag{1.4}$$

Another class of materials that are reported to produce anodic $H_2O_2$ are carbon-based electrodes. While simple carbon fiber papers can work, the most exotic material was a carbon fiber paper treated with polytetrafluoroethylene (PTFE) reported by Xia et al. The authors ascribe the significant $H_2O_2$ production to the confinement of gas bubbles on the anode surface that change the local micro-environment, while other groups used computational chemistry to ascribe the enhanced $H_2O_2$ production to the electron-withdrawing character of the nearby carbon-fluorine bond. [21, 22] The potential dissolution of PTFE into the electrolyte stream represents an undesirable hazard that would be difficult to mitigate. Additionally, both untreated and PTFE-treated carbon fiber papers undergo significant oxidation themselves, as carbon is easily oxidized, leading to eventual degradation of the fibers and the anode itself. Thus, these carbon-based anodes are not a favorable choice for industrial operation. A notable exception, used throughout this dissertation, is boron-doped diamond (BDD). This carbon-based electrode material still produces significant amounts of $H_2O_2$ but features extremely stable carbon-carbon bonds that prevent electrode degradation. [23, 24]

With many catalysts known for the 2 $e^-$ WOR, effort was made to understand the reaction mechanism in greater detail. But achieving this for the wide variety of anode materials requires knowledge of the exact species present at the anode surface and of short-lived intermediate species in the bulk, both of which are difficult to verify experimentally. Broadly speaking, there are two groups of proposed reaction pathways for anodic $H_2O_2$: a direct pathway, and an electrolyte-mediated pathway. A brief schematic of these mechanisms is shown in Figure 1.2.

The proposed direct pathways involve standard catalytic mechanisms such as the Eley-Rideal mechanism or less commonly seen pathways such as the dimerization of radical species. [25–30] However, the production of $H_2O_2$ appears to be dramatically improved by the use of carbonate or bicarbonate based electrolytes, and has led to proposed reaction mechanisms that involve the electrolyte itself. Gill et al. proposed a possible mechanism for the 2 $e^-$ WOR that proceeds by bicarbonate electrolyte acting as an intermediate in a catalytic cycle. [31] This proposed mechanism matches the overall electrochemistry that the reaction involves two electrons, but also matches experimental observation of the influence of the electrolyte. Kuttassery et al. proposed a mechanism where bi(carbonate) acts as a cofactor to the anode. [32] While there is still debate about the precise mechanism, further evidence supporting the hypothesis of the electrolyte's involvement has been shown. [33]

The quantification of the anodic $H_2O_2$ itself also leads to difficulties in unraveling the reaction mechanism, because the liquid $H_2O_2$ produced is immediately diluted

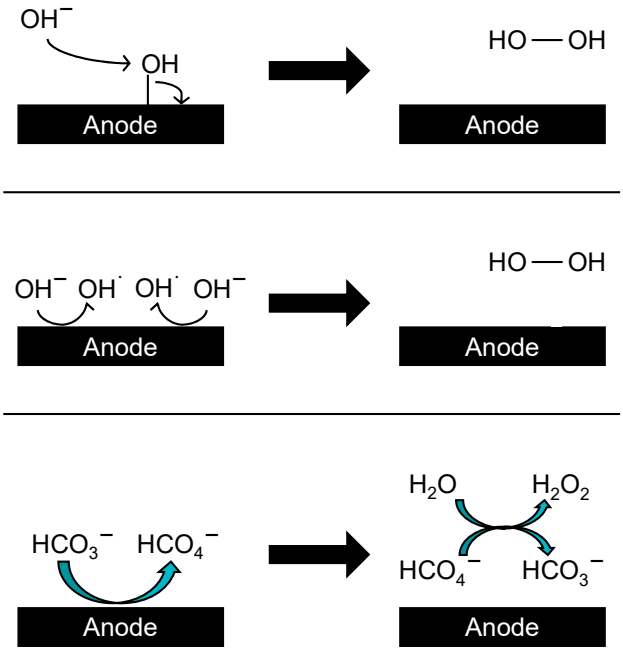


Figure 1.2: A simplified schematic of the proposed mechanisms for anodic $H_2O_2$ production. The top schematic is the Eley-Rideal mechanism, where an $OH^-$ anion binds to an adsorbed OH species to produce $H_2O_2$. [25–27] The middle schematic shows the dimerization of two radicals from 1 $e^-$ WOR to produce $H_2O_2$. [28–30] The bottom schematic is the mechanism proposed by Gill et al., where the bicarbonate ($HCO_3^-$) electrolyte is oxidized at the anode surface and then reacts with bulk water ($H_2O$) to form $H_2O_2$. [31] The block arrows in the bottom schematic represent more complicated mechanisms with intermediate steps rather than direct electron transfers.

by the surrounding electrolyte, thus lowering the threshold before which we can reliably measure any $H_2O_2$. We must therefore rely on a more generalized description of the extent of $H_2O_2$ production that can be used in calculations for scaling up this reaction.

### 1.2.2. Electrochemical Engineering of Anodic $H_2O_2$

The selectivity of an electrochemical reaction with multiple reaction pathways is called the faradaic efficiency, and is a measure of how much electrical charge has gone to the formation of the desired product. The fraction of electrons used for the desired product over the total number of electrons passed is the faradaic efficiency, often expressed as a percentage. In a typical case, this is easily calculated by measuring the product concentrations and comparing them to the delivered current.

But $H_2O_2$ is an unstable product, and undergoes two main decomposition reactions, shown in Equations (1.5) and (1.6). The former is the further oxidation of $H_2O_2$ to $O_2$ and occurs at the anode surface, while the latter is a disproportionation reaction that occurs in the bulk electrolyte.

$$H_2O_2 + 2\,OH^- \rightarrow 2\,H_2O + O_2 + 2\,e^- \tag{1.5}$$

$$2\,H_2O_2 \rightarrow 2\,H_2O + O_2 \tag{1.6}$$

As soon as $H_2O_2$ is produced at the anode, it can immediately be further oxidized on exposure to the anode. Additionally, any $H_2O_2$ that leaves the anode surface and diffuses to the bulk solution will also inevitably degrade over time. As the electrode area is enlarged during scale-up and as the amount of electrolyte increases, these effects will increase. The faradaic efficiency calculated by measuring product concentration will therefore only be an effective faradaic efficiency of the process.

Most industrial chemical processes operate continuously to maximize production rates, and industrial electrolyzers are typically operated as stacks of electrolyzers in a flow cell configuration. In this configuration, the electrolyte is recirculated and the produced gases are separated in-line. A typical flow cell configuration for the production of anodic $H_2O_2$ is shown in Figure 1.3, but the co-production of liquid product brings new challenges. First, the re-introduction of $H_2O_2$ from the reservoir back to the anode chamber increases the likelihood of the surface reaction in Equation (1.5) occurring again. Second, the longer the recirculation time before $H_2O_2$ separation, the greater the time for the bulk decomposition reaction of Equation (1.6) to occur.

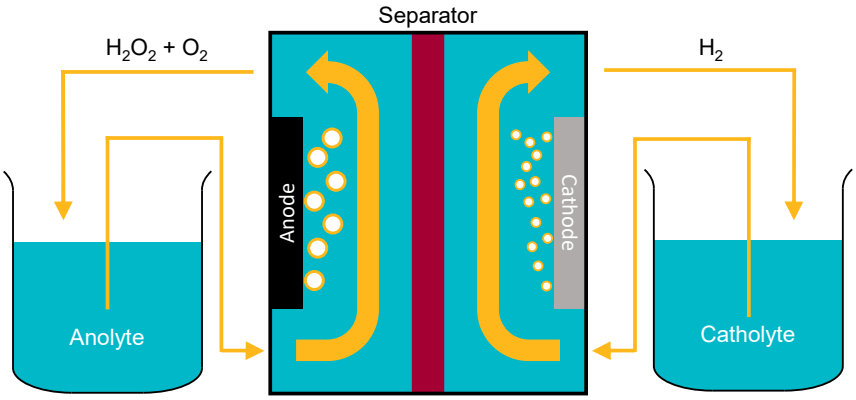


Figure 1.3: A simplified schematic of an electrochemical flow cell for anodic $H_2O_2$ production with yellow arrows indicating the path of electrolyte flow. The electrolyte on the anode side of the separator is referred to as the anolyte, and this convention carries over to the catholyte.

This competition between $H_2O_2$ generation and $H_2O_2$ degradation has implications on the operation of electrolyzers for this reaction. One solution could be to operate the electrolyzer in a single-pass configuration, where electrolyte is passed once over the electrode and then sent through a separation train to extract $H_2O_2$ before being recycled. The effect of flow rate on the outflow stream in single-pass configuration is shown in Figure 1.4. As the flow rate increases, the outlet stream concentration sharply decreases but the effective faradaic efficiency increases. The total $H_2O_2$ production rate can also be found from these plots by multiplying the flow rate by the concentration. Examining Figure 1.4a, we can see that increasing the flow rate from 5 mL $min^{-1}$ to 100 mL $min^{-1}$ leads to an increase in the production rate from 0.33 mmol $min^{-1}$ to 0.8 mmol $min^{-1}$.

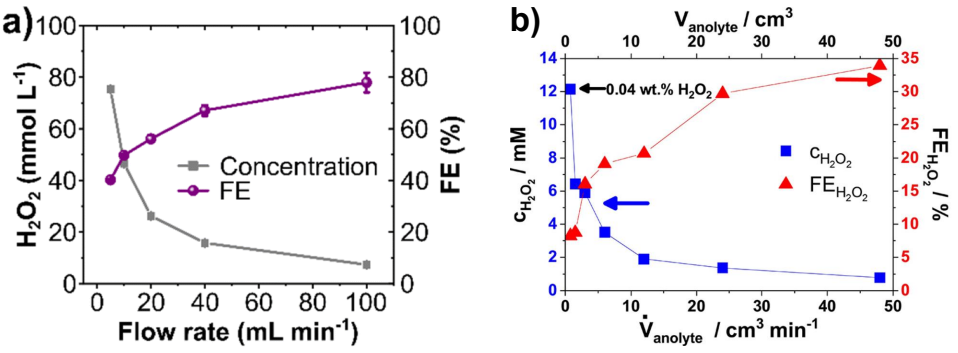


Figure 1.4: Plots from literature showing the effect of single-pass electrolyte flow rate on anodic $H_2O_2$ production using a BDD anode and 2 M $K_2CO_3$ electrolyte from a) Pangotra et al. (Reproduced under CC BY 3.0) [34] and b) Vass et al. (Reproduced under CC BY 4.0) [35]

These plots would indicate that single-pass configuration at high flow rate is the best choice. But when scaling up these reactions for maximum chemical production rates, we must also consider the downstream separation of the products. As a general heuristic, most chemical separations are more effective at higher concentrations. A worthy compromise would be to recirculate the electrolyte at a high flow rate until the anolyte has reached a sufficient $H_2O_2$ concentration, and then send it for separation. The extra $H_2O_2$ gained by continuing the reaction while recirculating should ideally outweigh the increased decomposition chance due to reintroducing the $H_2O_2$ to the anode and the longer residence times. However, recirculating electrolyte in this case can lead to other complications due to poor $OH^-$ transport in bi(carbonate) solution, which are briefly outlined in the next section.

## 1.3. AIMS AND OUTLINE

This dissertation explores the electrochemical engineering of the anodic production of $H_2O_2$ in alkaline water electrolysis. Specifically, we seek to fill the gap in literature concerning how this reaction would perform in the relevant industrial configuration, namely with recirculating electrolyte and keeping the final sale of product in mind. What are the limitations of electrolyzers when operated for $H_2O_2$ co-production and the causes of these limitations? How much $H_2O_2$ can we reliably generate and can we model this? Finally, using this knowledge, what does the separation of the produced $H_2O_2$ look like and can it be a profitable route given the current technology?

We begin with Chapter 2 which examines an often overlooked issue in recirculating electrolyte systems. As time goes on, the anolyte and catholyte slowly change composition due to insufficient $OH^-$ transport across the separator. This gradual depletion of $OH^-$ anions in the electrolyte leads to performance issues for the device such as rising voltages and falling currents. While this issue is often resolved in lab-scale by flowing electrolyte in single-pass operation, the recirculating system must be more carefully examined for scale-up.

The findings from this chapter are then carried over into an experimental setup used to produce anodic $H_2O_2$ in Chapter 3. The lab-scale setup operated in this chapter is run in the industrially relevant case, with higher current densities and recirculating flow. We use a stable BDD anode to generate concentration curves of $H_2O_2$ versus time and then use a reaction engineering description based on mole balances to develop a mathematical description of the system. The equations formulated can then be used to predict the resulting $H_2O_2$ concentrations over time given certain geometric and electrochemical parameters.

With an understanding of the pitfalls of recirculating electrolyte systems and an understanding of how $H_2O_2$ concentration develops over time, we then explore how to produce anodic $H_2O_2$ at process scale and sell it as a viable product in Chapter 4. This chapter begins by investigating the feasibility of separating $H_2O_2$ from the electrolyte for sale and finds that $H_2O_2$ can be better valorized as sodium percarbonate, a common detergent. A process design to achieve this is performed and the techno-economics of the process are evaluated. The input parameters are then adjusted to examine which parameters are most sensitive to the overall economic viability of co-producing $H_2O_2$ at the anode as an offset for green $H_2$ production costs. Finally, Chapter 5 concludes this dissertation and provides recommendations for future work on this topic.

# 2

# PRACTICAL LIMITATIONS IN GENERATING HYDROGEN PEROXIDE


## ABSTRACT

The commercialization of (bi)carbonate-based electrolyzers for reactions such as $CO_2$ reduction requires examination of their long-term operation. We studied the effects of electrolyte depletion and electrolyzer performance drop-off through experiments and simulations in a system with separated, recirculating electrolyte reservoirs. The effects of mass transport, electrochemical reactions, and equilibrium reactions form a combined picture that explains the behavior in these systems, which is characterized by insufficient $OH^-$ transport for electrochemical reactions at the anode surface. The carbonate equilibrium shifts towards bicarbonate as $OH^-$ anions are consumed at the anode, and the bicarbonate equilibrium shifts further to $CO_2$ as physical gas stripping by $O_2$ bubbles remove dissolved $CO_2$ until the electrolyte is fully depleted. We reduce the system into a simplified 1-D numerical model that identifies the relevant phenomena of the system. We use this model in tandem with experiments to show the loss of dissolved carbon due to physical gas stripping and electro-osmotic flow from anode to cathode in the system. The simulations agree with experimental measurements and show that migration is the dominant component of the ionic transport that sustains the current. Our results show that continuous operation of these systems is not possible without some strategy to improve $OH^-$ transport to the anode, such as recombining electrolyte streams after separation, using novel separators, or operating at much lower current densities.



The work in this chapter has been submitted for publication as S. A. Phadke, J. W. Haverkort and W. de Jong. 'Recirculating carbonate and bicarbonate based electrolyzers cannot operate continuously without in-line separation due to electrolyte depletion and ion crossover.'

## 2.1. INTRODUCTION

With more stringent emissions regulations comes the need for more sustainable methods of chemicals production. One of these methods is the electrochemical formation of commodity chemicals through electrolysis using renewable electricity and/or renewable feedstocks. [36] One example would be carbon dioxide ($CO_2$) reduction to produce methane, ethylene, oxalate, etc. [37] Another example is the electrochemical production of hydrogen peroxide ($H_2O_2$) in alkaline systems, which could displace the currently unsustainable production route through anthraquinone oxidation. [15, 38] Both of these electrochemical processes use aqueous electrolytes based on either carbonate ($CO_3^{2-}$) or bicarbonate ($HCO_3^-$) as the anion. But these aqueous, (bi)carbonate-based electrolyzers have some drawbacks. One issue is larger ohmic losses due to the lower conductivity of the electrolyte when compared to the typical 30 wt% potassium hydroxide (KOH) solution used in alkaline water electrolysis. [39, 40] Another drawback is that the lower concentration of charge-carrying hydroxide ($OH^-$) anions compared to 30 wt% KOH means that transport of $OH^-$ from cathode to anode is insufficient to achieve steady-state at high currents. [41] The electrochemical reactions at the anode in (bi)carbonate-based electrolyzers must therefore consume a different source of $OH^-$ anions instead: the electrolyte itself.

The (bi)carbonate anions are part of an equilibrium reaction network involving $CO_3^{2-}$, $HCO_3^-$, and $CO_2$, as well as protons ($H^+$) and $OH^-$ through water equilibration. Under an applied potential, $OH^-$ anions are consumed at the anode by electrochemical reaction and the local pH drops. Le Chatelier's principle dictates that these equilibrium reactions then shift to provide more free $OH^-$, which is further consumed by the anodic reactions. This can equivalently be viewed as arising from the generation of $H^+$ ions from the anodic reactions. In the catholyte, the $OH^-$ produced at the cathode cannot be transported through the porous separator to the anode quickly enough, and the catholyte pH rises. During this time, both $CO_3^{2-}$ and $HCO_3^-$ are also transported to the anolyte by migration and diffusion, where they undergo the same equilibrium shifts. [42, 43]

This pH swing can be mitigated in standard alkaline water electrolysis, where the anolyte and catholyte can be recombined after gas separation using a balancing line. The balancing line connects the two electrolyte tanks and ensures continual operation. [44] But in an electrochemical system that produces liquid products like $H_2O_2$ instead of exclusively gaseous products, the reservoirs cannot be mixed, as doing so would introduce the liquid product to the opposite electrode reaction and decompose it. Re-mixing the electrolyte would require in-line separation, which is very difficult for the low single-pass product concentrations that are typically achieved with these devices. When the electrolyte is recirculated in these systems without re-mixing, the $OH^-$ capacity in the anolyte steadily depletes, and the pH difference between the two chambers increases. [45–47] As this continues, the current drops to a limiting value as the electrode reactions slow down. Due to this equilibrium-based $OH^-$ capacity of the electrolyte, the reaction can run for longer than compared to dilute KOH solution of the same pH, but the depletion will still inevitably occur. This unsteady operation is detrimental to commercial chemicals production

by electrolysis, as lower current leads to lower chemical production rates. Therefore, the phenomenon of electrolyte depletion must be better understood if we hope to industrialize these processes.

Previous investigations into the topic have either focused mainly on the crossover of $CO_2$ reduction products from catholyte to anolyte, the impact of reaction conditions on product selectivity, or the migration of dissolved carbon species when $CO_2$ is being fed from the cathode side. [47–51] Here, we present experiments showing electrolyte depletion in a zero-gap alkaline water electrolyzer using carbonate-based electrolyte and recirculating flow with separated reservoirs. Our experiments do not include a pressurized feed of $CO_2$ into the catholyte through a gas-diffusion electrode, meaning that we are examining a system without an additional influx of species that lowers the overall pH. We also perform simulations using COMSOL Multiphysics to explore the system dynamics and identify key processes that explain the observed behavior. The results show that $CO_3^{2-}$ is depleted in the anolyte by the electrochemical demand of the anodic reactions, but that $HCO_3^-$ is then depleted due to physical gas stripping of $CO_2$ from solution by the generated $O_2$ bubbles. This results in a significant amount of dissolved carbon loss, as dissolved carbon species also migrate across the separator to the anode, where they are then equilibrated away to gaseous $CO_2$. We found that the migration of anionic species was the most significant contributor to the observed current until just before the electrolyte is fully depleted. The results also provided secondary evidence for the reaction mechanism of anodic $H_2O_2$ formation based on the peroxydicarbonate ($C_2O_6^{2-}$) catalytic pathway.

## 2.2. METHODS

### 2.2.1. EXPERIMENTAL SETUP

We constructed a zero-gap electrolyzer using laser-cut sheets of 5 mm thick poly(methyl methacrylate) (PMMA) and gaskets of silicone and ethylene propylene diene monomer (EPDM) rubber. An image of the electrolyzer can be seen in Figure 2.1. The cell was compressed together using nuts and bolts and made leak-tight with the aid of a thin, 3-D printed insert that added extra compressive force around the electrode chambers and prevented undesired crossover around the separator. Hose pillars were 3-D printed using Formlabs V4 resin and glued with epoxy into the PMMA endplates. The electrolyte used was 1 M $Na_2CO_3$ (Merck, ACS Reagent, anhydrous, ≥99.5%, granules) made using milli-Q water (Merck Millipore, 18.2 MΩ·cm). The separator used was Zirfon Perl UTP 500 from Agfa (500 µm thickness, 50% porosity). The separator was kept submerged in the 1 M $Na_2CO_3$ electrolyte between experiments in order to keep it hydrated and retain its transport properties. The anode used was Boron-Doped Diamond (BDD), 50 $cm^2$ from Condias, 2500 ppm p-type doping, chemical vapor deposition coated onto both sides of an expanded metal niobium substrate. BDD was chosen due to the need for a stable material under extremely oxidizing conditions. Many anodes were tested, such as nickel, stainless steel, and some proprietary coated electrodes, but all except BDD underwent significant corrosion during the experiments. The

cathode was a piece of nickel expanded metal from ExpandoMetal, 0.4 mm thick and 60 $cm^2$.

The current collectors were water-jet cut from 1 mm thick titanium plates with vertical busbars spanning the electrode faces. These vertical struts distributed current more evenly across the electrode surface while allowing gas bubbles to escape. These current collectors were glued into a recess that was milled out of the PMMA plates. They also helped to compress the electrodes onto the separator surface and ensured a zero-gap configuration. To ensure that the only available surface area for ion transport was immediately between the electrodes, a piece of gasket was cut to fit each electrode, which masked off any other separator surface area.

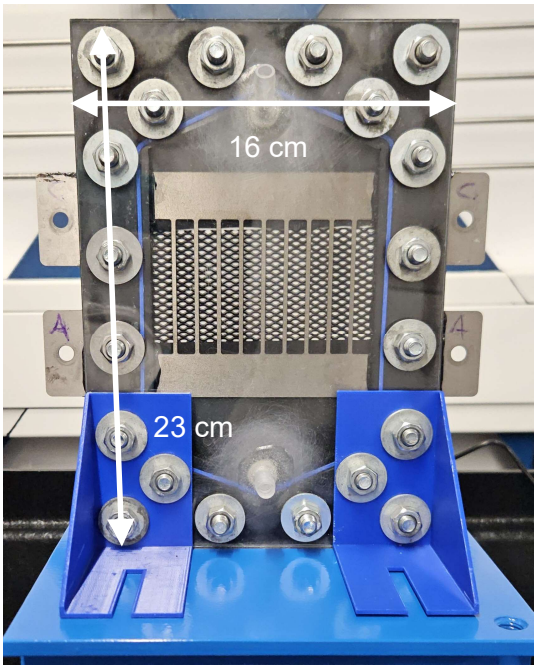


Figure 2.1: Photo of the electrolyzer with a view of the anode side. The black BDD expanded metal electrode in the center is surrounded by solid black EPDM gasket of the same thickness, which masks off all porous separator that is not directly in between the electrodes. The single electrode is held in place by the vertical struts of the titanium current collector, which also distribute current evenly across the electrode surface. The tabs extending out the left and right provide terminals for the power supply connections. The thin, blue, diamond-shaped piece around the electrode chamber is the 3-D printed insert that ensures a compressive force around the electrode chambers and prevents any leakage. The entire cell is compressed using nuts and bolts, with 3-D printed feet to keep the electrolyzer upright.

A Delta Elektronika SM15-200D was used to supply power, connected using ring terminals to the current collectors. Two electrolyte reservoirs were constructed from laser-cut PMMA and glued together using Acrifix 0192. During the experiments, these reservoirs were stirred using magnetic stir bars. Experiments were intentionally performed with low volumes of electrolyte (350 mL each for anolyte and catholyte) and large potential differences in order to quickly deplete the electrolyte. With these operating conditions, it was necessary to cool the electrolyte to prevent undesired changes to transport properties or reaction rates due to temperature increase. Simple heat exchangers were constructed using stainless steel Swagelok tubing and placed in a large plastic container that could be filled with ice and water as needed to manually regulate the electrolyte temperature. The electrolyte temperature was maintained between 20°C and 35°C.

A Longer BT100-3J peristaltic pump with DG15-24 two-channel pump head was used to pump electrolyte through the cell, while keeping the two streams separated. The flow path was from reservoir, through heat exchanger, through one chamber of the electrolyzer, and back to the same reservoir. The flow rate used was 250 mL $min^{-1}$, which led to an electrode chamber residence time of about 15 seconds. All tubing between components was made from silicone. An image of the full experimental setup is shown in Figure 2.2.

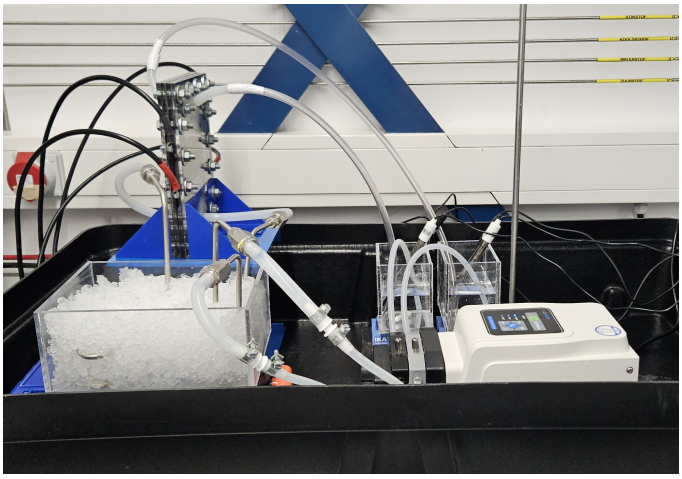

Figure 2.2: Photo of the experimental setup. In the bottom right is the peristaltic pump which pumps electrolyte into the heat exchangers in the bottom left. The heat exchangers are stainless steel tubes immersed in a container of ice. The exits of the heat exchangers lead into the electrolyzer in the top left, with black power cables attached to the current collectors. The electrolyte flows into the bottom of each electrode chamber, out the top, and returns to the reservoirs behind the peristaltic pump. Each reservoir has a temperature and pH probe submerged in it.

During the experiments, a significant electro-osmotic flow from anolyte to

catholyte was observed. This change in volume is caused by the negatively charged porous separator inducing a positive counter-charge in the electrolyte, resulting in a net fluid motion. [52] This leads to the anolyte losing water and the catholyte gaining water, contrary to the stoichiometry of the electrochemical reactions. The experiments were set to run for 200 minutes, but were stopped in the case that the anolyte reservoir ran dry and the pump could no longer recirculate electrolyte through the device. With a total of 350 mL of electrolyte in one reservoir and a volume of 250 mL in the tubing, heat exchanger, and electrode chamber on one side of the device, the current was switched on with 100 mL remaining in the reservoir. If that 100 mL was lost from the anolyte chamber before 200 minutes, the experiment was stopped.

### 2.2.2. Experimental Measurement

The power supply was controlled using analog voltage signals provided by a National Instruments Data Acquisition Device. The voltage was fixed at the current collectors to either 7.5 V, 6.5 V, or 5.5 V and the current was measured every 0.5 seconds. The pH and temperature of the reservoirs were monitored using PCE Instruments pH and temperature probes (PCE-228), recording data every 10 seconds. Experiments started with measured volumes of electrolyte in each reservoir and stopped when the anolyte reservoir ran dry due to electro-osmotic flow bringing electrolyte from anode side to cathode side. This corresponded to a loss of roughly 100 mL, leaving 250 mL remaining to fill the rest of the anolyte side of the system.

The BDD anode used in this experiment has been shown in literature to form peroxydicarbonate ($C_2O_6^{2-}$) through the oxidation of $CO_3^{2-}$ anions. [53–55] The resulting $C_2O_6^{2-}$ is proposed to react with water in the bulk to form $H_2O_2$. [34] To measure this produced $H_2O_2$, we used the potassium permanganate ($KMnO_4$) titration procedure outlined by Gill and Zheng. [56] Briefly, a sample of electrolyte is acidified with a 1:5 diluted sulfuric acid ($H_2SO_4$, Merck, ACS Reagent, 95%-98%) solution, and then titrated drop-wise using a burette with purple 2 mM $KMnO_4$ solution (Merck, Titripur, standardized against oxalate, 0.02 M, diluted tenfold using milli-Q water) until a light pink color remained in the initially colorless $H_2O_2$ sample. The volume of $KMnO_4$ added to reach the titration endpoint is then used to calculate the $H_2O_2$ concentration of the sample based on the stoichiometry.

To measure liberated $CO_2$ gas from the anolyte, we used a gravimetric assay. The outlet of the anolyte was connected to a simple gas-liquid separator, and when the separated liquid stream flowed into the reservoir, the gas stream was fed into a beaker containing a mixture of 1 M barium chloride ($BaCl_2$ dihydrate, Merck, ACS reagent, ≥99%) solution mixed with 1 M sodium hydroxide (NaOH, Merck, ACS reagent, ≥97%, pellets) solution. This high pH solution readily captured any gaseous $CO_2$ while letting oxygen bubble through freely. The trapped $CO_2$, in the form of $CO_3^{2-}$ in solution, then quickly reacted with barium ions in solution to precipitate as the highly insoluble barium carbonate ($BaCO_3$). This precipitate was allowed to settle, vacuum filtered, and then dried in an oven to measure its mass.

### 2.2.3. NUMERICAL MODEL DEVELOPMENT

The model created was a simplified 1-D model using COMSOL Multiphysics v6.2, where the 1-D domain represented the porous separator. The domain was modeled using the "Tertiary Current Distribution, Nernst-Planck" interface, with boundary Ordinary Differential Equations (ODE's) used to describe the content of the reservoirs. A schematic showing the experimental setup and its translation to the numerical geometry is depicted in Figure 2.3. Whereas other models for such a system are 2-D and include a $CO_2$ feed through a gas-diffusion electrode, our model can be simplified due to the simpler nature of the transport phenomena near the electrode surfaces. [57, 58] Our model includes the contributions of diffusion, migration, and convection, and also enforces electroneutrality everywhere. The effects of temperature change were not included, and the simulation temperature was set to a constant 298.15 K. The full details of the simulation can be found in Section 2.B.

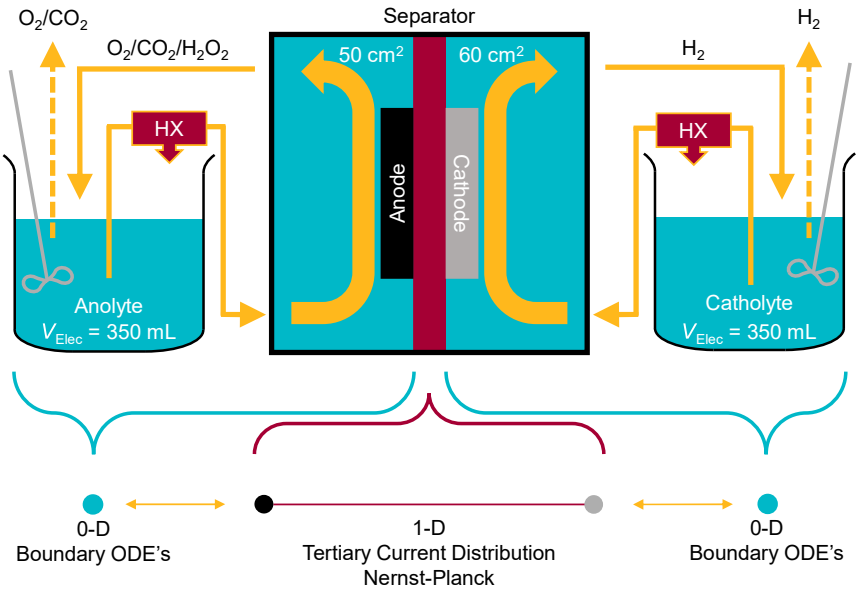


Figure 2.3: Schematic of the experimental setup compared to the numerical geometry. The porous separator is treated as a 1-D line segment with the anode and cathode included within the domain. All the electrolyte on one side of the separator (in the reservoir, tubing, heat exchanger, and electrolyzer chamber) is combined into a single set of Boundary ODE's for that side. The HX represents a heat exchanger removing heat from the electrolyte flow before entering the electrode chamber. The solid yellow arrows in the experimental schematic represent electrolyte flow and are represented in the numerical schematic by solid yellow arrows between the 0-D and 1-D domains that are mathematically described using the vertical liquid velocity in the electrode chamber.

The equations satisfied by the model are written in Equations (2.1) – (2.4).

$$N_{\mathrm{D},i} = -D_{\mathrm{Eff},\,i}\nabla c_i \tag{2.1}$$

$$N_{\mathrm{M},i} = -z_i\mu_i\mathcal{F}c_i\nabla\phi \tag{2.2}$$

$$N_{\mathrm{C},i} = uc_i \tag{2.3}$$

$$\sum z_i c_i = 0 \tag{2.4}$$

In the preceding equations, $N_{\mathrm{D},i}$, $N_{\mathrm{M},i}$, and $N_{\mathrm{C},i}$ are the diffusive, migratory, and convective fluxes of species $i$, respectively, $D_{\mathrm{Eff},i}$ is the effective diffusivity, $\nabla c_i$ is the concentration gradient, $z_i$ is the ionic charge, $\mu_i$ is the mobility calculated by the Nernst-Einstein relation shown in Equation (2.B.16), $\mathcal{F}$ is Faraday's constant, and $\nabla\phi$ is the electrolyte potential gradient. The electro-osmotic velocity, $u$, is calculated based on the electrolyte potential difference and shown in Equations (2.B.17) and (2.B.18).

The molecular and ionic species included in the simulation were $H^+$, $OH^-$, $CO_3^{2-}$, $HCO_3^-$, $CO_2$, $C_2O_6^{2-}$, $H_2O_2$, $HO_2^-$, and $Na^+$. For the anolyte reservoir boundary ODE's, an additional species representing gas phase $CO_2$, $CO_2$(g), was also included. Equation (2.4) was satisfied in the 1-D separator by balancing the other ionic species with $Na^+$ as the counterion.

The left boundary of the 1-D domain represented the BDD anode and here the oxygen evolution reaction (OER), peroxydicarbonate ($C_2O_6^{2-}$) generation reaction, and anodic oxidation of $H_2O_2$ take place. At the right boundary of the 1-D domain representing nickel, the hydrogen evolution reaction takes place. These four electrochemical reactions are detailed in Equations (2.5) – (2.8).

$$4\,OH^- \rightarrow O_2 + 2\,H_2O + 4\,e^- \tag{2.5}$$

$$2\,CO_3^{2-} \rightarrow C_2O_6^{2-} + 2\,e^- \tag{2.6}$$

$$H_2O_2 + 2\,OH^- \rightarrow O_2 + 2\,H_2O + 2\,e^- \tag{2.7}$$

$$2\,H_2O + 2\,e^- \rightarrow 2\,OH^- + H_2 \tag{2.8}$$

The electrochemical kinetics were modeled using the Butler-Volmer equation shown in Equation (2.B.14), with the equilibrium potential calculated using the Nernst equation shown in Equation (2.B.13). To account for concentration overpotential effects, the exchange current density term in the Butler-Volmer equation for the anodic reactions was multiplied by a concentration normalization factor, shown in Table 2.B.4.

Each electrode was also modified with a film resistance term in order to account for the ohmic loss over the external circuit and current collectors. A simple measurement of the current collectors was performed by directly connecting the power supply leads to the center and one outer flap of a single current collector and measuring the ohmic drop. The resulting measurement of 15 mΩ was then fixed as the film resistance on each electrode in the simulation as an approximation of ohmic losses.

The equilibrium reactions mentioned earlier concerning the electrolyte are shown in Equations (2.9) – (2.11). The unidirectional reactions for the formation and bulk disproportionation of $H_2O_2$ are shown in Equations (2.12) and (2.13). Lastly, the equilibrium reaction for the deprotonation of $H_2O_2$ based on pH is shown in Equation (2.14). These reactions occur everywhere in the simulation and details of their implementation can be found in Table 2.B.2.

$$CO_2 + OH^- \rightleftharpoons HCO_3^- \tag{2.9}$$

$$HCO_3^- + OH^- \rightleftharpoons CO_3^{2-} + H_2O \tag{2.10}$$

$$H_2O \rightleftharpoons OH^- + H^+ \tag{2.11}$$

$$C_2O_6^{2-} + 2\,H_2O \rightarrow 2\,HCO_3^- + H_2O_2 \tag{2.12}$$

$$2\,H_2O_2 \rightarrow O_2 + 2\,H_2O \tag{2.13}$$

$$H_2O_2 + OH^- \rightleftharpoons HO_2^- + H_2O \tag{2.14}$$

At each end of the 1-D domain, overlapping with the electrodes, a flux boundary condition was imposed in order to exchange contents with the reservoirs, shown in Equation (2.15).

$$N_{B,i} = k_{l,\,\mathrm{mt}}\left(\frac{n_{\mathrm{Res},i}}{V_{\mathrm{Elec}}(t)} - c_i\big|_B\right) - u\frac{n_{\mathrm{Res},i}}{V_{\mathrm{Elec}}(t)} \tag{2.15}$$

In the expression for the boundary flux of species $i$, $N_{B,i}$, the first term on the right-hand represents the recirculating flow of electrolyte to the electrode chamber, where $k_{l,\,\mathrm{mt}}$ is the mass transfer coefficient of 8.3 mm $s^{-1}$, $n_{\mathrm{Res},i}$ is the amount of species $i$ in the reservoir (in moles), $V_{\mathrm{Elec}}(t)$ is the anolyte or catholyte volume as a function of time, and $c_i\big|_B$ is the concentration of species $i$ at the boundary of the 1-D domain representing the separator. The precise value of $k_{l,\,\mathrm{mt}}$ was set equal to the average superficial vertical liquid velocity in the electrode chamber, but is not significant so long as it is large enough. The second term on the right-hand side represents the amount of species transported by electro-osmotic flow from anolyte into the 1-D domain, where $u$ is the electro-osmotic velocity. For the boundary at the

cathode, the second term on the right-hand side is replaced by $+uc_i\big|_B$, to account for the contents of the 1-D domain being convected to the catholyte reservoir.

The electrolyte outside of the separator was modeled as a well-stirred vessel of homogeneous concentration using a set of boundary ODE's with the following general form:

$$\frac{dn_{\text{Res},i}}{dt} = -N_{\text{B},i}A_{\text{Elec}} + \left(\sum_i r_i\right)V_{\text{Elec}}(t) \tag{2.16}$$

Equation (2.16) models the change in reservoir species by including the contributions of the flux boundary conditions and the homogeneous reactions mentioned earlier. The first term on the right-hand side is equal and opposite to Equation (2.15) multiplied by the geometric electrode surface area, $A_{\text{Elec}}$. The second term on the right-hand side represents the homogeneous reactions that occur at all points in the electrolyte, including the reservoirs and tubing, where $\sum r_i$ is the sum of reaction rate terms involving species $i$. The equation for $dn_{\text{Res},CO_2}/dt$ in the anolyte includes a term that accounts for physical gas stripping of dissolved $CO_2$ based on the gas fractions that result from the calculated currents. Conversely, the equation for $dn_{\text{Res},CO_2}/dt$ in the catholyte includes a term for the modest uptake of atmospheric $CO_2$ into a stirred, alkaline reservoir. These additional terms are detailed in Equations (2.B.28) and (2.B.29).

The equation for $V_{\text{Elec}}(t)$ is found by solving Equation (2.17).

$$\frac{dV_{\text{Elec}}(t)}{dt} = \left(A_{\text{Elec}}\sum_{H_2O}\frac{j}{nF} + V_{\text{Elec}}(t)\sum_{H_2O}\nu_i r_i\right)\mathcal{V}_{\text{m},H_2O} \pm uA_{\text{Elec}} \tag{2.17}$$

In Equation (2.17), the first term on the right-hand side represents the total volume of $H_2O$ that is either generated or consumed through electrochemical and homogeneous reactions, while the second term represents the volume gained or lost due to electro-osmotic flow. The symbol $j$ is the individual current density of the electrochemical reaction, n is the molar ratio of electrons to water, $\nu_i$ is the stoichiometric ratio of water in the homogeneous reactions, and $\mathcal{V}_{\text{m},H_2O}$ is the molar volume of water at 298.15 K.

### NUMERICAL METHODS

Due to a large range of time scales across the electrochemical kinetics, homogeneous reaction rates, and transport phenomena, the numerical system described here is an extremely stiff system of differential equations. The anode boundary in particular experiences the combined effects of diffusion, migration, convection, electrochemical reactions, homogeneous reactions, and flux conditions, all while $OH^-$ is being slowly depleted. This leads to very steep gradients in concentration and reaction rates near the boundaries. To improve stability, many of the reactions are thus numerically described in terms of producing $H^+$ rather than consuming $OH^-$.

The time-dependent simulation uses quadratic element order for species concentration, electric potential, and electrolyte potential in the 1-D domain, and also uses quadratic element order for species amounts in the 0-D domain. The implicit solver was fully coupled, and used undamped Newton's method and adaptive backwards differentiation formula with maximum order 2 and minimum order 1. The mesh across the 1-D domain consisted of three separate meshes. Two of the meshes were fine meshes of 2.5 nm element size for a total of 150 nm each at either end of the 1-D domain, to better capture the steep gradients that occurred. The center of the 1-D domain used larger elements of maximum 2.5 µm, with a distribution gradually reducing the element density from the mesh near the boundaries to the center of the domain. This led to a total of 445 mesh elements. A mesh refinement study showed that decreasing the maximum element size up to a factor of 10 led only to small changes in relative values of current (< 3%) and anolyte pH (< 1%), at the cost of increasing the computational time from minutes to many hours. The mesh refinement study and its details are included in Figures 2.A.4a – 2.A.4d.

## 2.3. Results and Discussion

### 2.3.1. Experimental-simulation agreement

The current at constant cell potentials, shown in Figure 2.4, began with a sharp increase within the first few minutes. This was likely the result of initial activation of the electrodes due to changes in surface chemistry or oxidation state, or a result of local heating of the device. The cell current then decayed approximately linearly and a significant electro-osmotic flow was observed from anolyte chamber to catholyte chamber. The comparison of the experiments with the numerical model are shown in Figure 2.4, with solid lines representing experiments and dashed lines representing simulations. There is overall agreement in shape and magnitude of the profiles with a slight underprediction by the model. One possible contributor to this difference may be local temperature effects that are not accounted for in the model, which slightly improve ionic transport through the separator. A plot of the reservoir volumes from the simulations is shown in Figure 2.A.1.

Through simulations, we can decompose the current and derive the individual contributions. Figure 2.5a shows that much of the delivered current is due to migration rather than due to diffusion. We can also decompose the current by reaction type, as in Figure 2.5b, which shows for the case of 7.5 V cell potential that while OER and the $C_2O_6^{2-}$ generation reaction are initially of similar order, the latter decreases while the anodic oxidation of $H_2O_2$ increases. The anodic oxidation of $H_2O_2$ then decreases until only OER remains. Similar plots for 6.5 V and 5.5 V cell potential can be found in Figures 2.A.2a and 2.A.2b.

Examining the experimentally measured pH of the anolyte reservoir over time reveals a quick decay to a value of approximately 8.5, which is roughly the pH of 1 M $NaHCO_3$. This result is in agreement with previously reported results. [49, 59, 60] Figure 2.6a shows the comparison between experimental and simulated results for anolyte pH over time. As cell potential increases, the drop to the lower pH value plateau occurs more quickly. At 7.5 V and 6.5 V, the anolyte pH then slightly

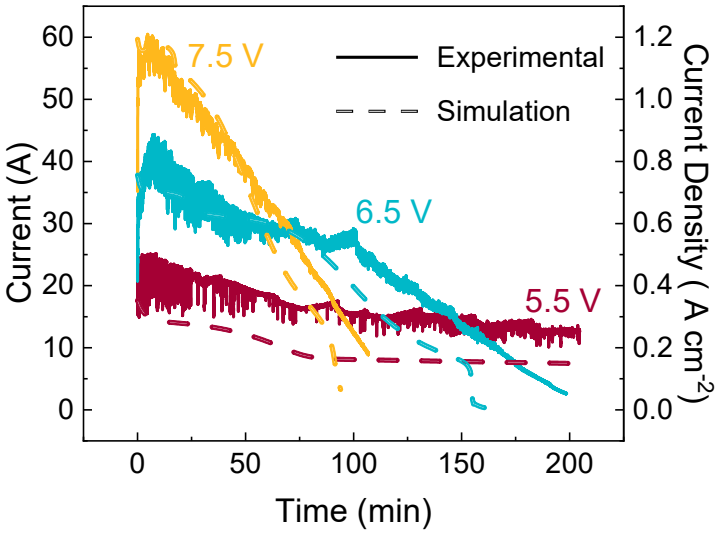


Figure 2.4: Plot of current versus time profiles at three constant cell potentials, where solid lines indicate experimental data and dashed lines indicate the simulation values. Experiments and simulations were performed at 1 bar and 25°C, beginning with 1 M $Na_2CO_3$. After an initial increase, the currents all decay roughly linearly on different time scales. The fluctuations in the experimental data are due to the fast sampling rate of 0.5 seconds, and the data shown here has not been smoothed or averaged. The current density is calculated using the geometric anode area of 50 $cm^2$.

increases before dropping again. We do not know the reason for the slight increase, but it may be due to $CO_2$ gas stripping slightly outpacing the $OH^-$ consumption from electrochemical reactions. The shape of the overall behavior is captured well by the simulations, but the timescales and magnitudes are slightly off. Figure 2.6b shows the comparison between experimental and simulated results for catholyte pH over time. Again, the qualitative agreement is correct, while the magnitudes are off. However, this change in magnitude could be due to the pH probe measurement error becoming larger as the pH approaches 14.

### 2.3.2. Simulation Results for Electrolyte Depletion

The simulation results for ion species concentration across the separator explain how the electrolyte depletes during operation. Figure 2.7 shows how the concentrations across the separator evolve over time for the case of 7.5 V. There is initially a sharp decrease in $CO_3^{2-}$ concentration with a corresponding increase in $HCO_3^-$ concentration near the anode. As $OH^-$ is consumed at the anode, the equilibrium of Equation (2.10) shifts to provide more $OH^-$ for the electrochemical reactions, pro-

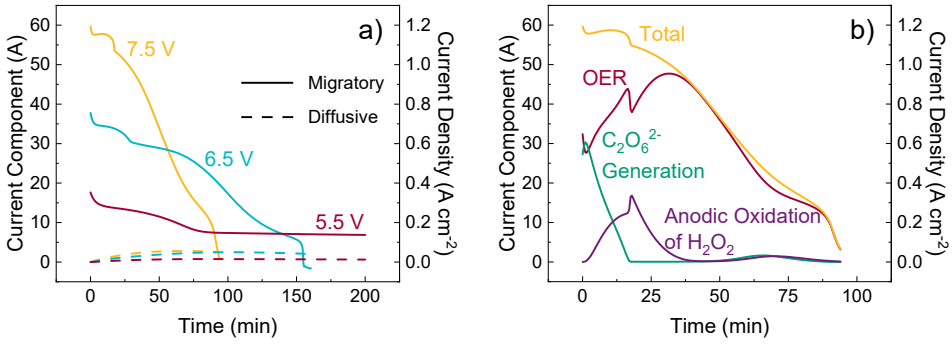


Figure 2.5: a) Plot of the contributions of migration and diffusion to the simulated cell currents at three different cell voltages, for simulations at 1 bar, 298.15 K, and beginning with 1 M $Na_2CO_3$. Migration is almost always the largest contributor of the current, until the anolyte is fully depleted, at which point diffusion becomes the dominant current contribution. b) Plot of the simulated current at 7.5 V cell potential, decomposed by electrochemical reaction at the anode for the same starting conditions as in a).

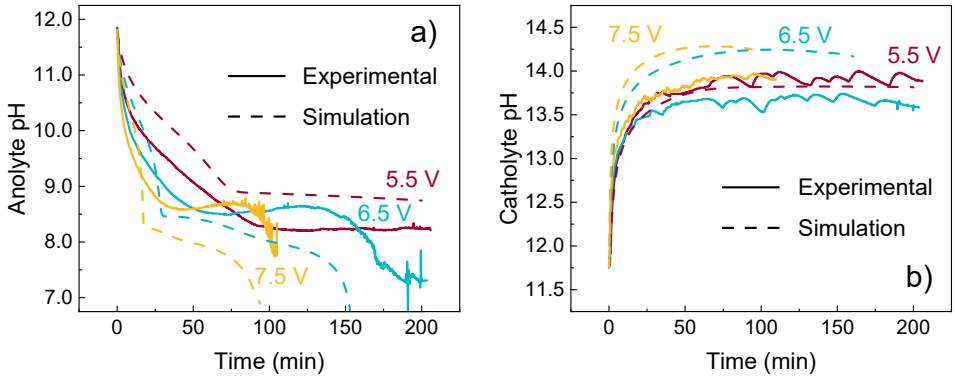


Figure 2.6: Comparison between experiments and simulations of the pH of a) anolyte reservoir and b) catholyte reservoir beginning at pH 11.75, corresponding to 1 M $Na_2CO_3$ at 1 bar and 298.15 K.

ducing $HCO_3^-$ with a corresponding drop in anolyte pH during this time. Near the cathode, there is a corresponding increase in $OH^-$ and $Na^+$ as the produced $OH^-$ cannot transport quickly enough to the anode. As time goes on, the $OH^-$ and $Na^+$ concentrations continue increasing near the cathode and the $HCO_3^-$ concentration decreases near the anode. The article submission includes short movies of the

relevant species' concentrations as a function of position across the separator over the simulation time, for each of the cell potentials simulated. These videos show the gradual depletion of ions at the anode due to electrochemical reactions exceeding the rate of ion transport across the separator. The effect of this behavior on the reservoir contents can be seen in Figure 2.8.

Figure 2.8a shows the relevant species' concentrations in the anolyte from simulations at 7.5 V. As current continues flowing through the system, the oxygen gas bubbles produced by OER strip away dissolved $CO_2$ into the gaseous phase as $CO_2$(g). This removal of aqueous $CO_2$ from the anolyte and the continued consumption of $OH^-$ at the anode shift the equilibrium of Equation (2.9) towards aqueous $CO_2$ due to Le Chatelier's principle. This then allows further physical gas stripping of $CO_2$ and further equilibrium shift, thus continuing the cycle. Eventually, all of the dissolved carbon species are fully removed from the anolyte and both the current and pH decrease sharply, as seen in Figures 2.4 and 2.6a, respectively. It should be noted that the simulations without any physical $CO_2$ stripping do not correctly replicate the current vs time profiles, as $HCO_3^-$ does not equilibrate to $CO_2$ quickly enough without the active removal of $CO_2$. The experimental confirmation of this result is discussed in Section 2.3.4, and a plot of simulation results without $CO_2$ stripping is shown in Figure 2.A.5.

While the anolyte reservoir depletes due to $OH^-$ consumption outpacing transport across the diaphragm, the catholyte reservoir instead concentrates as the produced $OH^-$ cannot transport quickly enough to the anode. Figure 2.8b shows the relevant species' concentrations in the catholyte from simulations at 7.5 V. The low concentration of $HCO_3^-$ initially present quickly drops to near zero as the large excess of $OH^-$ produced shifts the equilibrium towards $CO_3^{2-}$. After the small initial increase, the $CO_3^{2-}$ concentration then decreases due to diffusion and migration towards the anode, while the $OH^-$ concentration steadily rises. As the current drops due to ion depletion at the anode, the uptake of atmospheric $CO_2$ into the catholyte reservoir combined with a decreasing accumulation of $OH^-$ starts to slightly increase the $CO_3^{2-}$ concentration again. This follows naturally from the equilibrium relationship where a small amount of $CO_2$ introduced into an alkaline system quickly equilibrates fully to $CO_3^{2-}$. By examining the final amount of $CO_2$(g) in the anolyte compared to the starting amounts of $CO_3^{2-}$ and $HCO_3^-$, it is clear that the anolyte loses a larger amount of dissolved carbon species than was initially present, and that this came from the catholyte.

The simulations for the species' concentrations in each reservoir for 7.5 V and 6.5 V show a similar shape, but at different time scales, with the $HCO_3^-$ also fully depleting near the end of the simulation for 6.5 V. However, the simulation for 5.5 V shows an even slower time scale where the $HCO_3^-$ concentration first increases, but then does not fully decrease to zero within the simulation time of 200 minutes. The plots of the species' concentrations in the reservoirs for different cell potentials are shown in Figures 2.A.3a – 2.A.3d.

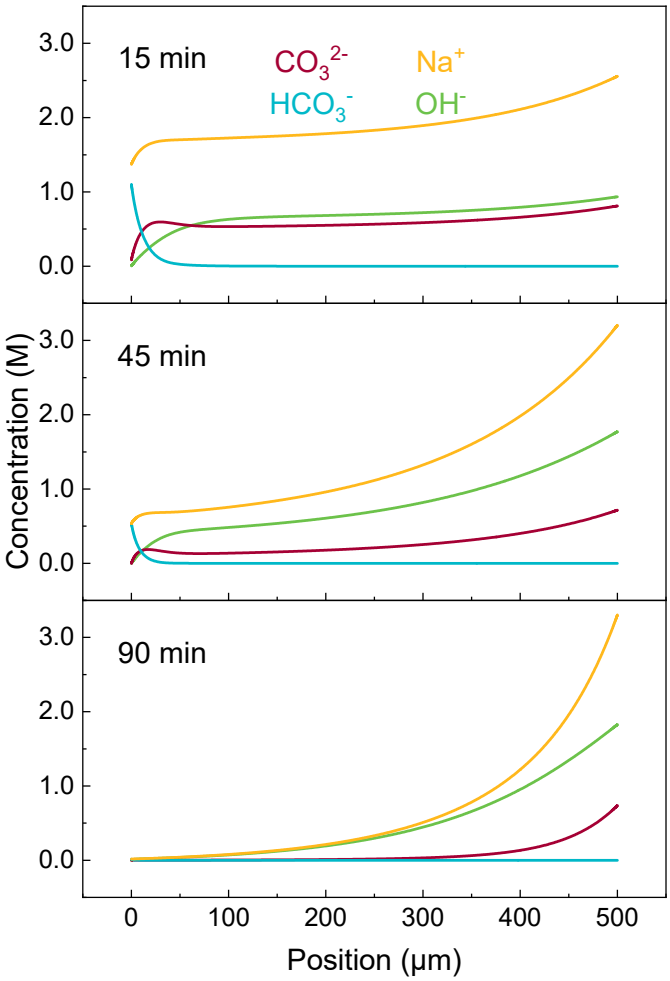


Figure 2.7: Plot of the relevant species' concentrations across the separator at different times for the case of 7.5 V cell potential. Simulations were performed at 1 bar and 25°C, beginning with 1 M $Na_2CO_3$. The left side at 0 μm represents the anode while the right side at 500 μm represents the cathode. The concentration of $HCO_3^-$ first increases at the anode and then decreases as the dissolved carbon species are slowly removed from the separator. The article submission also includes short movies of these species' concentrations across the separator over time for the cases of 5.5, 6.5, and 7.5 V cell potential.

### 2.3.3. $H_2O_2$ FORMATION

Alongside the depletion of dissolved carbon species, there are anodic reactions involved in the formation of $H_2O_2$. While there is initially $CO_3^{2-}$ present in the

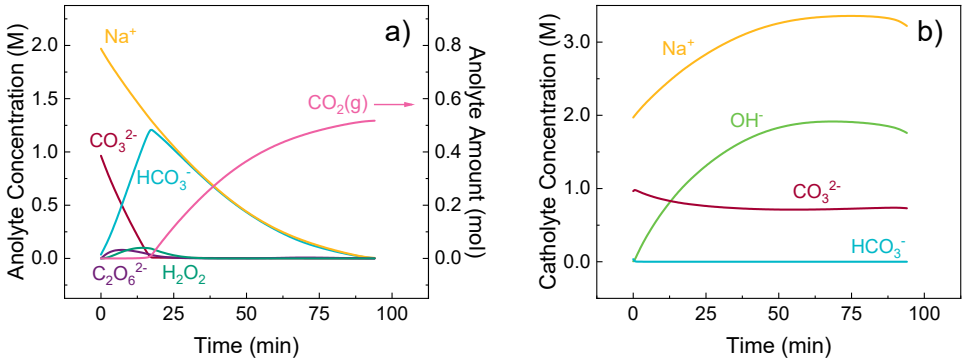


Figure 2.8: Simulations of species concentrations in the a) anolyte reservoir and b) catholyte reservoir for a cell potential of 7.5 V at 1 bar, 298.15 K, beginning with 1 M $Na_2CO_3$. The ions depleted in the anolyte are correspondingly accumulated in the catholyte, leading to a large pH gradient across the separator, as seen in Figure 2.6.

anolyte, the dimerization reaction at the anode surface to form $C_2O_6^{2-}$ shown in Equation (2.6) can occur. This $C_2O_6^{2-}$ then reacts with water to form $H_2O_2$ with a small time delay based on the rate constant of $C_2O_6^{2-}$ decay. The formed $H_2O_2$ then decays homogeneously and at the anode surface, leading to an exponential decay. The comparison of $H_2O_2$ concentration in the anolyte in the 7.5 V case can be seen in Figure 2.9. The difference between simulation and experimental values could be due to a number of factors, including that the actual kinetic rate constants change as the pH and anolyte composition change over time, which is not accounted for in the simulation. But the qualitative agreement between experimental and simulation results provides secondary evidence for the hypothesis that $H_2O_2$ is generated through a catalytic cycle involving $C_2O_6^{2-}$, rather than by direct electrochemical generation at the anode surface.

### 2.3.4. Gaseous $CO_2$ Evolution

As described in Section 2.2.2, the evolved gas from the anolyte chamber was passed through a barium solution in order to precipitate dissolved $CO_2$ as $BaCO_3$. For the case of 7.5 V, Figure 2.8a predicts that a total of 0.52 moles of $CO_2$(g) should be evolved. For complete capture and conversion of this $CO_2$(g) to $BaCO_3$, this would mean an expected dry precipitate mass of 102.6 g. The experimental mass of dry precipitate measured was 31.9 g. There could be numerous reasons for this large discrepancy, such as insufficient mixing time for the gas bubbles to interact with the barium solution, or not using a large enough molar excess of barium in solution to fully capture all of the $CO_2$. But this result provides at least a qualitative validation of the significant evolution of gaseous $CO_2$ during electrolyzer op-

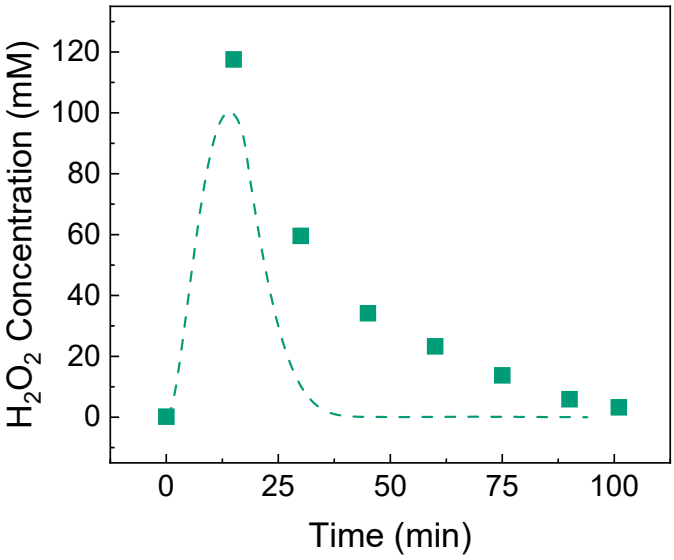


Figure 2.9: Plot of experimental vs simulated $H_2O_2$ concentrations at 7.5 V, showing fairly good agreement in both timescale and magnitude. The concentration values from the simulation are the sum of $HO_2^-$ and $H_2O_2$. Experimental measurements are expected to include both species as well, because the measurement procedure involves an acidification step. The experimentally measured $H_2O_2$ concentration decays more slowly, which could be due to changing decomposition kinetics in the anolyte as the pH decreases over time.

eration. Visually, the barium solution remained relatively clear until the 15 minute mark and then started becoming cloudy due to the formation of $BaCO_3$ precipitate. This corresponds with the simulation results for species' concentrations shown in Figure 2.8a, where $CO_2$(g) begins to evolve around the same time. The evolution of $CO_2$ over time and in significant quantity was also reported by Ma et al., but their setup had an active supply of $CO_2$. [49]

### 2.3.5. Considerations for Scale-up

From the above results, we see that (bi)carbonate-based electrolyzer systems steadily lose dissolved carbon when pushed to high currents, which could have more implications on the scaled-up system in question beyond the issue of electrolyte depletion. For example, the $CO_2$ reduction reaction typically involves feeding $CO_2$ through a gas-diffusion electrode at the cathode side, aiming to convert it to higher value hydrocarbons. The greater ambition of the technology is to upcycle $CO_2$ emissions to close the carbon cycle, but any unreacted $CO_2$ at the cathode will become a dissolved carbon species, which will have the tendency to migrate to the anolyte and be stripped away as gaseous $CO_2$ or precipitate near the cathode.

[61] This results in a loss of the $CO_2$ that ideally would be reacted in order to close the carbon loop. Another case where this transport of carbon species in the system plays a significant role is the formation of anodic $H_2O_2$. For this reaction, the electrolyte composition has implications on the generation and stability of $H_2O_2$. [31, 62] Continually losing dissolved carbon species through this electrolyte depletion mechanism and the resultant pH swing may significantly alter kinetics, in addition to shortening the achievable reaction time.

It may be difficult to find solutions for electrolyte depletion when the use of a rebalancing line is prohibited due to liquid product formation. In-line separation of the liquid product directly following electrolysis would allow for rebalancing. [59] If in-line separation is not possible, sustaining the electrochemical reaction may require injection of alkaline solution to the anolyte. This lowers the concentration of liquid product, but should hopefully keep the carbon species concentration relatively constant, which may help product stability. However, the continual injection of solution to the system cannot be maintained in a fully continuous process. The true solution may rest in switching from porous separators to newer anion exchange membranes that offer superior transport of $OH^-$, but they also indiscriminately transport negatively charged ions, such as $CO_3^{2-}$ and $HCO_3^-$, and the operational stability of these new membranes has not yet reached the necessary targets for commercialization. [63–65] Another solution could be operating at sufficiently low current densities such that $OH^-$ transport is sufficiently fast, but this dramatically lowers the overall chemical production rate. Other promising solutions have been researched to prevent dissolved carbon species crossover, such as the use of bipolar membranes, different cationic species such as $Cs^+$, or even using solid electrolyte between the electrodes, but these solutions introduce additional complications to the scalability and long-term operation of the system and require further study. [48, 66, 67]

## 2.4. Conclusion

We show combined experimental and simulation results to understand the dynamics of ion transport and electrolyte depletion in (bi)carbonate-based electrolyzer systems. The equilibrium reactions of (bi)carbonate electrolyte provide a source of $OH^-$ anions that can sustain the anodic reactions, but this results in continual depletion of anolyte species. While the first equilibration of $CO_3^{2-}$ to $HCO_3^-$ occurs readily, the second equilibration of $HCO_3^-$ to $CO_2$ is assisted by the physical gas stripping from the oxygen produced during OER. There is an overall net flux of dissolved carbon species from catholyte to anolyte, as dissolved $CO_3^{2-}$ and $HCO_3^-$ transport over to the anolyte and equilibrate away to provide more $OH^-$ for the anodic reactions. This work highlights the issue of using (bi)carbonate-based electrolyte, which is that the systems are only viable at lab-scale current densities for lab-scale operational times. Solving this issue for commercialization will require new process flows such as in-line separation of products from the electrolyte or new technologies for the separators such as bipolar membranes or solid electrolyte systems.

# 2.A. Appendix - Additional Simulation Results

## 2.A.1. Reservoir Volumes

Figure 2.A.1 shows the simulated electrolyte volumes as a function of time, where the simulations had a stop condition that ended the simulation once the anolyte volume reached 250 mL. The decay is roughly linear, with a sharp decrease at the end for the 7.5 V and 6.5 V cases. This sharp drop-off corresponds to the sharp increase of electrolyte potential difference once depletion occurs, and is in agreement with the drop-off in current shown in Figure 2.4.

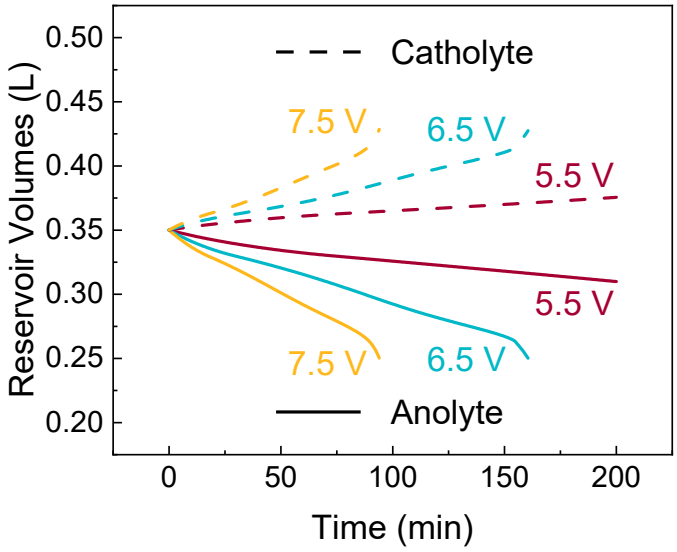


Figure 2.A.1: Plot of simulated electrolyte reservoir volumes over time for simulations at 1 bar, 298.15 K, beginning with 1 M $Na_2CO_3$. The time to simulation end is in rough agreement with the time to experiment end, which was 100 minutes for 7.5 V and 200 minutes for 6.5 V.

## 2.A.2. Current Breakdown by Reaction

Figure 2.A.2 shows the breakdown of simulated current by anodic reaction for 6.5 V and 5.5 V cell potential. Figure 2.A.2a for the case of 6.5 V shares similar behavior as Figure 2.5b, with a decreasing component of $C_2O_6^{2-}$ generation reaction with corresponding increase of OER and anodic oxidation of $H_2O_2$, until only OER remains. But Figure 2.A.2b for the case of 5.5 V looks markedly different. OER is not the dominant current component until approximately 100 minutes, and the $C_2O_6^{2-}$ generation reaction current does not reach zero before the simulation ends. This is likely due to there still being a non-zero concentration of $CO_3^{2-}$ at the anode, which allows the $C_2O_6^{2-}$ reaction to proceed. These concentrations are shown in Figure 2.A.3c.

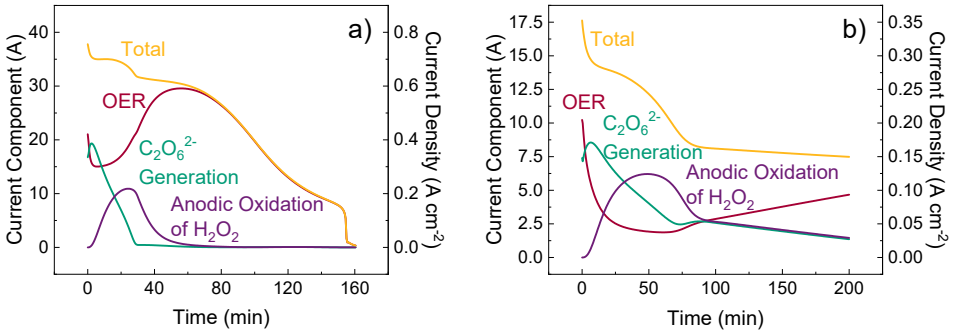


Figure 2.A.2: Plot of the simulated current, decomposed by electrochemical reaction at the anode for a) 6.5 V cell potential and b) 5.5 V cell potential. The simulation conditions are the same as those in Figure 2.5, namely 1 bar and 298.15 K.

## 2.A.3. Reservoir Concentrations

Figures 2.A.3a – 2.A.3d show the simulation results for the relevant species' concentrations at different cell potentials, similar to Figures 2.8a and 2.8b. The time scales for anolyte depletion are different, but we observe the same behavior, namely a quick depletion of $CO_3^{2-}$ followed by a more gradual depletion of $HCO_3^-$. The reason that the current in the simulations at 5.5 V cell potential does not drop to zero within 200 minutes is that the $HCO_3^-$ is not yet fully depleted. Additionally, the concentration of $CO_3^{2-}$ does not reach zero for the case of 5.5 V cell potential, indicating that the transport of $OH^-$ ions to the anode is much closer to a value that could allow for steady-state operation.

## 2.A.4. Mesh Refinement Study

Figures 2.A.4a – 2.A.4d show the mesh refinement study for constraining the maximum element size of both the near-electrode region in the separator as well as the middle of the separator by increasing factors of 2, 5, and 10. The precise details of the meshes can be found in Table 2.A.1. The simulation was run with each of the meshes, and then the (relative) difference between the resulting current and anolyte pH values at 7.5 V were compared to the original coarsest mesh used. While there is a slight convergence to the finest mesh at 10 times the refinement, meaning maximum element sizes of 0.25 nm near the electrode and 0.25 µm in the middle of the separator, the change in values is very small, both in magnitude and as a relative percentage of the original values. Increasing the mesh to 10 times finer also increased computational time from minutes to hours, thereby removing the advantage of a simplified, 1-D geometry. Therefore, the results presented in this work are those using the coarsest mesh.

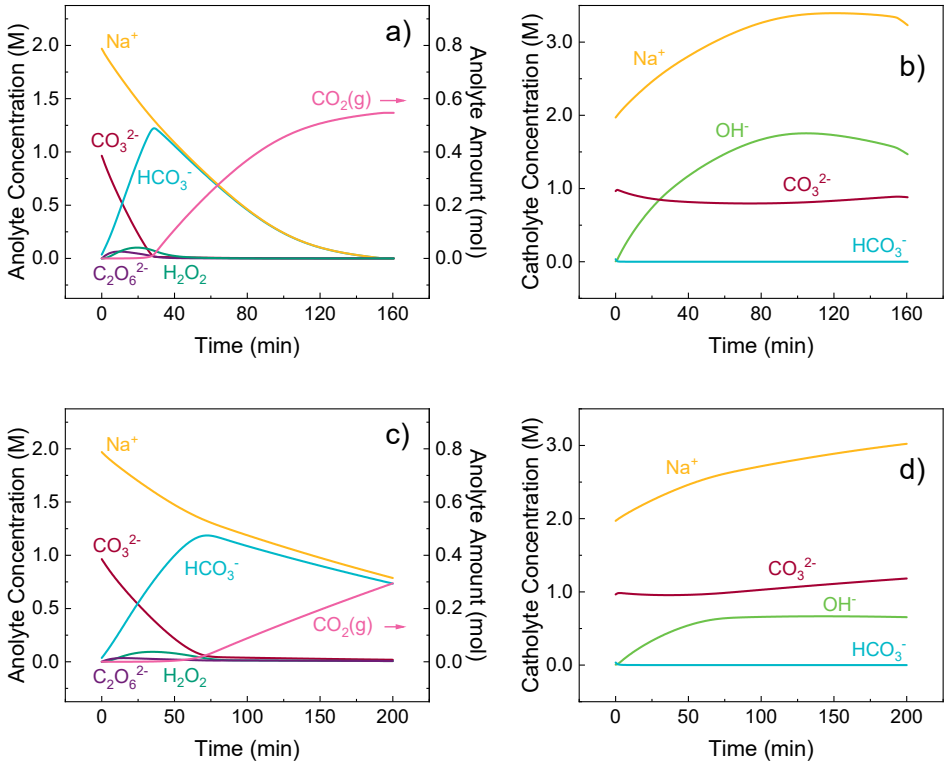


Figure 2.A.3: Simulations of species concentrations in the a) anolyte reservoir for 6.5 V, b) catholyte reservoir for 6.5 V, c) anolyte reservoir for 5.5 V, and d) catholyte reservoir for 5.5 V. The time scales of electrolyte depletion become evident when viewed here, with the 6.5 V case depleting in approximately 165 minutes and the 5.5 V case not yet fully depleted after 200 minutes. The simulation conditions are the same as those in Figure 2.8, namely 1 bar, 298.15 K, and starting with 1 M $Na_2CO_3$.

## 2.A.5. CURRENT PROFILES WITHOUT $CO_2$ STRIPPING

Figure 2.A.5 shows the simulation results of replacing the $CO_2$ stripping term in Equation (2.B.28) with $k_l a_{CO_2,\,degas}(n_{CO_2,\,An} - c_{CO_2,\,sol} V_{An})$, where $k_l a_{CO_2,\,degas}$ is a volumetric mass transfer coefficient of 2 $s^{-1}$ representing the rate of $CO_2$ degassing due to the reaching solubility limit and $c_{CO_2,\,sol}$ is the solubility concentration of $CO_2$ in 0.5 molal $NaHCO_3$ of 23.8 mM (absent data on a 1 M solution). [68] The value of 2 $s^{-1}$ was chosen because it was the highest value of $k_{CO_2} a_g$ reached during the simulations, ensuring that we are comparing the case with $CO_2$ stripping to a case where $CO_2$ removal from solution is not limited by anything other than a concentration difference with solubility. The results show that the passive removal

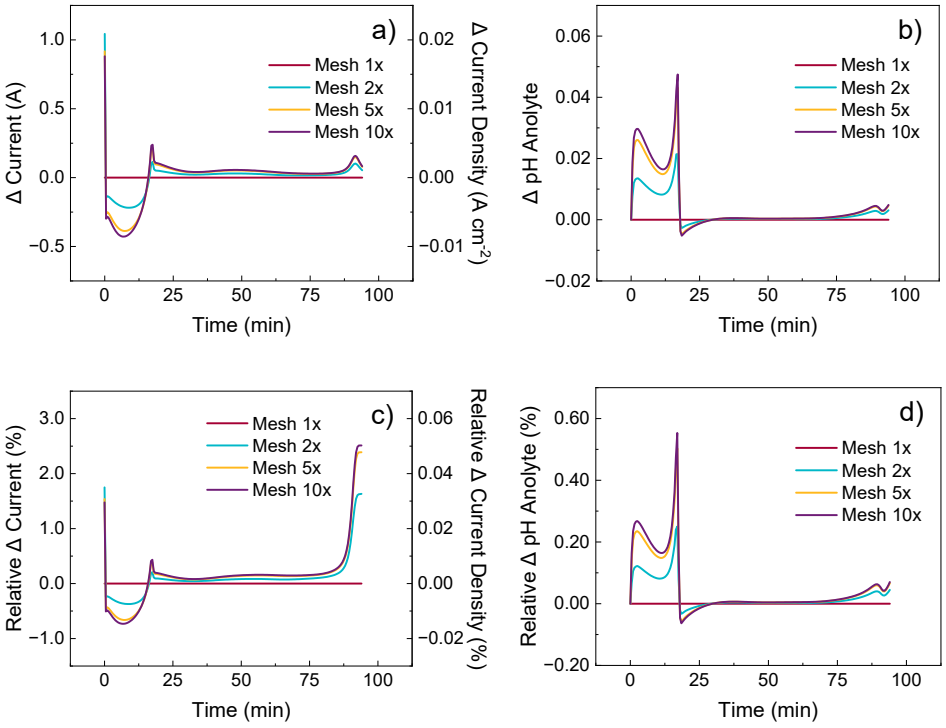


Figure 2.A.4: Mesh refinement study for the case of 7.5 V cell potential, showing the difference over time in a) current, and b) anolyte pH, as well as the relative difference over time in c) current, and d) anolyte pH. The values plotted are comparing the finer meshes (2x, 5x, and 10x) to the coarsest mesh (1x) used for the plots published in Chapter 2. The labels of 1x, 2x, 5x, and 10x, refer to the factor by which the maximum mesh element sizes are reduced, where 10x represents the finest mesh. Their details are shown in Table 2.A.1.

of $CO_2$ due to reaching the solubility limit is insufficient to account for the experimental results. What is observed experimentally and needed in the simulations is a stronger driving force for $CO_2$ removal than simply the dissolved gas concentration exceeding the solubility limit.

Table 2.A.1: List of mesh parameters used in the simulation and from the mesh refinement study, where the results of Chapter 2 are using the coarsest mesh, 1x.

| | 1x | 2x | 5x | 10x |
|---|---|---|---|---|
| Maximum element size in near-electrode regions (nm) | 2.5 | 1.25 | 0.5 | 0.25 |
| Number of mesh elements in near-electrode regions | 120 | 240 | 600 | 1200 |
| Maximum element size in middle of separator (µm) | 2.5 | 1.25 | 0.5 | 0.25 |
| Number of mesh elements in middle of separator | 325 | 649 | 1622 | 3244 |
| Total number of mesh elements | 445 | 889 | 2222 | 4444 |

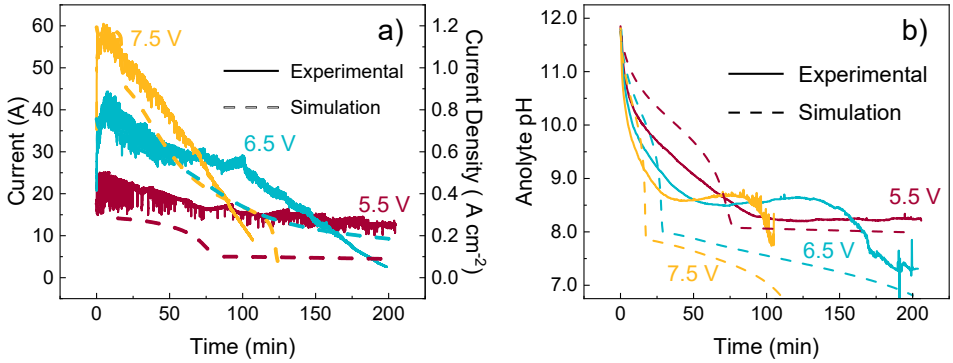


Figure 2.A.5: Plot of a) the simulated current and b) the simulated anolyte pH in the case where $CO_2$ simply degasses after reaching the solubility limit rather than being actively removed by physical gas stripping, compared to experimental results. All parameters, including 1 bar pressure, 298.15 K temperature, and beginning with 1 M $Na_2CO_3$, were otherwise kept the same. The agreement of both current and pH versus time is noticeably worse than what is shown in Figures 2.4 and 2.6a. The simulated current lowers too early compared to the experimental results and the anolyte pH is overall far too low.

## 2.B. Appendix - Simulation Details

### 2.B.1. Model Geometry and Operating Parameters

By reducing the simulation from 3-D to 1-D, the complexity of the simulation is greatly reduced. Some of the details of the 3-D experimental geometry must still be included in order to properly evaluate the system. The temperature and pressure were also kept constant throughout the simulation. These parameters are included in Table 2.B.1.

Table 2.B.1: List of the geometric and operating parameters used in the simulation

| Symbol | Parameter | Value | Unit |
|---|---|---|---|
| $A_{Elec}$ | Geometric electrode surface area | 60 | $cm^2$ |
| $V_{An,\,Start}$ | Initial anolyte volume | 0.35 | L |
| $V_{Cath,\,Start}$ | Initial catholyte volume | 0.35 | L |
| $L_{Sep}$ | Separator length | 500 | µm |
| $l_x$ | Electrode chamber thickness | 5 | mm |
| $l_y$ | Electrode chamber width | 10 | cm |
| $l_z$ | Electrode height | 5 | cm |
| $T$ | Temperature | 298.15 | K |
| $P$ | Pressure | 1 | bar |

### 2.B.2. Model Homogeneous Reaction Kinetics

For numerical convergence, the majority of the chemical reactions were modeled in terms of the concentrations of $H^+$. The formulations used in the model and their corresponding homogeneous reaction rate expressions are shown in Equations (2.B.1) – (2.B.6). In Equation (2.B.1), carbonic acid ($H_2CO_3$) has been rewritten as $CO_2$ + $H_2O$, as carbonic acid quickly dissociates at standard conditions. Table 2.B.2 shows the reaction rate constants for the listed homogeneous reactions.

$$CO_2 + H_2O \rightleftharpoons HCO_3^- + H^+ \; ; \; r_1 = k_1 c_{CO_2} - k_{-1} c_{HCO_3^-} c_{H^+} \tag{2.B.1}$$

$$HCO_3^- \rightleftharpoons CO_3^{2-} + H^+ \; ; \; r_2 = k_2 c_{HCO_3^-} - k_{-2} c_{CO_3^{2-}} c_{H^+} \tag{2.B.2}$$

$$H_2O \rightleftharpoons OH^- + H^+ \; ; \; r_w = k_w - k_{-w} c_{OH^-} c_{H^+} \tag{2.B.3}$$

$$C_2O_6^{2-} + 2\,H_2O \rightarrow 2\,HCO_3^- + H_2O_2 \; ; \; r_3 = k_3 c_{C_2O_6^{2-}} \tag{2.B.4}$$

$$2\,H_2O_2 \rightarrow 2\,H_2O + O_2 \; ; \; r_4 = k_4 c_{H_2O_2} \tag{2.B.5}$$

$$H_2O_2 \rightleftharpoons HO_2^- + H^+ \; ; \; r_5 = k_{H_2O_2} c_{H_2O_2} - k_{-H_2O_2} c_{HO_2^-} c_{H^+} \tag{2.B.6}$$

Table 2.B.2: List of the homogeneous reaction rate constants used in the simulation

| Symbol | Parameter | Value | Unit | Reference |
|---|---|---|---|---|
| | $CO_2 + H_2O \rightleftharpoons HCO_3^- + H^+$ | | | |
| $pKa_1$ | pKa of $H_2CO_3$ | 6.37 | - | [57] |
| $K_{eq,\,1}$ | Acid dissociation constant = $10^{-pKa_1}$ | $4.265\times10^{-4}$ | mol $m^{-3}$ | [57] |
| $k_1$ | Forward rate constant | $3.71\times10^{-2}$ | $s^{-1}$ | [69] |
| $k_{-1}$ | Reverse rate constant = $\frac{k_1}{K_{eq,\,1}}$ | 86.971 | $m^3\ s^{-1}\ mol^{-1}$ | – |
| | $HCO_3^- \rightleftharpoons CO_3^{2-} + H^+$ | | | |
| $pKa_2$ | pKa of $HCO_3^-$ | 10.32 | - | [57] |
| $K_{eq,\,2}$ | Acid dissociation constant = $10^{-pKa_2}$ | $4.786\times10^{-8}$ | mol $m^{-3}$ | [57] |
| $k_2$ | Forward rate constant | 59.44 | $s^{-1}$ | [69] |
| $k_{-2}$ | Reverse rate constant = $\frac{k_2}{K_{eq,\,2}}$ | $1.242\times10^{9}$ | $m^3\ s^{-1}\ mol^{-1}$ | – |
| | $H_2O \rightleftharpoons OH^- + H^+$ | | | |
| $K_{eq,\,w}$ | Water dissociation constant | $1\times10^{-8}$ | $mol^2\ m^{-6}$ | – |
| $k_w$ | Forward rate constant | 1 | mol $m^{-3}\ s^{-1}$ | [69] |
| $k_{-w}$ | Reverse rate constant = $\frac{k_w}{K_{eq,\,w}}$ | $1\times10^{8}$ | $m^3\ s^{-1}\ mol^{-1}$ | – |
| | $C_2O_6^{2-} + 2\,H_2O \rightarrow 2\,HCO_3^- + H_2O_2$ | | | |
| $k_3$ | Reaction rate constant | $3.33\times10^{-3}$ | $s^{-1}$ | – |
| | $2\,H_2O_2 \rightarrow 2\,H_2O + O_2$ | | | |
| $k_4$ | Reaction rate constant | $3.083\times10^{-5}$ | $s^{-1}$ | [62] |
| | $H_2O_2 \rightleftharpoons HO_2^- + H^+$ | | | |
| $pKa_{H_2O_2}$ | pKa of $H_2O_2$ | 11.6 | - | – |
| $K_{a,\,H_2O_2}$ | Acid dissociation constant = $10^{-pKa_{H_2O_2}}$ | $2.51\times10^{-9}$ | mol $m^{-3}$ | – |
| $k_{H_2O_2}$ | Forward rate constant | $2.5\times10^{2}$ | $s^{-1}$ | – |
| $k_{-H_2O_2}$ | Reverse rate constant = $\frac{k_{H_2O_2}}{K_{a,\,H_2O_2}}$ | $9.95\times10^{10}$ | $m^3\ s^{-1}\ mol^{-1}$ | – |

### 2.B.3. MODEL INITIAL CONCENTRATIONS

The starting concentrations of ions in electrolyte were determined by using the initial pH value, the initial concentration of carbon species in the electrolyte, and the equilibrium relationships of the carbonate system. Equations (2.B.7) and (2.B.8) show how the starting $H^+$ and $OH^-$ concentrations are found using the starting pH. Equations (2.B.9) – (2.B.11) show how the initial concentration of carbon species was calculated. The starting concentration of sodium was calculated using Equation (2.B.12) by balancing the excess negative charge from all of the other ionic species. The starting amount of species in moles for the reservoirs was calculated by multiplying the starting concentrations, shown in Table 2.B.3, with the initial reservoir volumes shown in Table 2.B.1.

$$c_{H^+,\,\mathrm{Start}} = 10^{\mathrm{pH_{Start}}} \tag{2.B.7}$$

$$c_{OH^-,\,\mathrm{Start}} = 10^{\mathrm{pH_{Start}}-14} \tag{2.B.8}$$

$$c_{CO_3^{2-},\,\mathrm{Start}} = \frac{K_{eq,\,1}K_{eq,\,2}}{c_{H^+,\,\mathrm{Start}}^2 + K_{eq,\,1}c_{H^+,\,\mathrm{Start}} + K_{eq,\,1}K_{eq,\,2}}c_{\mathrm{Carbon}} \tag{2.B.9}$$

$$c_{HCO_3^-,\,\mathrm{Start}} = \frac{K_{eq,\,1}c_{H^+,\,\mathrm{Start}}}{c_{H^+,\,\mathrm{Start}}^2 + K_{eq,\,1}c_{H^+,\,\mathrm{Start}} + K_{eq,\,1}K_{eq,\,2}}c_{\mathrm{Carbon}} \tag{2.B.10}$$

$$c_{CO_2,\,\mathrm{Start}} = \frac{c_{H^+,\,\mathrm{Start}}^2}{c_{H^+,\,\mathrm{Start}}^2 + K_{eq,\,1}c_{H^+,\,\mathrm{Start}} + K_{eq,\,1}K_{eq,\,2}}c_{\mathrm{Carbon}} \tag{2.B.11}$$

$$c_{Na^+,\,\mathrm{Start}} = \sum_i -\nu_i c_{i,\,\mathrm{Start}} \tag{2.B.12}$$

### 2.B.4. MODEL ELECTROCHEMISTRY

The equilibrium potentials were determined by the Nernst Equation shown in Equation (2.B.13).

$$E_{eq,\,i} = E_{eq,\,\mathrm{ref},\,i} - \frac{RT}{n\mathcal{F}}\prod_i\left(\frac{c_i}{c_{i,\,\mathrm{ref}}}\right)^{\nu_i} \tag{2.B.13}$$

Reference concentrations were taken to be 1 M for all species, $R$ is the ideal gas constant, $n$ is the number of electrons involved in the reaction, $\mathcal{F}$ is Faraday's constant, and $\nu_i$ is the stoichiometric coefficient of the species involved in the reaction.

The electrochemical kinetics were determined using the Butler-Volmer Equation, shown in Equation (2.B.14).

$$j = j_0\left(e^{\frac{\alpha_a\mathcal{F}\eta}{RT}} - e^{\frac{-\alpha_c\mathcal{F}\eta}{RT}}\right) \tag{2.B.14}$$

Table 2.B.3: List of the starting concentrations used in the simulation

| Symbol | Parameter | Value | Unit |
|---|---|---|---|
| $pH_{Start}$ | Initial electrolyte pH | 11.75 | - |
| $c_{Carbon}$ | Concentration of dissolved carbon | 1 | M |
| $c_{H^+,\,Start}$ | Initial concentration of $H^+$ | $1.778\times10^{-6}$ | M |
| $c_{OH^-,\,Start}$ | Initial concentration of $OH^-$ | $5.623\times10^{-3}$ | M |
| $c_{CO_3^{2-},\,Start}$ | Initial concentration of $CO_3^{2-}$ | 0.964 | M |
| $c_{HCO_3^-,\,Start}$ | Initial concentration of $HCO_3^-$ | 0.036 | M |
| $c_{CO_2,\,Start}$ | Initial concentration of $CO_2$ | $1.49\times10^{-7}$ | M |
| $c_{Na^+,\,Start}$ | Initial concentration of $Na^+$ | 1.970 | M |
| $c_{C_2O_6^{2-},\,Start}$ | Initial concentration of $C_2O_6^{2-}$ | 0 | M |
| $c_{H_2O_2,\,Start}$ | Initial concentration of $H_2O_2$ | 0 | M |
| $c_{HO_2^-,\,Start}$ | Initial concentration of $HO_2^-$ | 0 | M |

In Equation (2.B.14), $j$ is the current density, and $\eta$ is the overpotential of the reaction calculated internally based on the applied electrode potentials and equilibrium potentials of the reactions. Table 2.B.4 shows the values for the electrochemical kinetics used. It should be noted that the anodic electrochemical reactions were also written in terms of $H^+$ to improve numerical convergence. Due to the complex electrochemical reaction network, it was difficult to find precise values for each reaction on BDD, so values other than $E_{eq,\,ref}$ were tuned to achieve better agreement with experiments. The values of $\alpha_a$ and $\alpha_c$ deviating from 0.5 and the low values of $j_0$ reflect BDD's notoriously sluggish kinetics.

The initial electrolyte potential was set as linearly decreasing from 0.7 V to 0.15 V across the length of the 1-D domain, from anode to cathode. This initial electrolyte potential profile was set to improve convergence and matches closely with the initial electrolyte potential difference at 7.5 V.

## 2.B.5. Model Species Transport

### Diffusive Transport

The 1-D domain is modeled as a medium with a porosity, $\varepsilon$, and the effective diffusivity, $D_{i,Eff}$, is calculated by using Bruggeman's relation, shown in Equation (2.B.15).

$$D_{i,Eff} = \varepsilon^{3/2} D_i \tag{2.B.15}$$

In Equation (2.B.15), $D_i$ is the molecular diffusivity of the species in $H_2O$, and the factor of 3/2 appears due to factoring in the porosity and tortuosity of the porous medium. Table 2.B.5 shows the values of the molecular diffusivities used in the model.

Table 2.B.4: List of the electrochemical parameters used in the simulation. The anodic reactions' exchange current densities are multiplied by a concentration factor following the simplified form from Kulikovsky in the case of reactions far from equilibrium. [70]

| Symbol | Parameter | Value | Unit |
|---|---|---|---|
| | **Oxygen Evolution Reaction** | | |
| $E_{eq,\,ref}$ | Equilibrium reference potential | 1.23 | V vs SHE |
| $j_0$ | Exchange current density | $1\times10^{-8}\times\frac{c_{OH^-}}{c_{OH^-,\,Start}}$ | A m$^{-2}$ |
| $\alpha_a$ | Anodic charge transfer coefficient | 0.22 | – |
| $\alpha_c$ | Cathodic charge transfer coefficient = 1 - $\alpha_a$ | 0.78 | – |
| | **$C_2O_6^{2-}$ Generation Reaction** | | |
| $E_{eq,\,ref}$ | Equilibrium reference potential | 2.00 | V vs SHE |
| $j_0$ | Exchange current density | $4\times10^{-5}\times\frac{c_{CO_3^{2-}}}{c_{CO_3^{2-},\,Start}}$ | A m$^{-2}$ |
| $\alpha_a$ | Anodic charge transfer coefficient | 0.23 | – |
| $\alpha_c$ | Cathodic charge transfer coefficient = 1 - $\alpha_a$ | 0.77 | – |
| | **Anodic Oxidation of $H_2O_2$** | | |
| $E_{eq,\,ref}$ | Equilibrium reference potential | 0.67 | V vs SHE |
| $j_0$ | Exchange current density | $4\times10^{-9}\times\frac{c_{H_2O_2}}{c_{H_2O_2,\,ref}}$ | A m$^{-2}$ |
| $\alpha_a$ | Anodic charge transfer coefficient | 0.20 | – |
| $\alpha_c$ | Cathodic charge transfer coefficient = 1 - $\alpha_a$ | 0.80 | – |
| | **Hydrogen Evolution Reaction** | | |
| $E_{eq,\,ref}$ | Equilibrium reference potential | 0.00 | V vs SHE |
| $j_0$ | Exchange current density | $1.16\times10^{-2}$ | A m$^{-2}$ |
| $\alpha_a$ | Anodic charge transfer coefficient = 1 - $\alpha_c$ | 0.70 | – |
| $\alpha_c$ | Cathodic charge transfer coefficient | 0.30 | – |
| | **Electrical Circuit Parameters** | | |
| $E_{Circuit}$ | Externally applied voltage | 5.5, 6.5, 7.5 | V |
| $E_{Cath}$ | Electrode potential on cathode | -1 | V |
| $E_{An}$ | Electrode potential on anode = $E_{Circuit}$ + $E_{Cath}$ | 4.5, 5.5, 6.5 | V |
| $R_{ohmic}$ | External ohmic resistance | 0.015 | Ω |
| $\hat{R}_{Film}$ | Film resistance = $R_{ohmic}$ × $A_{Elec}$ | $9\times10^{-5}$ | Ω·m$^2$ |

Table 2.B.5: List of the molecular diffusivities for the species in the simulation. Some species are short-lived ($C_2O_6^{2-}$) or their diffusivities are not listed ($HO_2^-$). In these cases, the value was copied from another relevant species ($CO_3^{2-}$ and $H_2O_2$, respectively).

| Symbol | Parameter | Value | Unit | Reference |
|---|---|---|---|---|
| $\varepsilon$ | Porosity | 0.5 | - | – |
| $D_{H^+}$ | Molecular diffusivity of $H^+$ | $9.312\times10^{-9}$ | $m^2\ s^{-1}$ | [71] |
| $D_{OH^-}$ | Molecular diffusivity of $OH^-$ | $5.260\times10^{-9}$ | $m^2\ s^{-1}$ | [71] |
| $D_{CO_3^{2-}}$ | Molecular diffusivity of $CO_3^{2-}$ | $8.050\times10^{-10}$ | $m^2\ s^{-1}$ | [72] |
| $D_{HCO_3^-}$ | Molecular diffusivity of $HCO_3^-$ | $1.105\times10^{-9}$ | $m^2\ s^{-1}$ | [71] |
| $D_{CO_2}$ | Molecular diffusivity of $CO_2$ | $1.910\times10^{-9}$ | $m^2\ s^{-1}$ | [73] |
| $D_{Na^+}$ | Molecular diffusivity of $Na^+$ | $1.334\times10^{-9}$ | $m^2\ s^{-1}$ | [71] |
| $D_{C_2O_6^{2-}}$ | Molecular diffusivity of $C_2O_6^{2-}$ | $8.050\times10^{-10}$ | $m^2\ s^{-1}$ | $D_{CO_3^{2-}}$ |
| $D_{H_2O_2}$ | Molecular diffusivity of $H_2O_2$ | $1.389\times10^{-9}$ | $m^2\ s^{-1}$ | [74] |
| $D_{HO_2^-}$ | Molecular diffusivity of $HO_2^-$ | $1.389\times10^{-9}$ | $m^2\ s^{-1}$ | $D_{H_2O_2}$ |

### Migrative transport

The electrical mobility of the individual species was determined by the Nernst-Einstein relation, shown in Equation (2.B.16).

$$\mu_i = \frac{D_{i,\,\mathrm{Eff}}}{RT} \tag{2.B.16}$$

### Convective transport

The electro-osmotic mobility, $\mathcal{M}$, was calculated by using the Helmholtz-Smoluchowski equation assuming no pressure gradients across the porous separator. This is shown in Equation (2.B.17), where $\epsilon_0$ is the permittivity of free space. The other parameters are shown in Table 2.B.6. The values depend strongly on the surface and electrolyte in question and are not well-defined for 1 M $Na_2CO_3$ electrolyte with Zirfon Perl UTP 500, so values in a typical order of magnitude were chosen and tuned to match experiments. For comparison, the effective values of $\zeta$ and $\epsilon_r$ for 1 M KOH electrolyte and Zirfon Perl UTP 500 reported by Haverkort and Rajaei were 15 mV and 77, respectively, when incorporating porosity and tortuosity. These values were based on fitting of $\mathcal{M}$ using a version of Equation (2.B.17) without a dependence on porosity and tortuosity. [41] The electro-osmotic velocity was then calculated by multiplying the electro-osmotic mobility with the electrolyte potential gradient, as shown in Equation (2.B.18).

$$\mathcal{M} = \frac{\varepsilon^{3/2}\epsilon_r\epsilon_0\zeta}{\mu} \tag{2.B.17}$$

$$u = -\mathcal{M}\nabla\phi \tag{2.B.18}$$



Table 2.B.6: List of the parameters used to calculate electro-osmotic flow.

| Symbol | Parameter | Value | Unit |
|---|---|---|---|
| $\epsilon_r$ | Relative permittivity | 60 | – |
| $\zeta$ | Zeta potential | 20 | mV |
| $\mu$ | Electrolyte viscosity | $1\times10^{-3}$ | Pa s |

## 2.B.6. Model $CO_2$ Stripping

The physical stripping of dissolved $CO_2$ was included in the model by using the analytical relations from Haverkort shown in Equations (2.B.19) – (2.B.28). [75] Using the Stokes rise velocity ($w_S$) of a bubble from Equation (2.B.19), the Reynolds number of a bubble ($Re_b$) and the Schmidt number of the electrolyte (Sc) can be calculated as per Equations (2.B.20) and (2.B.21). The correlation of Ranz and Marshall in Equation (2.B.22) gives the Sherwood number (Sh), which can be used to find the mass transfer coefficient of $CO_2$ into a bubble, $k_{l,\,CO_2}$, using Equation (2.B.23). Next, the current density going to produce gas bubbles by electrochemical reactions, $j_{Gas}$, is calculated using Equation (2.B.24). Using the geometry of the system and the above calculated values, a critical height, $z_c$, and average gas fraction, $\varepsilon_{g,\,Avg}$, can be found using Equations (2.B.25) and (2.B.26), respectively. Then, the surface area to volume ratio, $a_g$, for a volume with an average gas fraction and fixed bubble diameter is given by Equation (2.B.27). Finally, the terms are combined with the anolyte reservoir $CO_2$ amount to give a $CO_2$ stripping rate, $\dot{n}_{CO_2\,strip}$, in Equation (2.B.28). Equation (2.B.29) models the gradual uptake of atmospheric $CO_2$ into the catholyte reservoir more simply, using a mass transfer coefficient of a reasonable order of magnitude for a stirred reservoir, a concentration difference based on $CO_2$ solubility, and the surface area of the reservoir that was in contact with the atmosphere. Equations (2.B.28) and (2.B.29) are the extra terms added to Equation (2.16) to account for the movement of $CO_2$(g). The parameters used are shown in Table 2.B.7.

$$w_S = \frac{d_b^2 g \Delta\rho}{18\mu} \tag{2.B.19}$$

$$Re_b = \frac{\Delta\rho w_S d_b}{\mu} \tag{2.B.20}$$

$$Sc = \frac{\mu}{\rho_l D_{CO_2}} \tag{2.B.21}$$

$$Sh = 2 + 0.6 Re_b^{1/2} Sc^{1/3} \tag{2.B.22}$$

$$k_{l,\,CO_2} = \frac{D_{CO_2}\mathrm{Sh}}{d_b} \tag{2.B.23}$$

$$j_{Gas} = \frac{j_{OER}}{n_{OER}} + \frac{j_{H_2O_2\ An\ Ox}}{n_{H_2O_2\ An\ Ox}} \tag{2.B.24}$$

$$z_c = \frac{\varepsilon_{g,\,Max} l_x (w_S + W_l)}{j_{Gas} \mathcal{V}_m / \mathcal{F}} \tag{2.B.25}$$

$$\varepsilon_{g,\,Avg} = \varepsilon_{g,\,Max} \frac{l_z/(2z_c)}{1 + l_z/(2z_c)} \tag{2.B.26}$$

$$a_g = \frac{6\varepsilon_{g,\,Avg}}{d_b} \tag{2.B.27}$$

$$\dot{n}_{CO_2\ strip} = -k_{l,\,CO_2} \left(n_{CO_2,\,An}\right) a_g \tag{2.B.28}$$

$$\dot{n}_{CO_2\ uptake} = k_{l,\,CO_2\ uptake} \left( c_{CO_2,\,Sol} - \frac{n_{CO_2,\,Cath}}{V_{Cath}} \right) A_{Res} \tag{2.B.29}$$

Table 2.B.7: List of the parameters used to calculate $CO_2$ stripping rates. Some of the other necessary parameters relating to geometry can be found in Table 2.B.1.

| Symbol | Parameter | Value | Unit |
|---|---|---|---|
| $d_b$ | $O_2$ gas bubble diameter | 80 | µm |
| $g$ | Acceleration of gravity | 9.8 | m $s^{-2}$ |
| $\Delta\rho$ | $O_2$-Electrolyte density difference | 1000 | kg $m^{-3}$ |
| $\rho_l$ | Electrolyte density | 1000 | kg $m^{-3}$ |
| $\varepsilon_{g,\,Max}$ | Maximum gas fraction | 1 | – |
| $W_l$ | Vertical liquid velocity in electrolyzer chamber | 8.33 | mm $s^{-1}$ |
| $\mathcal{V}_m$ | Molar volume of gas at 298.15 K, 1 bar | 24.79 | L $mol^{-1}$ |
| $k_{l,\,CO_2\ uptake}$ | $CO_2$ uptake mass transfer coefficient | $1\times10^{-4}$ | m $s^{-1}$ |
| $c_{CO_2,\,Sol}$ | $CO_2$ solubility concentration in water | 32.95 | mM |
| $A_{Res}$ | Reservoir-Atmosphere interface area | 70 | $cm^2$ |

# 3

# ACCUMULATING HYDROGEN PEROXIDE AT LABORATORY SCALE


## ABSTRACT

The anodic co-production of hydrogen peroxide ($H_2O_2$) during alkaline water electrolysis has gained interest as a sustainable alternative for anthraquinone oxidation. However, electrochemical $H_2O_2$ production is often studied with idealized laboratory setups to determine the $H_2O_2$ formation kinetics. In this work, we perform the reaction with industrially relevant operating principles using a flow cell with separately recirculating anolyte and catholyte. We then fit the data to an analytical model that we derive based on mole balances that accounts for anodic generation, anodic oxidation, and bulk disproportionation of $H_2O_2$, as well as electrolyte volumes and electrode surface area. We performed experiments at 100, 200, and 300 mA $cm^{-2}$ to derive values for the reaction system. At 200 mA $cm^{-2}$, we found a generation rate of 0.037 mmol $min^{-1}$ $cm^{-2}$ ($FE_{H_2O_2}$ = 59%) and an anodic decomposition rate constant of 0.304 cm $min^{-1}$, with a bulk disproportionation rate constant of $1.85 \times 10^{-3}$ $min^{-1}$. We successfully applied our model to two sources in literature to derive values for their systems as well. In all cases, the contribution of anodic oxidation of $H_2O_2$ was found to be the larger loss mechanism in comparison to bulk disproportionation. Using the analytical model, we show that decreasing the reservoir volume is a simple way to increase the $H_2O_2$ concentration over time. Further refinement of the model can be achieved through the use of mass transfer relationships based



The work in this chapter has been published as S. A. Phadke, W. de Jong and J. W. Haverkort. 'An experimentally validated model for anodic $H_2O_2$ production in alkaline water electrolysis and its implications for scaled-up operation'. In: *Electrochimica Acta* 491 (2024), p. 144258. DOI: 10.1016/j.electacta.2024.144258 [76]

on electrolyzer geometries to describe the anodic oxidation of $H_2O_2$ in the mole balance equations.

## 3.1. Introduction

The use of electrochemistry, when powered by renewable energy resources, offers a promising pathway for the sustainable production of chemicals. One of these chemicals that requires a more sustainable pathway is hydrogen peroxide ($H_2O_2$), which is used as a green oxidant in industries such as paper milling and textile bleaching. [12, 77] However, it is currently produced by the anthraquinone oxidation process, which has a large energy demand of 17.6 kWh $kg^{-1}$ due to high solvent use and separation requirements. [13, 78, 79] A more sustainable route would be via alkaline water electrolysis. During alkaline water electrolysis, we typically produce hydrogen gas ($H_2$) at the cathode and oxygen gas ($O_2$) at the anode. [80] While research into the cathodic co-production of $H_2O_2$ via oxygen reduction reaction is more commonly investigated, cathodically produced $H_2O_2$ has some notable drawbacks. One drawback is that in order to effectively deliver oxygen to the cathode, a more complex gas-diffusion electron must be used, which can lead to mass transfer limitations. The other issue is that in cathodic $H_2O_2$ production, the valuable $H_2$ product is replaced, and the anode still produces low-value $O_2$. [81] A more attractive alternative is to instead electrochemically produce $H_2O_2$ at the anode by carefully selecting the anode material and electrolyte. [15] This form of paired electrolysis makes use of both the cathode, by producing a valuable, carbon-free energy carrier in $H_2$, and of the anode, by producing a high-value commodity chemical in $H_2O_2$ alongside $O_2$.

The main difficulty of anodic $H_2O_2$ production is that the potential required to produce $H_2O_2$ is higher than that required to produce $O_2$. The thermodynamic half cell potential to produce $H_2O_2$ under alkaline conditions as per Equation (3.1.1) is 1.76 V versus the Reversible Hydrogen Electrode (RHE). Because the thermodynamic half cell potential to produce $O_2$ is only 1.23 V versus RHE as per Equation (3.1.2), the generation of $H_2O_2$ at the anode is always in competition with the formation of $O_2$. While different anode materials may display different selectivities towards $H_2O_2$ generation over $O_2$ evolution, there is still no reported material with 100% faradaic efficiency to $H_2O_2$.

Much of the research into anodic $H_2O_2$ production focuses on finding more selective anode materials or on elucidating the reaction mechanism. [16, 20, 22, 31, 82] In either case, experiments are typically performed in a one-compartment cell or in a separated H-cell configuration to study the fundamental anode performance over time. [18, 83, 84] Experiments are also often performed with refreshed anolyte, or single-pass anolyte in the case of flow cells, to avoid the effect of $H_2O_2$ loss mechanisms. [21, 85] A cation exchange membrane such as Nafion 117 is also frequently used, presumably to prevent $H_2O_2$ crossover to the catholyte. However, this would be inadvisable for an alkaline electrolyzer system as it inhibits the transport of hydroxide ($OH^-$) anions, which allow the reaction to proceed. In order to scale up a system for industrial electrochemical $H_2O_2$ production, we must examine how the

system behaves with more relevant industrial operating conditions, which include separately recirculating electrolyte flows, a porous separator material, and constant pH and temperature throughout the reaction.

For example, operating a flow cell with single-pass anolyte using high flow rates yields an anolyte product stream with very low $H_2O_2$ concentration. This low concentration results in a more difficult downstream separation to extract the product. One could feed anolyte at lower flow rates to achieve a higher concentration, but the total $H_2O_2$ production rate would then be lower. Such lower flow rates come with the drawback of the unavoidable loss mechanisms, namely the anodic oxidation of $H_2O_2$ as per Equation (3.1.3) at 0.67 V versus RHE, and the disproportionation of $H_2O_2$ in bulk electrolyte as per Equation (3.1.4). One solution would be recirculating the anolyte at high flow rates for some time before the separation stage, thus increasing $H_2O_2$ concentration over time, easing downstream separation, and reducing cost. However, recirculating anolyte comes with the same unavoidable loss mechanisms. As $H_2O_2$-charged anolyte recirculates past the anode, the chance for anodic oxidation of the $H_2O_2$ increases. Additionally, the increased time for recirculation increases the time for bulk disproportionation to occur in the anolyte reservoir, further decreasing the achieved $H_2O_2$ concentration. Therefore, we must study how the network of reactions behaves in the relevant case. This network of reactions is shown schematically in Figure 3.1.1.



$$2\,OH^- \rightarrow H_2O_2 + 2\,e^- \qquad E^\circ = 1.76\ \text{V versus RHE} \qquad (3.1.1)$$

$$4\,OH^- \rightarrow 2\,H_2O + O_2 + 4\,e^- \qquad E^\circ = 1.23\ \text{V versus RHE} \qquad (3.1.2)$$

$$H_2O_2 + 2\,OH^- \rightarrow 2\,H_2O + O_2 + 2\,e^- \qquad E^\circ = 0.67\ \text{V versus RHE} \qquad (3.1.3)$$

$$2\,H_2O_2 \rightarrow 2\,H_2O + O_2 \qquad (3.1.4)$$

In this work, we study an industrially relevant electrolyzer system that separately recirculates anolyte and catholyte, and includes the standard porous separator material used in alkaline water electrolysis, Zirfon Perl UTP 500. We formulate a system of transient mole balance equations for the process and perform experiments to derive individual terms of the mole balance equations. The terms we derive experimentally are the generation rate of $H_2O_2$ and the rate constant of bulk disproportionation of $H_2O_2$ in the electrolyte. We then fit our experimental data to the analytical solution of the mole balance equations, which provides the rate constant for the oxidation of $H_2O_2$ at the anode. We repeat this analysis using data from two references in literature that perform the reaction in a similar manner. Lastly, we simulate a change in design parameters to inform our recommendations on reactor and system design.

## 3.2. Analytical Model for $H_2O_2$ Accumulation

### 3.2.1. List of Symbols

Table 3.2.1 lists the variables used in this chapter and their accompanying units, chosen for better comparison with literature values.

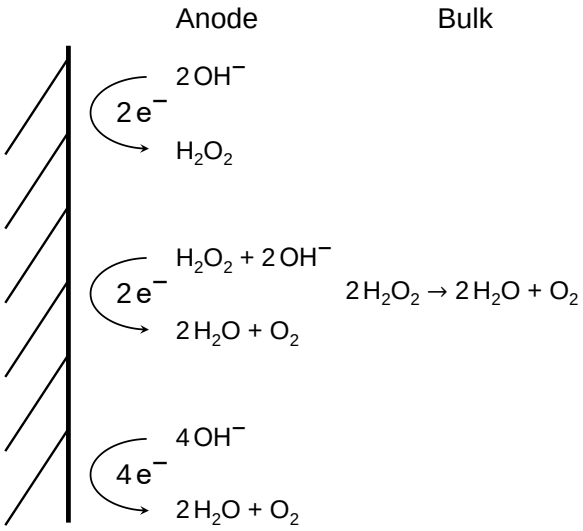


Figure 3.1.1: A simplified schematic of the reactions detailed in Equations (3.1.1) – (3.1.4) occurring in the anode chamber of the electrolyzer, with the anode wall on the left.

### 3.2.2. MOLE BALANCE EQUATIONS

We follow the analysis method outlined by Pickett involving two separate mole balances, one over the electrolyzer, and the other over the electrolyte reservoir. [86] In our analysis, we interchangeably use the terms "electrolyzer" and "electrolyzer volume" to denote the anode chamber and the volume of the anode chamber, because they are the system under investigation. A simplified diagram of the system is shown in Figure 3.2.1. The mole balance over the electrolyzer is written in Equation (3.2.1),

$$V_E \frac{dc_{\text{out}}}{dt} = \dot{Q}c_{\text{in}} - \dot{Q}c_{\text{out}} + SA_{\text{Elec}} - k_a A_{\text{Elec}} c_{\text{out}} - k_b V_E c_{\text{out}} \tag{3.2.1}$$

where $V_E$ in L is the volume of the anode chamber, $c_{\text{out}}(t)$ in mM is the concentration of $H_2O_2$ out of the electrolyzer, $t$ in min is time, $\dot{Q}$ in L min$^{-1}$ is the volumetric flow rate of electrolyte, $c_{\text{in}}(t)$ in mM is the concentration of $H_2O_2$ going into the electrolyzer, $S$ in mmol min$^{-1}$ cm$^{-2}$ is the constant anodic generation rate of $H_2O_2$, $A_{\text{Elec}}$ in cm$^2$ is the geometric anode surface area, $k_a$ in cm min$^{-1}$ is the rate constant for anodic oxidation of $H_2O_2$ as per Equation (3.1.3), and $k_b$ in min$^{-1}$ is the rate constant for bulk disproportionation as per Equation (3.1.4). Note that these units require the anodic oxidation term, $k_a A_{\text{Elec}}$, to be multiplied by a conversion factor of 0.001 L cm$^{-3}$, which carries throughout.

A similar mole balance is expressed in Equation (3.2.2) for the change in concentration across the electrolyte reservoir,

Table 3.2.1: List of symbols used in Chapter 3 with units.

| Symbol | Parameter | Units |
|---|---|---|
| $V_E$ | Volume of Anolyte in Anode Chamber | L |
| $V_R$ | Volume of Anolyte in Reservoir | L |
| $V_A$ | Total Anolyte Volume | L |
| $c_{\text{out}}$ | $H_2O_2$ Concentration Out of Electrolyzer | mM |
| $c_{\text{in}}$ | $H_2O_2$ Concentration Into Electrolyzer | mM |
| $t$ | Time | min |
| $\dot{Q}$ | Electrolyte Flow Rate | L $min^{-1}$ |
| $S$ | $H_2O_2$ Generation Rate | mmol $min^{-1}$ $cm^{-2}$ |
| $k_a$ | $H_2O_2$ Anodic Decomposition Rate Constant | cm $min^{-1}$ |
| $k_b$ | $H_2O_2$ Bulk Disproportionation Rate Constant | $min^{-1}$ |
| $k_c$ | $H_2O_2$ Crossover Rate Constant | cm $min^{-1}$ |
| $A_{\text{Elec}}$ | Electrode Area (Geometric) | $cm^2$ |
| $A_{\text{Sep}}$ | Separator Area (Geometric) | $cm^2$ |
| $\xi$ | Extent of Reaction | - |
| $j$ | Current Density | mA $cm^{-2}$ |
| $\text{FE}_{H_2O_2}$ | Faradaic Efficiency to $H_2O_2$ | % |
| $D_{\text{Eff}}$ | Effective Diffusion Coefficient | $cm^2$ $s^{-1}$ |
| $L_{\text{Sep}}$ | Separator Thickness | cm |



$$V_R \frac{dc_{\text{in}}}{dt} = \dot{Q}c_{\text{out}} - \dot{Q}c_{\text{in}} - k_b V_R c_{\text{in}} \tag{3.2.2}$$

where $V_R$ in L is the reservoir volume. The total anolyte volume, $V_A$ in L, is equal to $V_E + V_R$. This definition treats the small volume of electrolyte in the tubing between electrolyzer and reservoir as belonging to the reservoir, and is addressed in Section 3.3.1. The terms involving $S$ and $k_a$ appear only in the electrolyzer mole balance, while the term involving $k_b$ appears in both balances, as bulk disproportionation can occur everywhere.

### 3.2.3. Assumptions

We assume a perfectly mixed anode chamber due to bubble mixing and flow such that the outlet concentration of the electrolyzer, $c_{\text{out}}(t)$, is the concentration everywhere in the anode chamber, including the anode surface. This assumption is acceptable for systems with low single-pass conversion rates, which for our system was between 0.9% and 3.0%, validating the assumption. We similarly assume a perfectly mixed anolyte reservoir, which we achieve experimentally via magnetic stirring. We also assume that $V_A$, $V_E$, $V_R$, and $\dot{Q}$ are constant.

In Equation (3.2.1), we express the anodic oxidation of $H_2O_2$ as a surface reaction described by a first order rate equation using a homogeneous $H_2O_2$ concentration

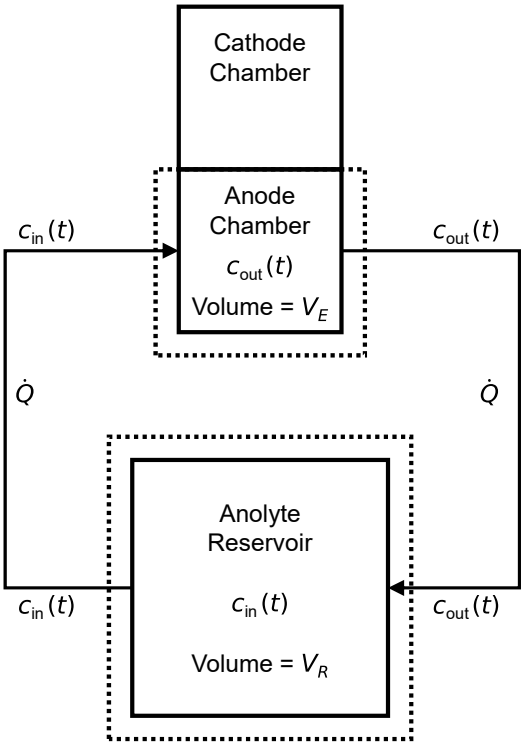


Figure 3.2.1: A simplified diagram of the overall system. The dashed boxes indicate the boundaries of the mole balance equations.

in the electrolyzer. This is a simplifying assumption for a surface concentration that would actually involve a mass transfer term, [80] but it allows us to more easily express the reaction term without involving more complex mass transfer relationships for various electrolyzer geometries. Incidentally, a mass transfer limited reaction would also be expected to be a first order reaction, so this generalized form may cover more than one possible situation.

We assume that only the reactions in Equations (3.1.1) – (3.1.3) take place at the anode. We further assume that $S$ is constant, although in reality there will be a ratio of how much current goes towards $H_2O_2$ generation versus $H_2O_2$ oxidation, $O_2$ evolution, or any other side reactions at the anode. Finally, we assume that there is no loss of $H_2O_2$ due to crossover into the catholyte. This was observed experimentally and further examined in Section 3.4.4.

### 3.2.4. Solutions

Equation (3.2.2) can be rearranged to solve for $c_{out}(t)$ as a function of $c_{in}(t)$, and then differentiated to find an expression for $dc_{out}(t)/dt$ as a function of $c_{in}(t)$. These expressions can be used to eliminate $c_{out}$ from Equation (3.2.1), leading

to the second order, non-homogeneous differential equation in Equation (3.2.3),

$$\frac{d^2c}{dt^2} + \left(\frac{\dot{Q}}{V_E} + \frac{\dot{Q}}{V_R} + \frac{k_a A_{\text{Elec}}}{V_E} + 2k_b\right)\frac{dc}{dt} + \left(\dot{Q}\left(\frac{k_a A_{\text{Elec}}}{V_E V_R} + \frac{k_b}{V_R} + \frac{k_b}{V_E}\right) + \frac{k_a A_{\text{Elec}} k_b}{V_E} + k_b^2\right)c = \frac{S A_{\text{Elec}} \dot{Q}}{V_E V_R} \tag{3.2.3}$$

where we have dropped the subscript of $c_{\text{in}}(t)$ and examine simply $c(t)$ in mM, the concentration of $H_2O_2$ in the anolyte reservoir over time.

We make a final simplification of Equation (3.2.3) for the case that the flow rate, $\dot{Q}$, is very large. The full solution to Equation (3.2.3) and the justification of the high flow rate assumption are shown in Sections 3.A and 3.B. In the case of large $\dot{Q}$, the $\dot{Q}$ term cancels out and we obtain the first order differential equation in Equation (3.2.4).

$$\frac{dc}{dt} = \frac{S A_{\text{Elec}}}{V_E + V_R} - \frac{k_a A_{\text{Elec}}}{V_E + V_R}c - k_b c \tag{3.2.4}$$

Using the initial condition that $c(t) = 0$ at $t = 0$, we reach the final result in Equation (3.2.5).

$$c = \frac{S A_{\text{Elec}}}{k_a A + k_b(V_E + V_R)}\left(1 - e^{-\left(\frac{k_a A_{\text{Elec}}}{V_E + V_R} + k_b\right)t}\right) \tag{3.2.5}$$

As $t$ approaches $\infty$, we find the expected steady state concentration in Equation (3.2.6), which takes the form of the $H_2O_2$ generation term over a weighted sum of the $H_2O_2$ decomposition terms.

$$c_{\text{steady state}} = \frac{S A_{\text{Elec}}}{k_a A_{\text{Elec}} + k_b(V_E + V_R)} \tag{3.2.6}$$

We can also define an extent of reaction, $0 \leq \xi < 1$, such that $\xi c(t)$ is the fraction of the steady state concentration reached in the anolyte. Using this definition and solving for $t_\xi$, the time it takes to reach $\xi$ fraction of the steady state concentration, we arrive at Equation (3.2.7).

$$t_\xi = \frac{\ln(1-\xi)}{\left(\frac{k_a A_{\text{Elec}}}{V_E + V_R} + k_b\right)} \tag{3.2.7}$$

## 3.3. METHODS

### 3.3.1. MATERIALS

Experiments were performed using a flow cell constructed of laser-cut PMMA sheets with silicone and EPDM gaskets layered in between, compressed together with bolts. Titanium plates were used as current collectors, and the electrodes

were kept at a distance of 0.7 cm to the separator. The anode and cathode chamber dimensions were 3 cm wide by 4 cm tall by 0.7 cm deep ($V_E$ = 0.0084 L). The cathode was nickel fiber felt (12 $cm^2$, geometric) from Hebei Aegis Metal Materials Co., Ltd, 0.4 mm thickness, with 40 µm fiber diameter and 60% porosity. The anode was boron-doped diamond (2.5 cm×4 cm = 10 $cm^2$, geometric) from NeoCoat on a niobium substrate, with 5 µm thick, p-doped, 2500 ppm boron doping, polycrystalline coating. The separator used was the porous diaphragm, Zirfon Perl UTP 500 (Agfa) with a thickness of 500 µm. The electrolyte used was 1 M $Na_2CO_3$ (Merck-Sigma, ACS Reagent, ≥ 99.5%, powder or granules) plus 11 g $L^{-1}$ (approximately 90 mM) $Na_2SiO_3$ (Merck-Sigma, SKU 307815). Flow was maintained at 0.1 L $min^{-1}$ using a Longer BT100-3J peristaltic pump with DG15-24 two-channel pump head, with the anolyte and catholyte recirculated separately. The tubing for anolyte held a volume of 8.04 $cm^3$, which was negligible compared to the anolyte volume of $V_A$ = 0.4 L. The anolyte reservoir was magnetically stirred to ensure good mixing.

Because $S$, $k_a$, and $k_b$ are expected to vary based on temperature, pH, electrolyte composition, presence of a stabilizer, etc., these parameters were kept constant across all experiments. The anolyte pH was maintained between 13.25 and 13.10, just above the base electrolyte pH of 13.10, by manual monitoring and addition of aliquots of 5 M NaOH (Merck-Sigma, ACS Reagent, ≥ 97.0%) solution. The high NaOH concentration served to reduce the amount of anolyte volume change upon NaOH addition. The overall combination of reaction, sampling, NaOH addition, and any possible liquid flux through the porous separator resulted in overall volume changes of < 10% over 7 hours across all experiments. The temperature was controlled to be just under room temperature, at approximately 16 ± 1 °C, by immersing the anolyte reservoir in a cold water bath. The anolyte pH and temperature were measured using a Prominent PHEP-H 314 SE sensor and a Prominent Pt 100-SE sensor, respectively. Catholyte was recirculated for all experiments, with no maintenance of pH or temperature. Fixed current (galvanostatic operation) was supplied at 1.0, 2.0, or 3.0 A in two-electrode operation using an OWON SPE6103 power supply. Figure 3.3.1a shows a photo of the experimental setup and Figure 3.3.1b shows the typical curves for pH and temperature in the anolyte reservoir over time during an experiment with recirculating flows.

### 3.3.2. $H_2O_2$ Quantification

The $H_2O_2$ concentration was quantified using the potassium permanganate ($KMnO_4$) titration method as outlined by Gill et al. [56] In short, the method comprises of taking a sample of electrolyte (typically 2.5 mL) and immediately acidifying with equal volume of a 1:5 dilution of $H_2SO_4$ (Merck-Sigma, 95%-98%, ACS Reagent) in milli-Q water. Electrolyte samples from both anolyte and catholyte were taken from the reservoirs at regular intervals. For single-pass experiments, electrolyte was sampled directly from the reactor outflow. The titrant used was a 2 mM solution of $KMnO_4$, diluted ten-fold from stock solution (Merck-Sigma, 0.02 M, standardized against oxalate, Titripur). To start, three drops of 2 mM $KMnO_4$ solution were added to the magnetically stirred, acidified sample until the pink

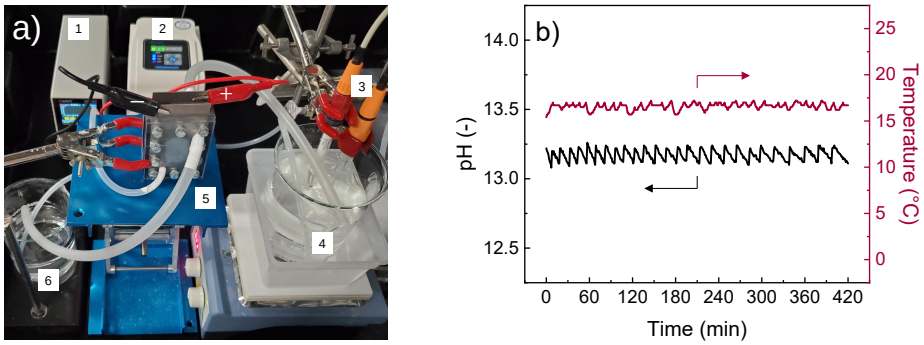


Figure 3.3.1: a) Photo of the experimental setup with 1) power supply 2) two-channel peristaltic pump 3) pH and temperature sensors 4) Anolyte reservoir with magnetic stirring and external container for cold water bath 5) electrochemical flow cell with cathode compartment near and anode compartment away 6) catholyte reservoir. b) Plot of the maintained pH and temperature of the anolyte reservoir for a typical experiment with recirculating flows. The vertical spikes in pH were the moments of NaOH solution addition, and are required less frequently as the pH of the catholyte slowly increases during the experiment.

color disappeared (starting the reaction). These three drops defined the limit of quantification for a 2.5 mL sample to be 0.3 mM. The titrant was further added drop-wise until a light-pink color remained in the sample, indicating the titration endpoint.

### 3.3.3. DETERMINATION OF GENERATION RATE, $S$

The majority of literature shows that for fresh electrolyte passed across the anode, the generation of $H_2O_2$ tends to be constant over time for a fixed operating potential. [21, 85] This observation could also be reasoned for an electrode that is very stable over time, such as boron-doped diamond. So for a corresponding fixed current density, this formation rate can be expressed as,

$$S = \frac{\dot{Q} c_{\text{single pass}}}{A_{\text{Elec}}} = \frac{j}{n\mathcal{F}} \text{FE}_{H_2O_2} \tag{3.3.1}$$

where $c_{\text{single pass}}$ is the $H_2O_2$ concentration achieved in electrolyte flown in single-pass over the anode, $j$ is the current density, n = 2 is the ratio of moles of electrons to moles of $H_2O_2$, $\mathcal{F}$ is Faraday's constant, and $\text{FE}_{H_2O_2}$ is the faradaic efficiency towards $H_2O_2$. The generation rate, $S$, for a single current density can be experimentally quantified by flowing electrolyte in single-pass at a high flow rate and measuring the outlet $H_2O_2$ concentration immediately. The high flow rate and quick measure-

ment ensure that the residence time for anodic oxidation and the time for bulk disproportionation are low enough to be negligible. Figure 3.3.2 shows the schematic of the flow setups of the experiments. The first expression in Equation (3.3.1) can be used to find a value for $S$ from the experiment, while the second can be used to calculate the faradaic efficiency.



### 3.3.4. Determination of Bulk Disproportionation Rate Constant, $k_b$

The experimental determination of the rate constant for bulk disproportionation, $k_b$, required first running the electrolyzer with recirculating flow in order to charge the anolyte with $H_2O_2$. After two hours of operation with pH and temperature maintained, the electrolyzer contents were drained into the reservoirs, and samples of anolyte were periodically taken for $H_2O_2$ quantification. This procedure was performed for three different current densities in order to compare concentration curves with different initial concentration values.

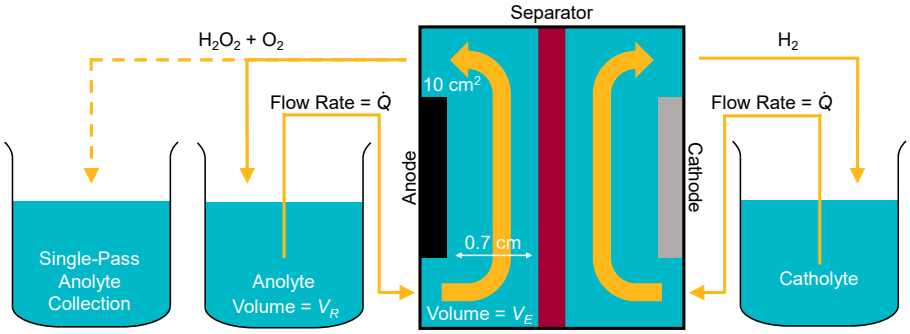


Figure 3.3.2: Diagram of the different flow configurations (not to scale). The solid arrow leaving the anode chamber and returning to the anolyte reservoir represents recirculating flow, while the dashed arrow leaving the anode chamber towards a separate collection vessel represents single-pass flow. For recirculating flow, anolyte is sampled from the reservoir. For single-pass flow, anolyte is sampled directly from the outlet of the anode chamber, not the collection vessel.

### 3.3.5. Numerical Fitting of Anodic Decomposition Rate Constant, $k_a$

Because the anodic oxidation of $H_2O_2$ is an electrochemical reaction, $k_a$ is expected to increase as the cell potential increases. However, due to its lower thermodynamic half cell potential of $E°$ = 0.67 V versus RHE compared to the generation of $H_2O_2$ at 1.76 V versus RHE, these two reactions are in direct competition. As

such, $k_a$ cannot be independently measured. Instead, after experimentally deriving values for $S$ and $k_b$ as described in Sections 3.3.3 and 3.3.4, the electrolyzer is run for seven hours with recirculating flow. Samples of electrolyte are taken for $H_2O_2$ quantification as described in Section 3.3.2. With the known values of $V_E$ and $V_R$, the data points of $c(t)$ for a given current density are fitted to Equation (3.2.5) in Python using the 'curvefit' function from the SciPy module. This function runs a non-linear least squares regression to find the best fit. Fitted parameters were given no constraints and only supplied with an initial guess to ease computation.



## 3.4. Results and Discussion

### 3.4.1. $H_2O_2$ Generation Values

The results of the single-pass flow experiments are shown in Figure 3.4.1a. Using the average concentrations at each of the three current densities, we use Equation (3.3.1) to calculate $S$ = 0.017, 0.037, and 0.054 mmol $min^{-1}$ $cm^{-2}$ for 100, 200, and 300 mA $cm^{-2}$, respectively. The calculated faradaic efficiencies at each of the three current densities were similar, with values of 54%, 59%, and 58% for 100, 200, and 300 mA $cm^{-2}$, respectively. These constant $H_2O_2$ generation rates and the calculated faradaic efficiencies are consistent with the literature report of boron-doped diamond materials by Mavrikis et al. using refreshed electrolyte. [85] At the same current densities in 1 M carbonate/bicarbonate electrolyte, they report $H_2O_2$ generation rates between 0.016 and 0.076 mmol $min^{-1}$ $cm^{-2}$ and faradaic efficiencies between 50% and 70% for a set of boron-doped diamond anodes.

### 3.4.2. $H_2O_2$ Loss via Bulk Disproportionation

The results of the experiments for $k_b$ quantification are shown in Figure 3.4.1b. Each of the curves represent a batch of anolyte that was charged with $H_2O_2$ for two hours at 100, 200, or 300 mA $cm^{-2}$ with separately recirculating flows. The power supply was then switched off, its contents drained, and the anolyte concentration was measured over time. Literature indicates that the disproportionation of $H_2O_2$ should be a first order decomposition reaction. [62] Examining the data, we see a constant slope on a semi-log plot for all three data sets, indicating a first order decomposition reaction with an average rate constant of $1.85 \times 10^{-3}$ $min^{-1}$. This value is consistent with the value for bulk disproportionation found by Li et al., who used an electrolyte of 2 M $KHCO_3$ at room temperature, and Lee et al., who studied $H_2O_2$ decomposition for a range of electrolytes including $Na_2CO_3$ with $Na_2SiO_3$ stabilizer. [62, 87]

### 3.4.3. Full System - Fitting Data to Find $k_a$

After deriving $S$ and $k_b$, we now perform seven hour experiments with separately recirculating electrolyte, a porous Zirfon separator, and with anolyte pH and temperature maintained. Figure 3.4.2 shows the accumulation of $H_2O_2$ over time in the system, along with the fit for Equation (3.2.5). The fitted values for $k_a$ are 0.136, 0.304,

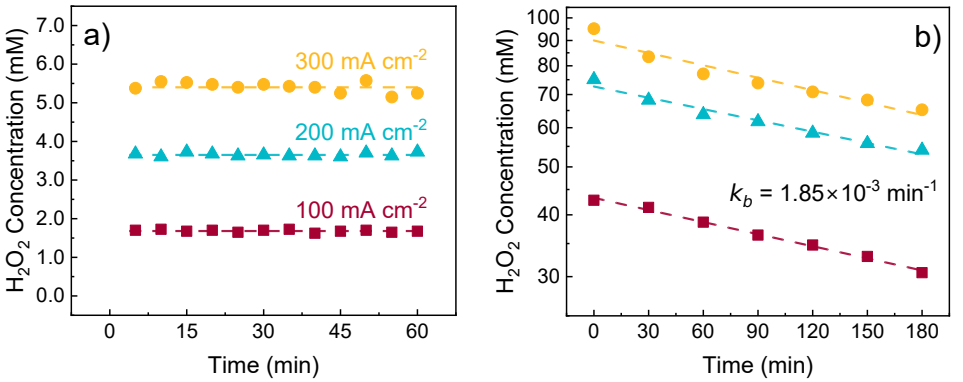


Figure 3.4.1: a) The constant generation of $H_2O_2$ under single-pass flow for a given current density. The dashed lines indicate the average measured concentrations over one hour of 1.68, 3.65, and 5.40 mM for 100, 200, and 300 mA $cm^{-2}$, respectively. These average concentrations are used to calculate $S$ = 0.017, 0.037, and 0.054 mmol $min^{-1}$ $cm^{-2}$, in order of increasing current density. b) Comparison in semi-log scale of the homogeneous decomposition of $H_2O_2$ in anolyte from different starting concentrations without applied current. These starting concentrations were achieved by operating the electrolyzer with recirculating electrolyte flow for two hours at different current densities. Dashed lines are linear regressions of the data sets. These data sets share a constant slope, indicating a first order bulk disproportionation reaction with an average rate constant of $k_b = 1.85\times10^{-3}$ $min^{-1}$.

and 0.349 cm $min^{-1}$ for 100, 200, and 300 mA $cm^{-2}$, respectively. The modified anodic decomposition term as it appears in Equation (3.2.4), $(k_a A_{Elec})/(V_E + V_R)$, was calculated to be $3.40\times10^{-3}$, $7.59\times10^{-3}$, and $8.73\times10^{-3}$ $min^{-1}$, in order of increasing current density. These values are all greater than $k_b = 1.85\times10^{-3}$ $min^{-1}$, indicating that the anodic oxidation of $H_2O_2$ in the anolyte was the dominant loss mechanism in our system. The fit appears to match the experimental results well, though there is a slight underprediction of the concentration at $t < 240$ min and a slight overprediction of the steady state concentration at $t > 360$ min. This likely originates from our definition of the constant generation of $H_2O_2$. In the case of a competing surface reaction, $S$ would no longer be constant, but be expected to decrease over time as $c(t)$ increased over time, due to the increased rate of anodic oxidation. Nevertheless, the fit is good and displays the expected trend of increasing $k_a$ with increasing current density.

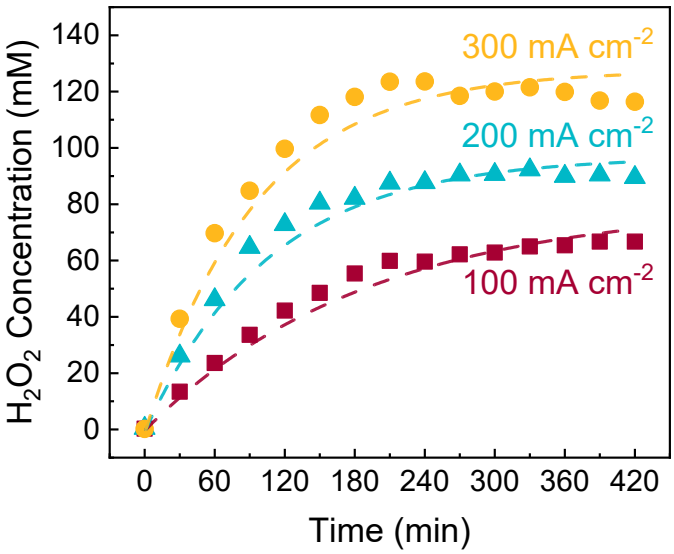


Figure 3.4.2: Seven-hour experiments for the anodic production of $H_2O_2$ with recirculating anolyte. The dashed lines show Equation (3.2.5) using fitted $k_a$ values of 0.136, 0.304, and 0.349 cm min$^{-1}$ for 100, 200, and 300 mA cm$^{-2}$, respectively.



### 3.4.4. Exclusion of Crossover Effects

It was observed that the $H_2O_2$ concentration in the catholyte was always at or below the limit of quantification (0.3 mM as mentioned in Section 3.3.2). This indicated that either the decomposition of $H_2O_2$ in the catholyte far outpaced the diffusive flux through the Zirfon separator, or that the diffusive flux itself was negligible. At pH greater than the pKa of $H_2O_2$ (11.7), the $H_2O_2$ exists primarily in its deprotonated form as $HO_2^-$. This anion experiences a force of electric migration towards the anode, which is in the opposite direction of the diffusive flux. We therefore reason, as we operate at pH > 13, that nearly all of the anodically produced $H_2O_2$ is retained in the anolyte. To confirm this, we modify Equation (3.2.1) to add a term to account for $H_2O_2$ crossover, $-k_c A_{Sep} c_{out}(t)$, where $A_{Sep}$ is the separator surface area. The $k_c$ term can be calculated by analogy to Fick's law for diffusion across the separator, assuming a concentration of zero on the cathode side, as per Equation (3.4.1),

$$k_c = \frac{D_{Eff}}{L_{Sep}} \tag{3.4.1}$$

where $k_c$ in cm min$^{-1}$ is the rate constant for crossover, $D_{Eff}$ is the effective diffusion coefficient, and $L_{Sep}$ is the thickness of the separator. Using the values of our setup ($A_{Sep}$ = 12 cm$^2$ and $L_{Sep}$ = 0.05 cm) and assuming a typical liquid diffusion coefficient at ambient temperature of $D_{Eff} = 1\times10^{-5}$ cm$^2$ s$^{-1}$, we find $k_c$ = $2.0\times10^{-4}$ cm min$^{-1}$. The modified crossover term as it would appear in Equa-

tion (3.2.4), $(k_c A_{Sep})/(V_E + V_R)$, was calculated to be $3.60 \times 10^{-4}$ min$^{-1}$. Comparing this value to the anodic decomposition terms that we found in Section 3.4.3 (all $\geq 3.40 \times 10^{-3}$ min$^{-1}$), we see that any effect of crossover is negligible in comparison to the anodic oxidation in the anode chamber. The modified crossover term is also negligible in comparison to the bulk decomposition rate constant of $1.85 \times 10^{-3}$ min$^{-1}$.



### 3.4.5. Extension to Literature Data

One of the strengths of the outlined analytical model is that knowledge of the precise details of the system are not required. Neither the specific reaction mechanism for $H_2O_2$ generation, the particular electrolyte composition, nor the electrolyzer geometry have to be taken into consideration. The only relevant parameters are the physical dimensions ($A_{Elec}$, $V_E$, and $V_R$), the overall generation rate ($S$), and the rate constants ($k_a$ and $k_b$). As such, the model remains versatile. We demonstrate this versatility by examining two sources from literature, Pangotra et al. [34] and Li et al. [87], and use their data to calculate rate constants as per their experimental setups.

The setup of Pangotra et al. uses a 10 cm$^2$ anode and an electrolyte flow rate of 0.1 L min$^{-1}$, and is very similar to our own. The main difference is that they use Nafion 117 as a separator and keep their anolyte in an ice bath to maintain the temperature. Using their data, we found a $k_b$ value of $5.70 \times 10^{-4}$ min$^{-1}$ for 2 M $K_2CO_3$ with 90 mM $Na_2SiO_3$ electrolyte. This value is about three times lower than for our system, which is consistent with a lowered reaction rate due to lower temperatures. We fitted their data for both $S$ and $k_a$ at the same current densities as we use, and the fit is shown in Figure 3.4.3a. The fitted curve shows excellent agreement, likely due to the additional free parameter available for fitting, $S$. Table 3.4.1 lists the computed values for all of the experimental data sets analyzed. The values of $S$ from Pangotra et al. are comparable to ours, but the $k_a$ values are much higher, particularly at 300 mA cm$^{-2}$. This leads to their overall lower steady state concentrations and their observed optimal current density of 200 mA cm$^{-2}$.

The setup used by Li et al. was not a flow setup but rather a separated batch reactor system. The anolyte was magnetically stirred to ensure mixing. Li et al. operate their system potentiostatically, but observed a relatively constant current at each potential, allowing our analysis to continue. While they do not maintain pH or temperature, they operate at low currents of $< 35$ mA and observe a very small pH change from 8.31 to 8.68. We therefore assume that the temperature and pH have not changed significantly over the course of the experiment, such that the model can still be applied. The analytical model can be reformulated by simply setting $V_R$ and $\dot{Q}$ equal to zero, which causes Equation (3.2.2) to cancel out entirely. The resulting mole balance across the electrolyzer takes the following form.

$$V_E \frac{dc_{out}}{dt} = S A_{Elec} - k_a A_{Elec} c_{out} - k_b V_E c_{out} \tag{3.4.2}$$

The solution to Equation (3.4.2), replacing $c_{out}$ with $c$, is shown in Equa-

tion (3.4.3),

$$c = \frac{SA}{k_a A_{\text{Elec}} + k_b V_E}\left(1 - e^{-\left(\frac{k_a A_{\text{Elec}}}{V_E} + k_b\right)t}\right) \tag{3.4.3}$$

where $V_E$ = 0.06 L is the anolyte volume. Equation (3.4.3) takes the same overall form as Equation (3.2.5), but setting $V_R$ equal to 0. This is a result of all reactions taking place in the same batch reactor, without a separate reservoir. Li et al. [87] arrive at a similar expression to Equation (3.2.5) and Equation (3.4.3) and fit it successfully to their data. However, they combine their $k_a$ and $k_b$ terms into a single parameter and neglect the solution volume and electrode surface area. Our more versatile analytical model based on mole balances successfully accounts for these differences, and the fit of Equation (3.4.3) to their data is shown in Figure 3.4.3b. Our fit matches well to the experimental data obtained by Li et al. However, the data sets do not continue until a very clear steady state, so we cannot comment on any underprediction or overprediction of the model with respect to time. Li et al. performed a similar experiment to quantify the contribution of bulk disproportionation as we did and found $k_b = 1.83 \times 10^{-3}$ min$^{-1}$. [87] This value is very close to the value for our system, despite using a different electrolyte of 2 M $KHCO_3$. The values of $S$ (calculated using data from Li et al.) are significantly lower than our values due to the lower total current of their experiments with a 0.5 cm$^2$ anode, but follow the predicted trend of increasing with increasing current density (see Table 3.4.1). However, the $k_a$ values (fitted) are quite large, and are comparable to those of Pangotra et al., who operate at much higher current densities. These large anodic decomposition rate constant values may also have led to the lower concentrations seen in the experiments of Li et al. This result highlights the drawback of running such a system in batch reactor, as there is a large opportunity for any produced $H_2O_2$ to oxidize further. In contrast, a flow cell system has a lower residence time of $H_2O_2$ in the electrolyzer, thereby reducing the chance for anodic oxidation of $H_2O_2$.

### 3.4.6. Model Validation and Implications for Scaled-Up Operation

The scaled-up electrochemical process to produce $H_2O_2$ with high flow rates faces the obstacle of low single-pass conversion. A low $H_2O_2$ concentration makes later separation and purification more difficult, and low flow rates result in overall low product yield, thus necessitating anolyte recirculation to charge it with higher concentrations of $H_2O_2$. The objective of the process design should then be to maximize $H_2O_2$ concentration in the anolyte stream in the minimum required time. While $S$, $k_a$, and $k_b$ are dependent on the electrode-electrolyte system chosen, $A_{\text{Elec}}$, $V_E$, $V_R$, and $\dot{Q}$ can all be easily changed as desired to fit the requirements of a separation system or target production rate.

To validate our model's ability to predict the change in $c(t)$ with varying $V_E$ or $V_R$, we perform experiments at 200 mA cm$^{-2}$ and overlay the predicted curves using fixed parameter values of $S$, $k_a$, and $k_b$ for different $V_E$ and $V_R$. The results of these experiments are shown in Figure 3.4.4. The model slightly underpredicts

Table 3.4.1: Summary of parameter values from fitted data. Entries marked "(fit)" were fitted using Equation (3.2.5) or Equation (3.4.3), while the others were derived from available data. $E_{Cell}$ indicates the full cell potential.

| **This Work** | $A_{Elec}$ (cm$^2$) | $V_R$ (L) | $V_E$ (L) | $\dot{Q}$ (L min$^{-1}$) |
|---|---|---|---|---|
| | 10 | 0.3916 | 0.0084 | 0.1 |
| | $S$ (mmol min$^{-1}$ cm$^{-2}$) | | $k_a$ (fit) (cm min$^{-1}$) | $k_b$ (min$^{-1}$) |
| 100 mA cm$^{-2}$ ($E_{Cell}$ ~ 5.5 V) | 0.017 | | 0.136 | $1.85\times10^{-3}$ |
| 200 mA cm$^{-2}$ ($E_{Cell}$ ~ 7.5 V) | 0.037 | | 0.304 | $1.85\times10^{-3}$ |
| 300 mA cm$^{-2}$ ($E_{Cell}$ ~ 9.1 V) | 0.054 | | 0.349 | $1.85\times10^{-3}$ |
| **Pangotra et al. [34]** | $A_{Elec}$ (cm$^2$) | $V_R$ (L) | $V_E$ (L) | $\dot{Q}$ (L min$^{-1}$) |
| | 10 | 0.191024 | 0.008976 | 0.1 |
| | $S$ (fit) (mmol min$^{-1}$ cm$^{-2}$) | | $k_a$ (fit) (cm min$^{-1}$) | $k_b$ (min$^{-1}$) |
| 100 mA cm$^{-2}$ ($E_{Cell}$ ~ 4.4 V) | 0.016 | | 0.423 | $5.7\times10^{-4}$ |
| 200 mA cm$^{-2}$ ($E_{Cell}$ ~ 5.9 V) | 0.036 | | 0.641 | $5.7\times10^{-4}$ |
| 300 mA cm$^{-2}$ ($E_{Cell}$ ~ 6.7 V) | 0.069 | | 1.830 | $5.7\times10^{-4}$ |
| **Li et al. [87]** | $A_{Elec}$ (cm$^2$) | $V_R$ (L) | $V_E$ (L) | $\dot{Q}$ (L min$^{-1}$) |
| | 0.5 | 0 | 0.06 | 0 |
| | $S$ (mmol min$^{-1}$ cm$^{-2}$) | | $k_a$ (fit) (cm min$^{-1}$) | $k_b$ (min$^{-1}$) |
| 2.3 V vs RHE (~25 mA cm$^{-2}$) | $6.37\times10^{-3}$ | | 0.456 | $1.83\times10^{-3}$ |
| 2.5 V vs RHE (~42 mA cm$^{-2}$) | $8.88\times10^{-3}$ | | 0.707 | $1.83\times10^{-3}$ |
| 2.7 V vs RHE (~69 mA cm$^{-2}$) | 0.013 | | 1.113 | $1.83\times10^{-3}$ |

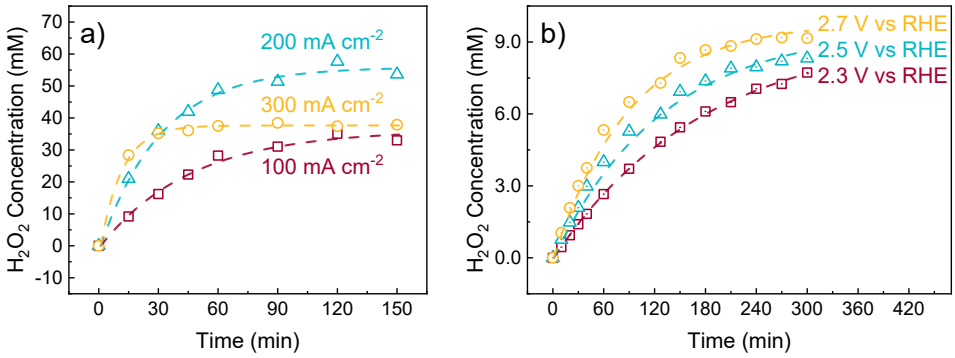


Figure 3.4.3: Fits to data from literature sources, with open symbols to indicate data points not from our work. See Table 3.4.1 for a summary of parameter values. a) Dashed lines showing the fit of Equation (3.2.5) to the data of Pangotra et al. [34] Both $S$ and $k_a$ were fitted to this data using $k_b$ from their data. b) Dashed lines showing the fit of Equation (3.4.3) to the data of Li et al. [87] Only $k_a$ was fitted to this data using $S$ and $k_b$ from their data.

the effect of increasing the anolyte reservoir volume, and largely misses the effect of changing the electrolyzer volume. The data gathered with $V_E$ = 0.0036 L was obtained by assembling the electrolyzer using a thinner PMMA plate for the anode chamber, altering the cell geometry and bringing the anode closer to the separator. Equation (3.2.5) predicts that changing $V_E$ while keeping $V_A$ constant should have no change on the accumulated $H_2O_2$ concentration. However, it appears that modeling the anodic oxidation of $H_2O_2$ as a surface reaction using a homogeneous concentration value across the electrolyzer chamber was insufficient to model the system. It is likely that the effect of cell geometry is too significant to be captured by a first order expression using a homogeneous concentration. Future refinement of this model should instead use a mass transfer expression based on electrolyzer geometry to find a surface $H_2O_2$ concentration value and examine different electrolyzer geometries and current densities to validate the expression.

Because the effect of changing $V_R$ was predicted relatively well, we extend the predictions to other values of $V_R$, using a base case with $V_E$ = 0.0084 L and $V_R$ = 0.3916 L as per our experimental setup. These predictions are shown in Figure 3.4.5a. As expected by examination of Equation (3.2.6), decreasing $V_R$ leads to higher steady state concentrations. Figure 3.4.5a also shows that decreasing $V_R$ leads to higher concentrations of $H_2O_2$ earlier in time as the anolyte is charged with $H_2O_2$. However, due to the large change in anolyte volume with $V_R$, the trend for the total number of moles is reversed. Figure 3.4.5b shows the predicted accumulation of $H_2O_2$ in moles, where a low $V_R$ achieves a correspondingly low amount of $H_2O_2$, reversing the trend seen in Figure 3.4.5a. Therefore, the target $H_2O_2$ production

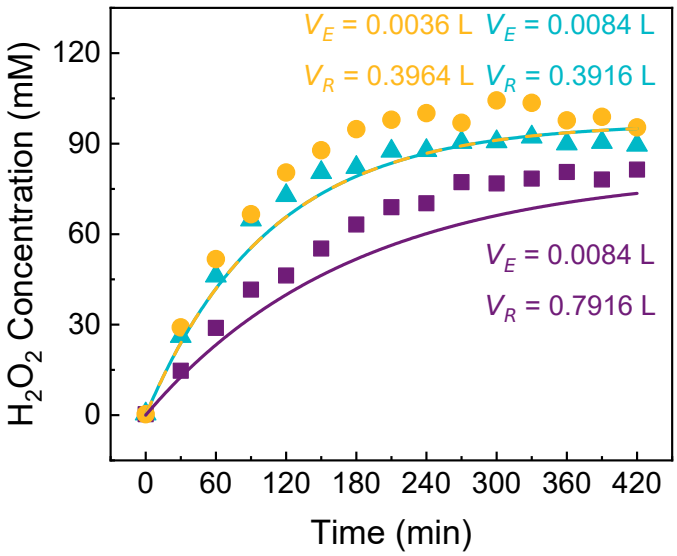


Figure 3.4.4: Experimental validation of the model for different $V_E$ and $V_R$ at 200 mA $cm^{-2}$. The lines show the predicted concentration curves for the given parameters. The predicted concentrations for the base case and the reduced $V_E$ case overlap completely because the total anolyte volume, $V_A$, was not changed. The prediction for changing $V_R$ underpredicts the experiment, and the prediction for changing $V_E$ does not match.

rate must be considered in tandem with the system geometry to find the optimal design parameters and recirculation time. This could be accomplished by setting a desired extent of reaction, $\xi$, or a desired reaction time, $t_\xi$, and then optimizing for the number of moles of $H_2O_2$.

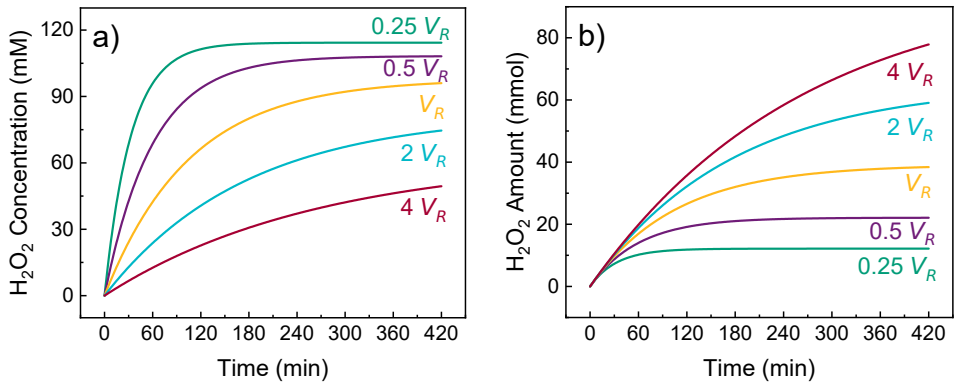


Figure 3.4.5: Simulated results using Equation (3.2.5) at 200 mA cm$^{-2}$ with changing reservoir volume, with $V_R$ = 0.3916 L and $V_E$ = 0.0084 L. a) The concentration of $H_2O_2$ reaches a higher steady state value more quickly with decreasing $V_R$. As $V_R$ approaches 0, the predicted curve approaches the case of a batch reactor. b) Simulated results for the amount of $H_2O_2$ in mmol at 200 mA cm$^{-2}$ with changing reservoir volume, $V_R$. Because the total electrolyte volume decreases strongly with decreasing $V_R$, the total number of moles produced also decreases.

## 3.5. CONCLUSIONS

The large-scale electrochemical production of $H_2O_2$ is hampered by low single-pass conversion, and thus requires electrolyte recirculation to charge the anolyte with enough $H_2O_2$ for further separation. Our work provides an analytical solution for how the concentration develops over time and a methodology to find individual reaction terms for a given system geometry. With simple experimentation, the individual rate constants for anodic generation and bulk disproportionation of $H_2O_2$ can be quantified. A rate constant for anodic oxidation can then be numerically fitted, but this value is best taken as an estimation of the anodic oxidation for a particular electrolyzer geometry. We found for our system, as well as two others in literature, that the $H_2O_2$ decomposition due to anodic oxidation was always greater than the decomposition due to bulk disproportionation. As a result of describing anodic oxidation using a homogeneous concentration across the electrolyzer chamber, our analytical model predicted that changing the volume of electrolyte in the anode

chamber would have no effect on the achieved concentration of $H_2O_2$. However, this description was found to be unsuitable for a differing electrolyzer geometry, and the model should be refined with a more generalized expression that accounts for electrolyzer geometry and mass transfer in order to extend the model using surface concentrations. We recommend that the anolyte reservoir volume, $V_R$, be selected to meet the target production rate at a desired reaction time, but further work can be done to find the optimal balance between these parameters and the overall cost of the scaled-up system.

# 3.A. APPENDIX - LOW FLOW RATE SOLUTION TO ANALYTICAL MODEL

Starting with Equation (3.2.3), we make the following substitutions:

$$\frac{d^2c}{dt^2} + \alpha\frac{dc}{dt} + \beta c = \gamma \tag{3.A.1}$$

$$\alpha = \frac{\dot{Q}}{V_E} + \frac{\dot{Q}}{V_R} + \frac{k_a A_{\text{Elec}}}{V_E} + 2k_b$$

$$\beta = \dot{Q}\left(\frac{k_a A_{\text{Elec}}}{V_E V_R} + \frac{k_b}{V_R} + \frac{k_b}{V_E}\right) + \frac{k_a A_{\text{Elec}} k_b}{V_E} + k_b^2$$

$$\gamma = \frac{S A_{\text{Elec}} \dot{Q}}{V_E V_R}$$

This leads to the general solution,

$$c = C_1 e^{-\lambda_1 t} + C_2 e^{-\lambda_2 t} + \frac{\gamma}{\beta} \tag{3.A.2}$$

where $C_1$ and $C_2$ are constants, and

$$\lambda_1 = \frac{\alpha - \sqrt{\alpha^2 - 4\beta}}{2} \quad ; \quad \lambda_2 = \frac{\alpha + \sqrt{\alpha^2 - 4\beta}}{2}$$

Using the initial conditions that $c(t) = 0$ at $t = 0$ and $dc(t)/dt = (SA_{\text{Elec}})/V_R$ at $t = 0$, we arrive at the complete solution in Equation (3.A.3).

$$c = \left(\frac{S A_{\text{Elec}}\beta - \gamma\lambda_2 V_R}{\beta V_R (\lambda_2 - \lambda_1)}\right) e^{-\lambda_1 t} - \left(\frac{S A_{\text{Elec}}\beta - \gamma\lambda_1 V_R}{\beta V_R (\lambda_2 - \lambda_1)}\right) e^{-\lambda_2 t} + \frac{\gamma}{\beta} \tag{3.A.3}$$

At $t$ approaches $\infty$, the steady state concentration reached can be expressed as Equation (3.A.4),

$$c_{\text{steady state}} = \frac{\gamma}{\beta} = \frac{S A_{\text{Elec}}}{k_a A_{\text{Elec}} + k_b (V_E + V_R) + \frac{k_a A_{\text{Elec}} k_b V_R}{\dot{Q}} + \frac{k_b^2 V_E V_R}{\dot{Q}}} \tag{3.A.4}$$

which simplifies to Equation (3.2.6) for large $\dot{Q}$.

## 3.B. Appendix - High Flow Rate Justification

In Section 3.2.4, we use a simplification of Equation (3.2.3) in the case of large $\dot{Q}$. Here, we fix the values of $S$, $k_a$, $k_b$, $A_{\text{Elec}}$, $V_E$, and $V_R$ using the values for our setup at 200 mA cm$^{-2}$, and vary $\dot{Q}$ in Equation (3.A.3) to confirm that our assumption is valid. Using a base case of $\dot{Q}$ = 0.1 L min$^{-1}$, as used in our experiments, we show the predicted effect of changing $\dot{Q}$ using Equation (3.A.3) in Figure 3.B.1. The curves for the fastest three flow rates (2 $\dot{Q}$, $\dot{Q}$, and 0.5 $\dot{Q}$) overlap, indicating that our flow rate of $\dot{Q}$ = 0.1 L min$^{-1}$ was sufficiently fast to use Equation (3.2.5) in our analysis.

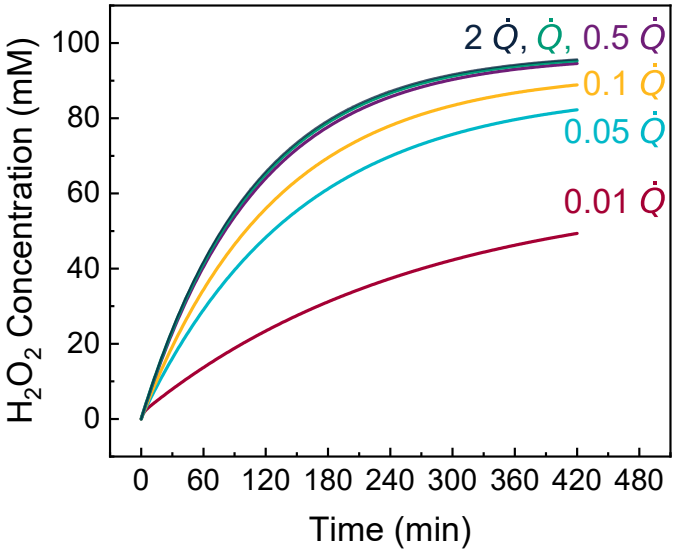


Figure 3.B.1: Simulated results for changing flow rate, $\dot{Q}$, where the highest three flow rates (corresponding to 0.2, 0.1, and 0.05 L min$^{-1}$) overlap, indicating the validity of the high flow rate assumption at 0.1 L min$^{-1}$.

# 4

# PROCESS DESIGN TO SEPARATE AND SELL HYDROGEN PEROXIDE


## ABSTRACT

The recent interest in the production of green hydrogen through water electrolysis is hampered by its high cost when compared to steam methane reforming. To overcome this disadvantage, some studies explore replacing anodic oxygen production with hydrogen peroxide, which has a higher value. Existing electrocatalysis research primarily focuses on hydrogen peroxide synthesis, neglecting process design and separation. Additionally, hydrogen peroxide's thermodynamic instability in alkaline conditions and the existence of other ions make the separation difficult. This chapter proposes a novel concept for the paired water electrolysis process that can be used to improve green hydrogen production economics through valuable chemical co-productions. Valorizing hydrogen peroxide to sodium percarbonate as the final product was chosen to address hydrogen peroxide separation challenges. An electrolyzer stack of 2 MW was chosen, incorporating a recirculating structure, and a boron-doped diamond anode to enhance the hydrogen peroxide production as the base case. According to the techno-economic analysis, for a 2 MW electrolyzer stack, capital expenditure was calculated as 64.5 M€, operational expenses as 21.6 M€, and revenue was calculated as 2.5 M€, resulting in a negative cash flow of -19.1 M€. Results revealed that the process can be profitable (breakeven point) at a capacity of approximately 308 electrolyzer stacks, which is 616 MW in capacity. A sensitivity analysis was conducted to determine how cost drivers including electricity price, anode price, faradaic efficiency, price of the products and tax subsidy



The work in this chapter is based on M. Mohajeri, S. Shanbhag, E. Trasias, F. Mousazadeh, W. de Jong and S. A. Phadke. 'Valorization of Hydrogen Peroxide for Sodium Percarbonate and Hydrogen Coproduction via Alkaline Water Electrolysis: Conceptual Process Design and Techno-Economic Evaluation'. In: *Industrial & Engineering Chemistry Research* 64.5 (2025), pp. 2801–2815. DOI: 10.1021/acs.iecr.4c03408 [88]

affect the breakeven point. A breakeven point of 60 electrolyzer stacks (120 MW) was found with a 100% increase in the sodium percarbonate sale price. In comparison, a theoretical 100% faradaic efficiency in the anode material would result in a breakeven point of 38 electrolyzer stacks (76 MW). Even a more realistic 75% faradaic efficiency leads to a breakeven plant size of 75 stacks (150 MW). Further, multiple two-parameter sensitivity analyses were conducted to assess the relations between faradaic efficiency, sodium percarbonate sale price and anode material price. For instance, if sodium percarbonate price increases by 100% and faradaic efficiency increases to 75%, the breakeven capacity drops down to 13 stacks (26 MW). Despite facing economic challenges for the proposed process design based on available technologies, the techno-economic analysis highlights key targets for future works. It also provides valuable insights into the economic feasibility of simultaneously producing hydrogen and sodium percarbonate through water electrolysis, indicating promising potential for the future.



## 4.1. INTRODUCTION

The issues of climate change related to greenhouse gas emissions have brought hydrogen ($H_2$) sharply into focus as a critical solution for the energy transition. Additionally, $H_2$ plays a significant role in the industry as a feedstock in various industrial processes, including ammonia, methanol, and steel production. Hydrogen is also a clean fuel that can be used for heating, thus enhancing its importance in fostering sustainability across a variety of sectors. Essentially, the significance of $H_2$, and in particular green hydrogen, lies in its capability to assist in the transition toward cleaner energy systems, as well as revolutionize industrial processes, contributing to global energy security and environmental sustainability. [89–93]

The steam methane reforming process remains the predominant method of producing $H_2$ worldwide (approximately 95%). [94] In recent years, there has been a growing emphasis on producing green $H_2$ through electrolysis using renewable energy sources, such as wind and solar power. Electrolysis technologies have gained considerable attention, particularly proton exchange membranes (PEM) and alkaline electrolysis, because of their potential to produce $H_2$ without carbon emissions. However, the process economics are still not favorable, despite the promise of this approach. The price range of $H_2$ obtained by water electrolysis (2.75-7.5 € $kg^{-1}$) is still not competitive with the price range of $H_2$ obtained via steam methane reforming (0.5-1.5 € $kg^{-1}$). [95–99]

The relatively low market value of the co-produced oxygen (32 € $tonne^{-1}$) [97] in water electrolysis is one of the economic disadvantages of the process. Recent studies have suggested that $O_2$ production can be substituted for valuable chemical co-production in water electrolysis to lower the $H_2$ price. Studies have shown that anodic production of hydrogen peroxide ($H_2O_2$) is a viable co-product of water electrolysis. [21, 97, 100, 101] Despite extensive literature coverage [102–106] of cathodic $H_2O_2$ production via 2 $e^-$ oxygen reduction reaction (2 $e^-$ ORR), anodic $H_2O_2$ production through 2 $e^-$ water oxidation reaction (2 $e^-$ WOR) is less common due to the thermodynamic unfavorability of the pathway (due to the competing co-

production of $O_2$). The 2 $e^-$ WOR technique is the focus of the current study since it represents a coveted electrochemical reaction pathway that can produce the valuable co-product $H_2O_2$ while still producing green hydrogen, making it extremely desirable. [16, 107]

Mavrikis et al. compiled a review of the proposed reaction mechanisms of 2 $e^-$ WOR, which are critical for the fabrication of electrocatalysts and the assembly of electrochemical reactors. Furthermore, different electrode materials and electrolytes were examined in their investigation. [16] Recent developments in $H_2O_2$ production by water oxidation, including fundamentals, materials, strategies for increasing efficiency, etc. were reviewed by Xue et al. They discussed the challenges and future works for $H_2O_2$ production by water oxidation, including material stability, and industrial-scale analysis such as techno-economic evaluation. [108] Anantharaj et al. identified the strategies employed in the design of catalysts for both 2 $e^-$ ORR and 2 $e^-$ WOR and proposed a few simple principles that have enabled the prediction of other prospective elements within the periodic table that can also form $H_2O_2$ selective catalysts. [109] According to Perry et al., electrochemical $H_2O_2$ electrosynthesis technologies have the potential to challenge the conventional anthraquinone process to produce $H_2O_2$, but further progress is required before the electrochemical route will be able to compete. Based on examining the advances made in the fields of materials and reactor design, they concluded that further developments in materials are crucial for improving stability and production rates as well as reducing operating costs. [110]

Although novel 2 $e^-$ WOR electrocatalysts have shown significant promise at low electrical currents, their electrocatalytic capabilities decrease at larger current densities. Mavrikis et al. developed modulated boron-doped diamond (BDD) films which achieved an impressive 87% faradaic efficiency to $H_2O_2$ ($FE_{H_2O_2}$) and produced 76.4 µmol $H_2O_2$ $min^{-1}$ $cm^{-2}$ while maintaining stable electrochemical performance for 10 h at 200 mA $cm^{-2}$. They also concluded that BDD is a viable candidate for the implementation of 2 $e^-$ WOR on a large scale. [24, 85] In another study, the electrochemical synthesis of $H_2O_2$ using BDD electrodes was reviewed by Espinoza-Montero et al. BDD electrodes were found to be promising materials for anodic $H_2O_2$ formation with their high $FE_{H_2O_2}$ and $H_2O_2$ production rate. However, the high cost of BDD electrodes may limit their application at an industrial scale. [23] Using BDD as the anode, Pangotra et al. examined the effects of different parameters on the electrolyzer performance, including flow configuration, flow rate, and type of electrolyte. They achieved $FE_{H_2O_2}$ of up to 78% and a production rate of 79 µmol $H_2O_2$ $min^{-1}$ $cm^{-2}$ as well as current densities of up to 700 mA $cm^{-2}$ over a sustained period of 28 h. [34]

It has also been demonstrated that metal oxides and carbon-based electrodes can produce $H_2O_2$. Despite their impressive selectivity to $H_2O_2$, this study did not consider these materials because they have significantly low current density and short lifetimes, making their large-scale implementation questionable. [24, 111, 112]

$H_2O_2$ electrosynthesis relies heavily on an efficient product purification strategy, which has not yet been reported. Previous research has predominantly centered on the synthesis of $H_2O_2$, with no reported studies focusing on its separation. This

omission is attributed to hydrogen peroxide's thermodynamic instability when subjected to alkaline conditions. [113] As a result, the separation process has been overlooked in favor of addressing challenges related to its synthesis, with even other techno-economic analyses treating the separation system as a black box. [97, 114] To the best of our knowledge and investigation, $H_2O_2$ separation from the electrolyte solution is extremely difficult. Qi et al. also proposed valorizing $H_2O_2$ into another valuable chemical due to the same separation problem. [113]

Since $H_2O_2$ and sodium carbonate (electrolyte) already exist in the process, as an alternative product, $H_2O_2$ can be valorized to produce sodium percarbonate (SPC). Sodium percarbonate ($Na_2CO_3 \cdot 1.5\,H_2O_2$) is usually called solid $H_2O_2$ and is dissolved in water to produce $H_2O_2$. It has chemical properties similar to $H_2O_2$, is used as a bleaching agent in detergents, and is more efficient in several aspects. SPC can function over a wider pH range and offers a more economical alternative to $H_2O_2$ due to its solid form which makes it easier for transportation and storage. [115–118] Furthermore, its market capacity in 2024 is estimated at 1.54 B€ and is projected to grow at 8.3% yearly. [119]

Although many studies have been conducted concerning the development of novel electrode materials, the evaluation of different types of electrolytes, the examination of reaction mechanisms, etc., the process design and techno-economic evaluation of large-scale industrial plants remain largely unexplored. This study presents a novel process design to produce $H_2O_2$ through water electrolysis and valorizing it into SPC as the final product, along with a detailed technoeconomic analysis. Ultimately, a sensitivity analysis was conducted to assess how different parameters affect the economics of the process, including product prices, electrode prices, and $FE_{H_2O_2}$.

## 4.2. Process Design

### 4.2.1. Co-production of $H_2O_2$ and $H_2$ in the electrolyzer

Figure 4.2.1 shows the proposed process design based on the electrochemical water oxidation reaction to $H_2O_2$ ($2\,e^-$ WOR). The first part of the process involves the production of $H_2O_2$ through the electrolysis of water. Sodium carbonate ($Na_2CO_3$) is used as the electrolyte salt as it has been shown to improve the faradaic efficiency toward the anodic $H_2O_2$ product. [33] Sodium silicate is also added (in minor quantities) to improve the stability of the formed $H_2O_2$ in the process. Additionally, sodium hydroxide (NaOH) is periodically added to the electrolyzer to maintain the pH environment to promote $H_2O_2$ formation. The electrolyzer is maintained at ambient temperature with the help of cooling water. When a potential difference is applied across the cell, $H_2$ and hydroxide ions are formed at the cathode via the water reduction reaction. The hydroxide ions migrate toward the anode and are oxidized to produce $H_2O_2$ and $O_2$ at the anode. In addition to the significant amount of $O_2$ that is produced directly at the anode, there is also considerable $O_2$ produced through the decomposition of $H_2O_2$ at the anode surface and in the bulk electrolyte. The reactions at the anode are presented in Equations (4.2.1) – (4.2.3) and the reaction at the cathode is presented in Equation (4.2.4).

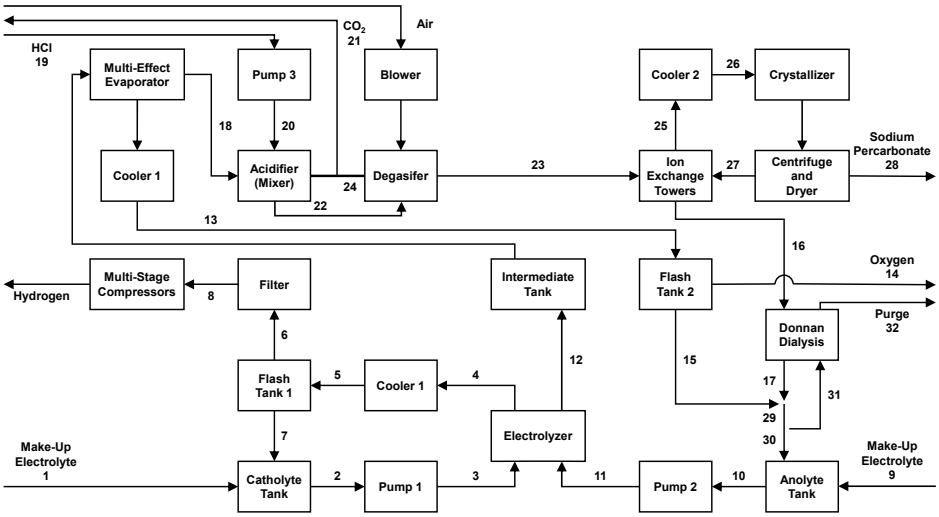


Figure 4.2.1: Process flow diagram of the proposed system. The catholyte recycles after a simple gas separation whereas the anolyte goes through a more complex chemical separation to crystallize out SPC before recycling. The streams are numbered and the overall inlet and outlet streams have their contents labeled.

$$2\,OH^- \rightarrow H_2O_2 + 2\,e^- \qquad E° = 1.76\ \text{V versus RHE} \qquad (4.2.1)$$

$$H_2O_2 + 2\,OH^- \rightarrow 2\,H_2O + O_2 + 2\,e^- \qquad E° = 0.67\ \text{V versus RHE} \qquad (4.2.2)$$

$$4\,OH^- \rightarrow 2\,H_2O + O_2 + 4\,e^- \qquad E° = 1.23\ \text{V versus RHE} \qquad (4.2.3)$$

$$2\,H_2O + 2\,e^- \rightarrow H_2 + 2\,OH^- \qquad E° = 0.00\ \text{V versus RHE} \qquad (4.2.4)$$

### 4.2.2. ELECTROLYZER STRUCTURE

Two types of flow structures were considered for the electrolyzer configuration: a single-pass flow system and a recirculating flow system. Single-pass flow systems continuously pass fresh electrolyte solution through the electrolyzer. At the electrolyzer outlet, the electrolyte is separated from products and recycled. Alternatively, the recirculating flow involves first recirculating the electrolyte solution within an electrolyzer until a desired concentration of $H_2O_2$ is reached. Following this, the electrolyte and products are separated. The discontinuous nature of the recirculating electrolyzer and the continuous nature of the separation can be managed through an intermediate holding tank.

The production rate is assumed to be constant for both structures since the electrolyzer capacity is fixed at 2 MW. However, the concentration of $H_2O_2$ achieved at the electrolyzer outlet is significantly lower in a single-pass structure than for the

recirculating flow. [24, 34] This lower concentration will lead to a very difficult downstream separation. Thus, a recirculating structure was chosen despite the need for an extra tank. Following electrolysis, the anode and cathode outlets need to undergo a separation process to obtain products with the required specifications as well as recover the electrolyte.

### 4.2.3. $H_2$ Separation

The cathode side separation is relatively easy as $H_2$ is in the gas phase and the electrolyte solution is in the liquid phase. The cathode outlet (Stream 4) is cooled and flashed to recover the $H_2$, and the electrolyte is recirculated. The $H_2$ is then compressed in a three-stage compressor to a final pressure of 50 bar and stored (Stream 8).



### 4.2.4. Challenges in $H_2O_2$ Separation

On the anode side, however, $H_2O_2$ and the electrolyte solution are in the liquid phase, which poses a difficulty in the separation. $H_2O_2$ is commercially separated by vacuum distillation in the anthraquinone process. However, in our case, the distillation of the electrolyte solution and $H_2O_2$ will result in water as the top product and the electrolyte salts and $H_2O_2$ as the bottom products. Attempting to separate small amounts of $H_2O_2$ from the electrolyte salts yields a product with very low purity. Even if it is assumed that the electrolyte salts can be perfectly removed from the solution, resulting in a pure water and $H_2O_2$ mixture before distillation, the energy required to concentrate the solution to the typical 30 wt % $H_2O_2$ is 109 kWh $kg^{-1}$ product (based on Aspen Plus simulation). This significant energy demand, driven by the low concentrations in the electrolyzer outlet, is more than six times the aggregate energy consumption of the entire conventional anthraquinone process, which requires only 17.6 kWh $kg^{-1}$ product to produce $H_2O_2$. [34] To overcome these challenges, we are forced to consider other valorization methods. One such possible product is SPC made by complexing $H_2O_2$ with $Na_2CO_3$. In our process, the outlet stream of the electrolyzer consists of $H_2O_2$, $Na_2CO_3$, and water making SPC a feasible valorized product.

### 4.2.5. Design Basis and Assumptions

To begin designing the process, several assumptions were made, which are as follows:

1. All the design calculations are based on a 2 MW electrolyzer stack. This capacity is considered based on commercial electrolyzer stacks for producing $H_2$. [120]

2. BDD was selected as the anode material because of its high $FE_{H_2O_2}$ and overall stability as mentioned previously in this chapter.

3. Based on the literature, all the calculations in this paper are based on a cell potential of 5 V, current density of 0.1 A $cm^{-2}$, outlet $H_2O_2$ concentration of $6 \times 10^{-5}$ kmol $kg^{-1}$ and the faradaic efficiency toward $H_2O_2$ is 40%. [34, 76] The combination of the cell potential and current density is so chosen based on highest production of $H_2O_2$ at steady state.

4. The faradaic efficiency of the cathode toward $H_2$ was assumed to be 100%. [121, 122]

5. A well-controlled process with a fixed current density is assumed throughout the study, ensuring consistency in the electrolysis rate across various operational conditions.

6. The effect of sodium silicate was neglected in the process, and it was assumed to behave like sodium carbonate due to its similar chemical structure.

7. Considering the small quantity of NaOH added required to maintain anolyte pH, we do not include the small makeup stream in the design. Additionally, since the function of NaOH is pH maintenance, the $OH^-$ ions are reacted away at the anode, thus not affecting the process.

8. Sweden was selected as the process plant location because of cheap electricity prices as well as proximity to ports. [123]

9. The scope of the design is limited to the production of SPC and $H_2$. The transport, waste management and auxiliary units are out of scope.



### 4.2.6. VALORIZATION OF HYDROGEN PEROXIDE TO SODIUM PERCARBONATE

The anodic outlet stream of the electrolyzer (Stream 12) consisting of $Na_2CO_3$ electrolyte and $H_2O_2$ must be valorized to SPC. In the commercial production of SPC, $H_2O_2$ is mixed with sodium carbonate in a 1:1.0-1.5 molar ratio and crystallized. [124] The reaction is shown in Equation (4.2.5):

$$Na_2CO_3(aq) + 1.5\,H_2O_2(aq) \rightarrow Na_2CO_3 \cdot 1.5\,H_2O_2(aq) \tag{4.2.5}$$

However, $H_2O_2$ and $Na_2CO_3$ are present in a molar ratio of approximately 1:17 in the electrolyzer's outlet. Therefore, it is necessary to reduce the carbonate salt content. With the correct ratio, the commercial process involves the addition of sodium chloride (NaCl) to produce a salting-out effect for crystallization.

### 4.2.7. EXCESS WATER REMOVAL

Since the electrolyzer outlet is mostly water (Stream 12), in the first step, it is necessary to separate as much water as possible after the electrolyzer to reduce the downstream equipment sizing as well as increase the concentration of the product

in the stream. A multi-effect evaporator was used at this step to remove large quantities of water in an energy-efficient and cost-effective manner. The evaporated water containing the oxygen (Stream 13) is sent to a flash vessel where the oxygen is separated from the water. The water is recirculated in the system (Stream 15), whereas the oxygen is vented out (Stream 14). Even though a 2 MW stack produces 72 kg $h^{-1}$ of oxygen, it was found to be not economical to compress and sell it, and thus a decision was made to vent it. The concentrated solution of water, $Na_2CO_3$ electrolyte and $H_2O_2$ (Stream 18) is then sent for further processing.

### 4.2.8. Adjustment of pH



The water removal step is then followed by carbonate removal. In order to carry out an ion-based separation technique, the pH of the solution must be lowered to a value where $H_2O_2$ is not in its deprotonated form and only the electrolyte salt is in its ionic form. Thus, the pH of the solution is lowered from 13 (Stream 18) to 10 (Stream 22). This pH value is lower than the pKa of $H_2O_2$ which is 11.6. Hydrochloric acid (Stream 19) was chosen as the appropriate acid primarily because it is a strong acid and can act as an additional source of $Cl^-$ ions. The formation of water, NaCl salt, and carbon dioxide occurs upon adding this acid to the solution. Therefore, it is necessary to add a degasifier on Stream 22 following the acid treatment and before the ion-exchange resin to remove carbon dioxide. Stream 23, now adjusted for pH and free of carbon dioxide is sent downstream.

### 4.2.9. Excess Sodium Carbonate Removal

Following acid treatment, carbonate ions should be removed to reach the ideal ratio. Ion exchange is a method to exchange unwanted ions in water with other non-objectionable ionic substances. A strong base anion exchange resin in the chloride form can remove the carbonate ions by exchanging one carbonate ion for two chloride ions. [125] This process is reversible, and the resin can be regenerated with brine. The reaction is shown in Equation (4.2.6), with Z representing the resin:

$$Na_2CO_3 + 2\,Z \cdot Cl \rightarrow 2\,NaCl + Z_2 \cdot CO_3 \tag{4.2.6}$$

While other ion separation techniques such as electrodialysis and Donnan dialysis were considered, ion-exchange is most suitable here and was selected for the process design due to the following reasons: (1) It is easier in practice to implement compared to other considered technologies. (2) There is better control over how much carbonate is removed. (3) There is no additional NaCl salt required as it exchanges carbonate ions for chloride ions. (4) Pumping costs are the only energy requirement. (5) Resin can be regenerated to recover carbonate lost during operation.

Stream 23, containing water, $Na_2CO_3$ and $H_2O_2$ enters the ion-exchange unit and leaves with reduced carbonate in Stream 25 for crystallization.

### 4.2.10. SODIUM PERCARBONATE FORMATION AND CRYSTALLIZATION

After reducing the carbonate content in water to achieve the desired molar ratio for the SPC reaction, the next step is to cool down the ion-exchange outlet stream and then crystallize the salt. Here, SPC is crystallized, separated, and dried. This step was considered similar to commercial SPC production. [124] It was assumed that all the produced $H_2O_2$ is converted into SPC and all the produced SPC is recovered through crystallization (Stream 28). The leftover brine solution after the crystallization step (Stream 27) is used to regenerate the ion-exchange column, exchanging chloride for carbonate ions, to be recycled into the electrolyte tank (Stream 16). However, it is necessary to fully remove chloride ions from Stream 16 before recycling it to the electrolyzer. The excess chloride ions can be traced back to the addition of hydrochloric acid in the previous steps. To avoid chlorine gas formation and to recover carbonate from the purge stream, it was decided to employ Donnan dialysis. The draw solution was considered as the cleaned purge stream with water and $Na_2CO_3$ (Stream 31). There is an exchange of the carbonate and chlorine ions between Streams 16 and 31 within the unit. Thus, one of the outlets of the unit only consists of water and $Na_2CO_3$ (Stream 17) which is then recycled to the electrolyzer. The second outlet is a wastestream consisting of water and NaCl (Stream 32). However, the waste stream generated can be effectively managed by discharging it to a local water treatment facility via the municipal sewer system. This method offers a cost-effective solution, provided that the effluent composition complies with local regulations. [126] Additional water and $Na_2CO_3$ need to be continuously provided to the process to make up for the water consumed in the electrolyzer, water lost in the purge stream, and $Na_2CO_3$ lost through the SPC product, indicated via Steams 1 and 9.

It should be noted that flash drums, pumps, coolers, and the water evaporator were simulated using Aspen Plus software. All the other equipment calculations were done by hand. The separations in the degasifier, ion-exchange column, crystallizer, and Donnan dialysis were assumed perfect for ease of calculation. A detailed stream summary is presented in Table 4.A.5.

## 4.3. TECHNO-ECONOMICS

This section presents the detailed techno-economic calculation of the proposed process. First, a comprehensive list of equipment was compiled and approximately designed based on the process flow diagram. Capital expenditures (CAPEX) estimation was undertaken using factorial methods with an accuracy of ± 35%. [127] This method proves to be valuable at this project stage, where detailed engineering data is inaccessible, and approximating certain factors provides a rough estimate of the anticipated investment.

The approaches employed were the Lang and Guthrie methods. [128] The Lang method utilizes a Lang factor, which is an estimated ratio of the overall installation cost of the plant and equipment to the delivered equipment cost. The higher the Lang factor, the lower the impact of the equipment cost on the total installed cost and vice versa. The factor depends on the type of plant, equipment, and construction

material.

Since the proposed process incorporates specialized equipment such as the electrolyzer, expensive anode material, and common materials like stainless steel, a decision was made to differentiate between various equipment categories with a Lang factor varying between 1 and 4. The first category is regular equipment, like pumps, storage tanks, the dryer, and the evaporator. The Lang factor considered for this category is 4, primarily due to the extra costs associated with the construction material. The second category, special equipment, includes the crystallizer, the ion-exchange unit, and the Donnan dialysis unit, with a Lang factor of 3. This factor accounts for both the expensive material and the auxiliary parts and equipment required for the unit. The third category pertains to electrical equipment, such as the electrolyzer and the cathode, with a Lang factor of 2. This lower factor is attributed to the installation's emphasis on wiring rather than piping. An additional crucial consideration is the exceptionally expensive anode price, constituting nearly 75% of the total bare equipment cost. Due to the anode costs being related solely to the material price, the Lang factor for the anode is set to 1.



The bare equipment cost for the electrolyzer was calculated based on the area of the anode, cathode, membrane, and housing. [97] The remaining equipment costs were calculated using the Matche cost estimator. [129] The Matche cost estimator calculates equipment costs using a cost index value based on the year and the specifications of the equipment in question. These specifications can include the construction material, flow rate, total volume, length, etc. The bare equipment costs are presented in Table 4.A.4. The complete breakdown of capital investment is shown in Table 4.3.1 where the total capital investment was calculated to be 64.52 M€. Further costs above the installed equipment costs are calculated using approximate percentages based on industrial heuristics. [130] For all equipment types except the anode, the costs outside battery limits and the contingency costs are taken as 50% and 37.5% of the installed equipment cost, respectively. The fixed capital investment is then the sum of those three costs together. The total capital investment for each equipment type includes a 15% and 10% cost for working capital and start-up costs, respectively, which are added to the fixed capital investment.

In general, operational expenditures (OPEX) refer to the day-to-day costs an organization incurs to maintain its regular operations, and some of the OPEX costs are dependent on the CAPEX costs. OPEX costs include direct production costs, capital expenditures, plant overhead and general expenses. Direct production costs include raw materials, utilities, equipment maintenance and repair, labor required for daily operations, and patent costs. Capital charges were calculated for a 10-year lifetime of the project and at a 12% interest rate on the investment amount. Capital charge is the cost to the business for borrowing the required capital, or in other words, it is the necessary return on the made investment. The 10-year lifetime is considered because the BDD anode is very expensive and can potentially last up to 10 years without needing replacement. [97] The 12% interest rate was decided based on investment risks and inflation. Plant overhead was defined as the total cost involved in operations which accounts for operational efficiency and the well-being of the facility (safety, recreation, and laboratories). This cannot be traced

Table 4.3.1: Breakdown of Total Capital Investment (TCI)

| Category | Regular Equip-ment | Special Equip-ment | Electro-lyzer | Cath-ode | Anode | Total |
|---|---|---|---|---|---|---|
| Equipment Cost (M€) | 4.089 | 1.168 | 0.054 | 0.003 | 14.579 | 19.893 |
| Lang Factor | 4 | 3 | 2 | 2 | 1 | - |
| Installed Equipment Cost (M€) | 16.354 | 3.505 | 0.108 | 0.006 | 14.582 | 34.555 |
| Costs Outside Battery Limits (M€) | 8.177 | 1.680 | 0.054 | 0.003 | 0.003 | 9.989 |
| Contingency (M€) | 6.133 | 1.314 | 0.040 | 0.002 | 0.002 | 7.492 |
| Fixed Capital Investment (M€) | 30.664 | 6.572 | 0.202 | 0.010 | 14.587 | 52.036 |
| Working Capital (M€) | 6.133 | 1.314 | 0.040 | 0.002 | 0.002 | 7.492 |
| Start-Up Cost (M€) | 4.089 | 0.876 | 0.027 | 0.001 | 0.001 | 4.995 |
| Total Capital Investment (M€) | 40.886 | 8.762 | 0.27 | 0.014 | 14.59 | 64.522 |

directly to the product. Additionally, other fixed and variable general expenses were considered. Fixed expenses include sales and marketing, engineering services and R&D. Variable costs include distribution, training, and management. Operational expenditures amounted to 21.59 M€ $yr^{-1}$. Table 4.3.2 shows the cost breakdown of OPEX, where the plant overhead and general expenses are 7.5% and 15% of the Total Manufacturing Costs, respectively. A more detailed breakdown is presented in Tables 4.A.1 – 4.A.3.

Table 4.3.2: Breakdown of operating costs

| Category | Amount (M€ $yr^{-1}$) |
|---|---|
| Direct Production Costs | 6.10 |
| •Fixed Costs | 0.05 |
| •Variable Costs | 6.05 |
| Capital Charges | 11.42 |
| Plant Overhead | 0.68 |
| General Expenses | 3.39 |
| •Fixed (Sales & Marketing, Engineering, R&D) | 1.36 |
| •Variable (Distribution, Training, Management) | 2.03 |
| Total Manufacturing Costs (TMC) | 21.59 |

The annual revenue generated by selling hydrogen and SPC produced by a 2 MW stack with prices of 5000 € $tonne^{-1}$ and 780 € $tonne^{-1}$, respectively, was found

to be 2.54 M€. The disparity between the two sale prices is due to the low molar mass of $H_2$, where there are approximately 75 times as many moles of $H_2$ than there are moles of SPC in one tonne of product. Based on the annual revenue and the calculated OPEX, the annual cash flow was estimated. A negative annual cash flow was calculated for the designed process at -19.05 M€ $yr^{-1}$. The main cost driver of OPEX is the cost of capital (53% of OPEX) which is majorly driven by the expensive anode material. Therefore, with current equipment efficiencies and prices for raw materials, utilities and final products, a one-stack electrolyzer project is considered unprofitable. However, it is considered that for larger capacity projects, operating costs will not increase linearly, hence a breakeven analysis was conducted.

A breakeven analysis was performed on the project's production capacity, according to the six-tenths heuristic. According to this heuristic, if the cost of a given unit at one capacity is known, the cost of a similar unit at $X$ times the capacity of the first is calculated by Equation (4.3.1):

$$\frac{\text{Investment for } X \text{ times given capacity}}{\text{Investment for given capacity}} = X^{1-M} \tag{4.3.1}$$

For all equipment except the electrolyzer, it is considered that the scaling-up costs are minimal, therefore factor $M$ was given the value of 0.4. However, assuming that the electrolyzer is a modular piece of equipment, $M$ was considered 0.2 for the electrolyzer, the anode, and the cathode. The breakeven analysis for capacities of up to 60% of the global SPC market, considering a 1.54 B€ market capacity, is shown in Figure 4.3.1. According to the figure, the breakeven point at which the project is considered profitable was found at a capacity equivalent to 39% of the global market. This market share translates to a process operating 308 electrolyzer stacks (2 MW each). It is important to note that the capacity serves only as an indicator and not a possible scenario, since the global market distribution can be a limiting factor on it.

Further economic analysis was conducted at a capacity of 339 stacks (10% higher than the breakeven point) including Internal Rate of Return (IRR) and Net Present Value (NPV). IRR represents the discount rate at which the NPV of an investment becomes zero. A higher IRR typically indicates a more attractive investment opportunity. The NPV for a lifetime of 10 years was calculated based on annual operating expenses, expected depreciation, and taxes. The NPV at the end of 10 years was negative, indicating that this process as a business proposition is not profitable in its current form. Based on cash flows for 10 years since the commencement of the plant, the IRR was 7.9%. Even though at this scale the IRR is positive, it is not large enough to yield a positive NPV (-509.25 M€ after 10 years), indicating an economically unfavorable investment. Thus, it was deemed critical to analyze the factors that affect these costs the most and understand if and how this design can be made into an economically feasible project. In Figure 4.3.2, the cost review is depicted, leading to the need for a sensitivity analysis of the most impactful parameters.

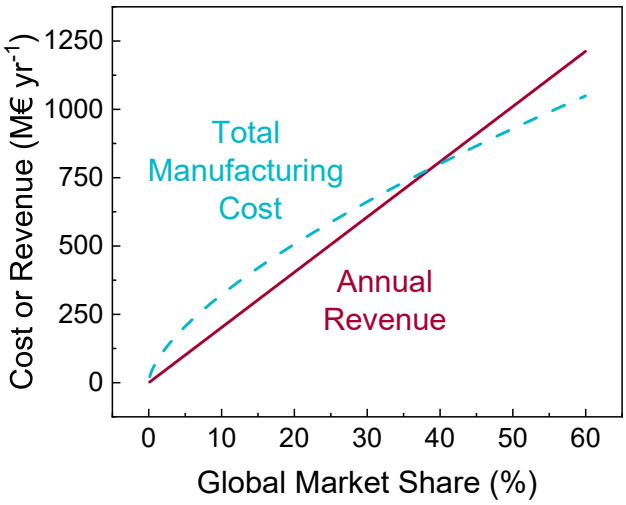


Figure 4.3.1: Breakeven point analysis based on a six-tenths heuristic for scaling the plant capacity.

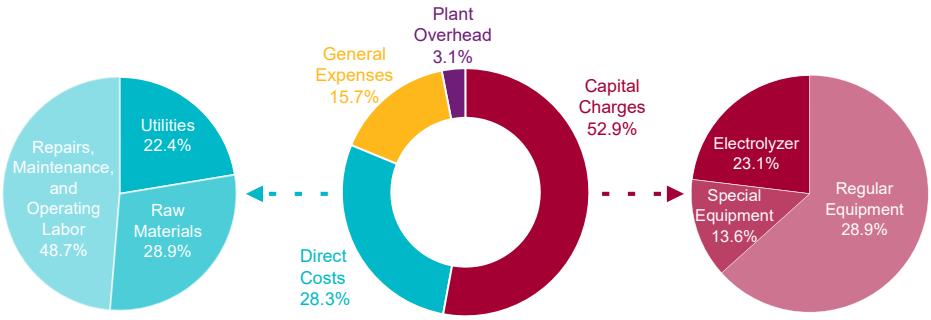


Figure 4.3.2: Cost review of the total manufacturing costs.

## 4.4. SENSITIVITY ANALYSIS

A sensitivity analysis evaluates the effect of changes in input parameters on a model's or system's output. This analysis allows one to identify the pivotal factors of a system or process. This can assist future studies by focusing on the most critical factors. This study focused on the cost drivers' impacts on the process economics. In our case, the main cost drivers investigated are electricity price, anode price, $FE_{H_2O_2}$, product prices and tax subsidies. To gain a comprehensive understanding of the impact of cost drivers, two different sensitivity analyses were conducted: (1) Breakeven Point Analysis and (2) IRR and NPV Analyses.

### 4.4.1. Breakeven Point Analysis

From Figure 4.3.1, it was noted that the breakeven point for the process is 308 stacks, which represents 616 MW of plant capacity and 39% of the worldwide market for SPC, which is considered an unreasonable scale. In this section, we investigate the influence of cost drivers on the breakeven point to identify targets that can make this process more economically feasible. Figure 4.4.1a shows the effects of key inputs such as electricity price, anode price, and faradaic efficiency on the breakeven point, while Figure 4.4.1b shows the effect of sale prices of $H_2$ and SPC on the breakeven point.

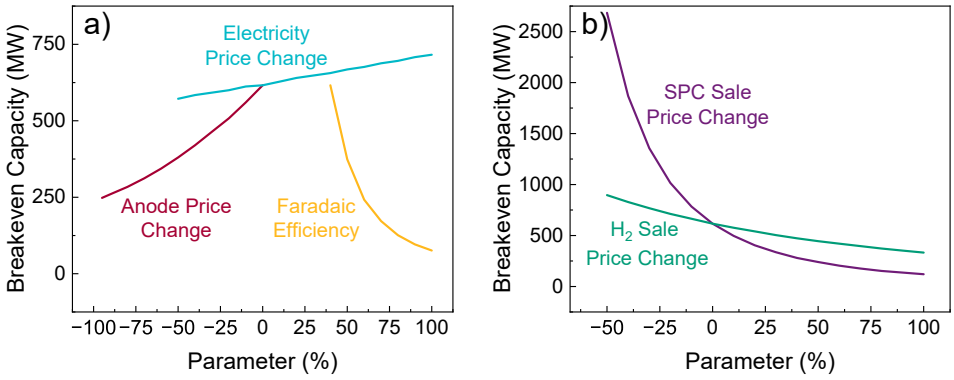


Figure 4.4.1: Effect of the a) inputs and b) product sale prices on the breakeven point.

**Key Inputs** The electricity price can change throughout the year and have a significant impact on process economics. Electricity prices historically have shown great volatility which could result in high uncertainties for the operating expenses, and therefore, for the overall economics of the process. In the past five years, electricity prices have spiked up to approximately 10 times higher than the average, due to extreme circumstances, and on average they fluctuate between -50% and +100% from today's prices (30-120 € $MWh^{-1}$). [123] As a result, a sensitivity analysis was conducted using this specific range of values. In the case of a 50% reduction in the electricity price, the breakeven point for the global market share of SPC decreases approximately by 5% from around 40% to about 35%. While electricity prices have an enormous impact on a standard alkaline water electrolysis plant's economic viability, they affect this process very little.

One of the most important factors affecting CAPEX is the anode cost. This high cost is attributed to the current manufacturing technology. Advancements in material science and manufacturing technology could lead to the development of alternative materials (not necessarily BDD) with comparable or higher $FE_{H_2O_2}$ at significantly reduced costs. Thus, by reducing the anode cost from 0 to 95%, its effect on

the breakeven point was investigated. Results show a significant change in plant capacity and breakeven point by changing the anode cost. A 95% reduction in the anode price leads to a breakeven point of around 15% of the global SPC market share which is a reasonable capacity. However, it could be challenging to develop a novel, stable and cheap anode for this process in the coming years.

In electrolysis, the faradaic efficiency is of paramount importance as it directly influences the efficacy of electrochemical processes crucial for sustainable energy technologies. It measures the extent to which the desired electrochemical reactions occur, ensuring that energy is efficiently converted without wasteful side reactions. A high $FE_{H_2O_2}$ signifies an optimized electrolysis process, minimizing energy losses and maximizing the yield of the intended products. Here we identify the effect of $FE_{H_2O_2}$ on the economic breakeven points. A sensitivity analysis was done on the $FE_{H_2O_2}$ range of 40% to an ideal case of 100%. Based on the current technology level (FE of around 40%), to reach a breakeven point, a plant size of 616 MW (39% of the market) should be targeted. However, in the ideal case (FE of 100%), plant size targets and market share can be significantly lowered to around 76 MW and 5%, respectively, to reach the breakeven point. As previously indicated, due to the low concentration of product at the electrolyzer outlet, the separation stays the same by increasing the $FE_{H_2O_2}$ (same CAPEX). The increase in $FE_{H_2O_2}$, however, directly increases revenue (production rate), while only OPEX changes. Therefore, $FE_{H_2O_2}$ was found to be the most important factor in this techno-economic analysis. Furthermore, anodes with high $FE_{H_2O_2}$ of approximately 80% have already been demonstrated at lab scales, indicating that this scenario is not highly unlikely to take place. [24, 85]



**Product Prices** SPC and hydrogen sale prices may change due to market fluctuations. Thus, a percent change in the individual product sale prices from -50% to +100% was examined. This corresponded to a constant $H_2$ sale price of 5,000 € $tonne^{-1}$ with the SPC sale price ranging from 390 to 1,560 € $tonne^{-1}$), and a constant SPC sale price of 780 € $tonne^{-1}$ with the $H_2$ sale price ranging from 2500 to 10,000 € $tonne^{-1}$. Figure 4.4.1b shows that if the SPC price is doubled, the breakeven point drops to almost 7.5% of the global SPC market share, whereas if the $H_2$ price is doubled, the breakeven point is almost 20%. Due to the larger mass of SPC produced compared to the mass of $H_2$ produced, the impact of changing percarbonate sale price is greater. However, it should be noted that neither price will remain constant, and both prices will fluctuate in the long run.

### 4.4.2. IRR and NPV Analyses

To determine the effect of cost drivers on IRR and NPV, another sensitivity analysis was performed. This analysis was conducted based on a realistic plant capacity of 200 MW (100 stacks) to ensure a fair comparison with the previous section's base analysis. For the chosen capacity of 200 MW, the IRR and the NPV were calculated as -5.8% and -806 M€, respectively.

**Key Inputs** The effect of the same key inputs used in Section 4.4.1 on IRR and NPV is shown in Figure 4.4.2. In addition to these inputs, one more parameter was considered: a tax credit. To promote green hydrogen production, the Clean Hydrogen Production Tax Credit is one of the most important policies. This tax credit is intended to stimulate the domestic clean hydrogen industry and reduce the cost gap between green and fossil-based hydrogen. Assuming the project could be part of a green transition policy, the tax rate could drop from 20.6% to zero.

The IRR and the NPV increase steadily as the electricity price decreases, reaching -4.5% and -758 M€, respectively. On the other hand, for a 100% increase in the electricity price, the IRR decreases to -8.8% and the NPV decreases to -902 M€. With a 95% reduction in the anode cost, the IRR is 4.8% and the NPV is negative at -222 M€. This indicates that along with anode cost reduction, other parameters must change favorably to consider this project an acceptable investment. Considering an ideal $FE_{H_2O_2}$ of 100%, the IRR and NPV are 19.6% and 447 M€, respectively. Even if a more feasible efficiency of 75% is considered as a target for the future, the IRR and NPV can be significantly increased to approximately 10.6% and -75 M€ compared to around only -5.8% and -806 M€ at the base case of 40% $FE_{H_2O_2}$. Lastly, it can seen that the IRR and NPV increase steadily as the tax rate decreases, reaching -4.2% and -767 M€, respectively. This indicates that tax subsidies do not have a significant influence on the project's economic viability, especially when compared to the other inputs.

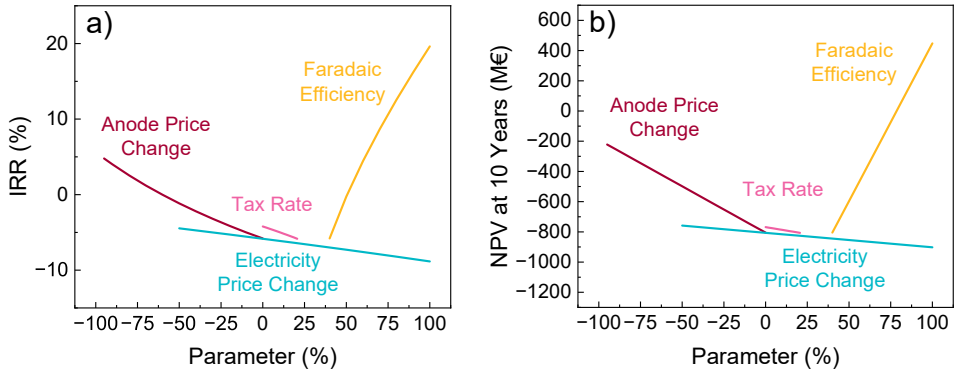


Figure 4.4.2: Effect of key input parameters on the a) IRR and b) NPV.

In addition to the IRR and the NPV, the effect of the electricity price on utility costs and manufacturing costs was also calculated, shown in Figure 4.4.3. In extreme conditions, utility costs may vary between -37 and +75%, indicating a relatively high impact of the electricity price on utility costs. But the impact on total manufacturing costs (TMC) is much lower, where a -50 to +100% change in the electricity price results in only a variation of -3 to +5% in TMC.

The anode price clearly has a large impact on the process economics, and the effect of the anode price change on CAPEX and OPEX specifically is shown in

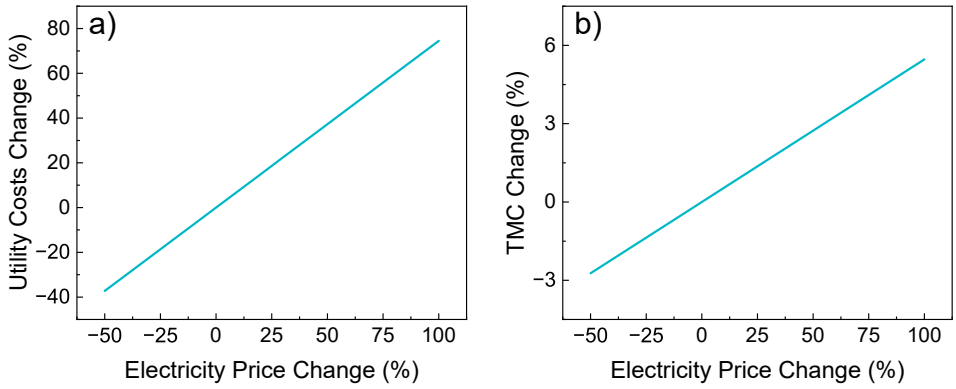


Figure 4.4.3: Effect of the electricity price on the a) utility costs and b) TMC.

Figure 4.4.4. Lowering the anode cost from 0% to 95%, can reduce the CAPEX up to approximately 40%, with an expected linear relationship. But because changes in CAPEX result in changes in capital charge, the OPEX value also changes. The anode price reduction reduces the OPEX by approximately 28%.

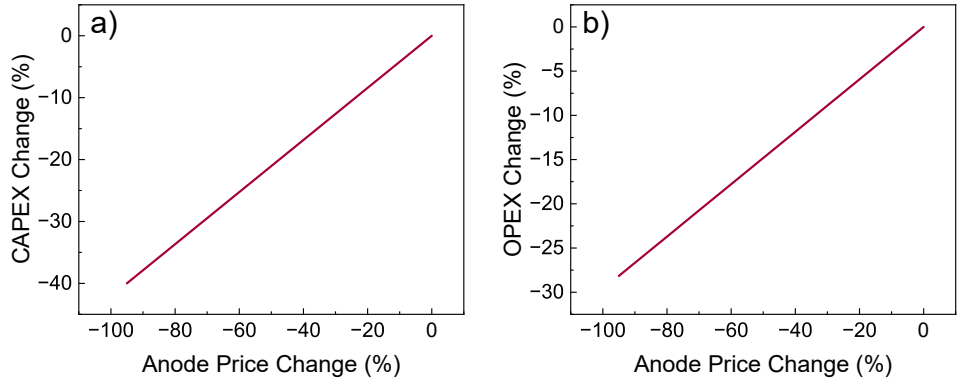


Figure 4.4.4: Effect of the electricity price on the a) CAPEX and b) OPEX.

**Product Prices** The effect of product sale prices on the IRR and NPV were also calculated, shown in Figure 4.4.5. For SPC sold at a 100% higher price, the IRR is 13.2% with a positive NPV of 69.44 M€ after 10 years. This is a plausible scenario considering this compound finds growing applications in cleaning powder and laundry detergents as an eco-friendly alternative to chlorine, and can be marketed as a green product. [131] Increasing the hydrogen sale price by 100% higher price,

results in an IRR of approximately 2%, but a negative NPV after 10 years of approximately -600 M€. Considering the increased demand for hydrogen, this price increase might be possible, but likely not since the base case price of 5 € $kg^{-1}$ already represents a green hydrogen premium. There is a greater impact on the IRR and NPV when it comes to SPC price changes since the production rate by mass in this process is far higher than that of hydrogen. Predictably, the best-case scenario would be if both products could be sold at a higher price.

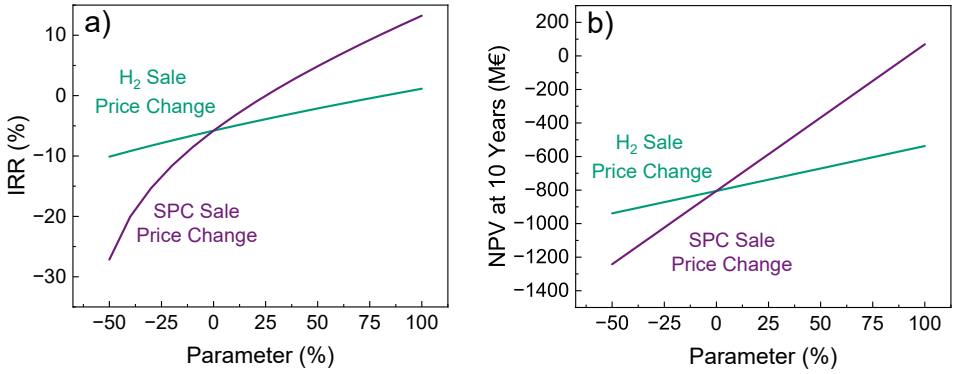


Figure 4.4.5: Effect of the sodium percarbonate sale price on the a) IRR and b) NPV.

### 4.4.3. Overview of the Sensitivity Analysis

The sensitivity analysis demonstrated how the project's economic performance varies with changing cost drivers. Some of these cost drivers have more impact than others, with some changes able to single-handedly bring the process design into economic viability. Table 4.4.1 illustrates how IRR and NPV are affected by changing cost drivers to their extreme values in the best case scenarios, and are listed in order of most dramatic improvement after the base case.

Table 4.4.1: Comparison of the most favorable scenarios

| Scenario | IRR (%) | NPV (M€) |
|---|---|---|
| Base Case | -5.8 | -805 |
| 100% Faradaic Efficiency | 19.6 | 447.39 |
| 100% SPC Sale Price Increase | 13.2 | 69.43 |
| 95% Anode Price Decrease | 4.8 | -222.01 |
| 100% $H_2$ Sale Price Increase | 1.1 | -537.81 |
| 100% Tax Subsidy Increase | -4.2 | -768.66 |
| 50% Electricity Price Decrease | -4.5 | -758.45 |

## 4.5. Multi-Parameter Sensitivity Analysis

The preceding analysis describes well how the process economics are affected by changing a single parameter while keeping the others constant. However, it rarely so happens that only one parameter changes. Thus, a two-parameter sensitivity analysis was performed on key parameters identified in the previous section, selecting the top three of faradaic efficiency, SPC sale price, and anode price.

### 4.5.1. Effect of Changing Faradaic Efficiency and SPC Price

Keeping in mind the most influential and likely parameters to change, a two-parameter sensitivity analysis was performed on the breakeven point, IRR and NPV by changing the $FE_{H_2O_2}$ and the SPC price. The results are shown in Figures 4.5.1 and 4.5.2.



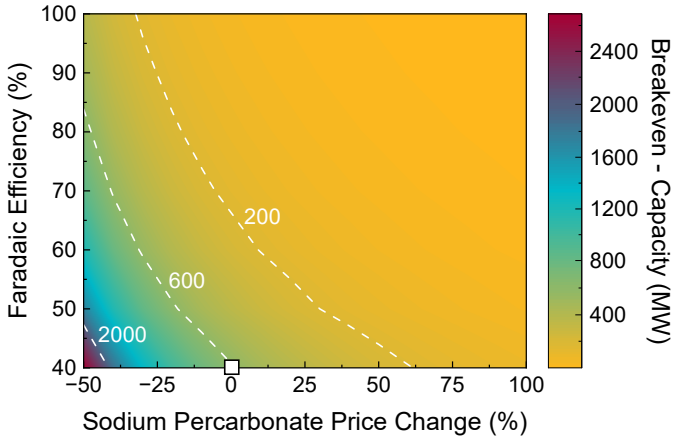


Figure 4.5.1: Effect of changes in the sodium percarbonate sale price and the faradaic efficiency on the breakeven point (white marker shows the current situation).

The breakeven point improves drastically with a positive change in the $FE_{H_2O_2}$ and SPC price. With a 75% $FE_{H_2O_2}$, the breakeven point ranges from 74 stacks (148 MW) to 13 stacks (26 MW) for a 0 to 100% increase in the price of SPC.

It can be seen that with the improvement in $FE_{H_2O_2}$ and an increase in SPC price, the process is economically more favorable. As seen in Figure 4.5.2, if $FE_{H_2O_2}$ can be improved to 75% and SPC can be sold at a price 0 to 100% more than the current cost, the IRR ranges from 10.6 to 35.8%, and the NPV ranges from -75 to 1383 M€.

### 4.5.2. Effect of Changing Anode Price and SPC Price

Another two-way sensitivity analysis was performed on the breakeven point, IRR and NPV by changing the anode price and the SPC price. The results are shown in Figures 4.5.3 and 4.5.4.

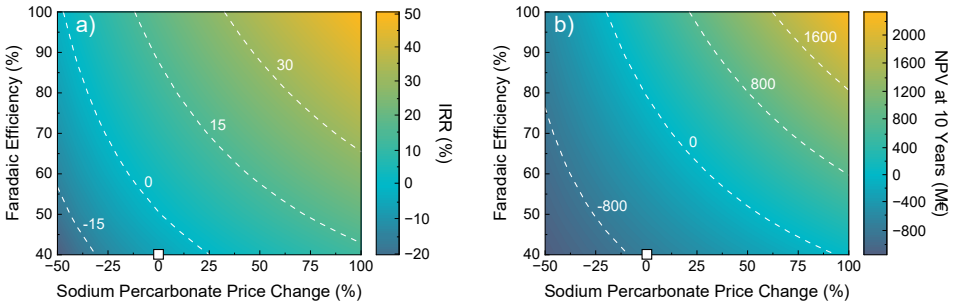


Figure 4.5.2: Effect of changes in the sodium percarbonate sale price and the faradaic efficiency on the a) IRR and b) NPV (white marker shows the current situation).

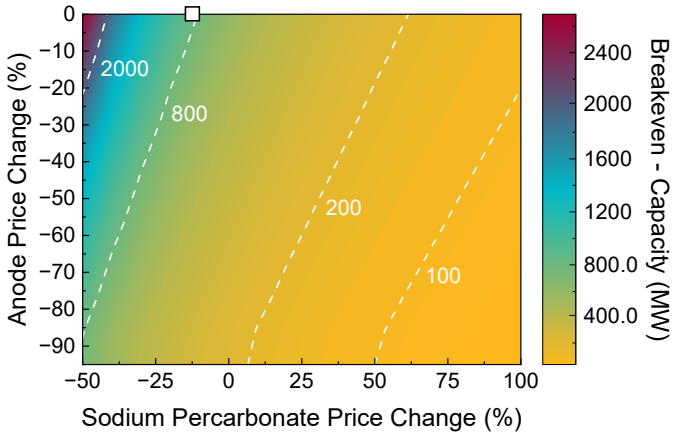


Figure 4.5.3: Effect of changes in the sodium percarbonate sale price and the anode price on the breakeven point (white marker shows the current situation).

The breakeven point improves with a positive change in the anode price and SPC price as well. With an 80% decrease in the anode price, the breakeven point ranges from 132 stacks (264 MW) to 31 stacks (62 MW) for a 0 to 100% increase in the price of SPC.

If the anode price decreases by 80% and SPC can be sold at a price 0 to 100% more than the current cost, the IRR ranges from 2.5 to 25.4%, and the NPV ranges from -290 M€ to 490 M€.

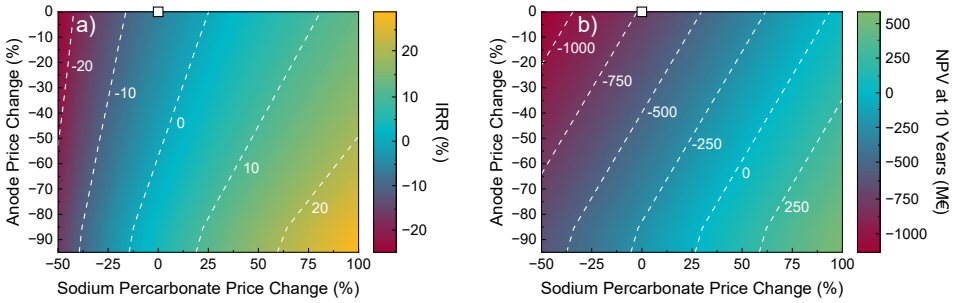


Figure 4.5.4: Effect of changes in the sodium percarbonate sale price and the anode price on the a) IRR and b) NPV (white marker shows the current situation).



### 4.5.3. EFFECT OF CHANGING ANODE PRICE AND FARADAIC EFFICIENCY

Multi-parameters analysis was also performed on the breakeven point, IRR and NPV by changing the anode price and faradaic efficiency. The results are shown in Figures 4.5.5 and 4.5.6.

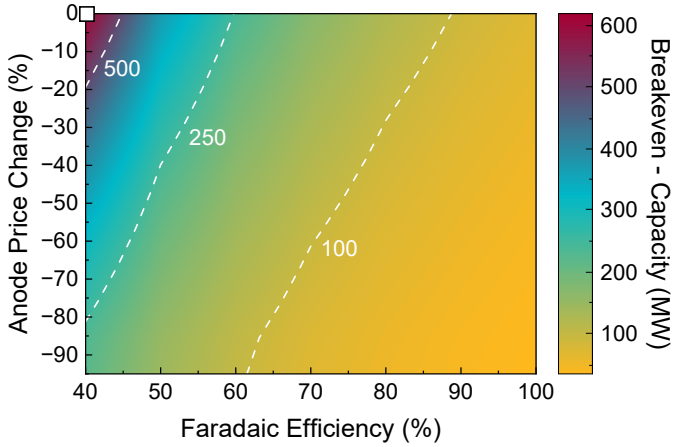


Figure 4.5.5: Effect of changes in the faradaic efficiency and the anode price on the breakeven point (white marker shows the current situation).

The breakeven point benefits from a decrease in anode price and an increase in faradaic efficiency. When the anode price drops by 80%, the breakeven point spans from 132 stacks (264 MW) to 21 stacks (42 MW), depending on faradaic efficiency, which varies between 40 and 100%.

Considering an anode price that is reduced by 80% and a faradaic efficiency

ranging between 40 and 100%, the IRR ranges from 2.5 to 33.7%, and the NPV ranges from -290 to 827 M€, as shown in Figure 4.5.6.

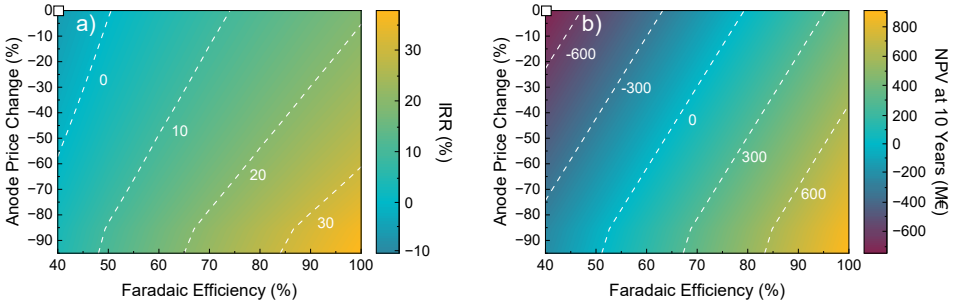


Figure 4.5.6: Effect of changes in the faradaic efficiency and the anode price on the a) IRR and b) NPV (white marker shows the current situation).

## 4.5.4. Overview of the Multi-Parameter Sensitivity Analysis

The multi-parameter sensitivity analysis results highlight the positive impact on economics when two parameters change favorably. As illustrated by the figures provided, attaining a lower breakeven point is comparatively easier and more feasible. With a promising change in multiple variables, NPV tends toward the positive side after 10 years with an IRR value that is more attractive to investors.

## 4.5.5. Scenarios' Likelihood Evaluation

It is considered that these scenarios would not occur with the same likelihood. According to the literature, it may be very likely that the $FE_{H_2O_2}$ will increase in the near future. Hydrogen and SPC prices may rise in the future due to high market demand, underestimation of the price in the current study, and the trend toward green technology. This scenario is very likely, as it reflects the current and projected situation of the hydrogen market. It also reflects the environmental and social factors that influence consumers' preferences and choices.

On the other hand, the electricity price scenario is not very likely, as it faces many challenges and uncertainties, such as the reliability and availability of renewable energy, the cost and efficiency of energy storage, and the market and political forces that affect the energy sector. The anode price scenario is also not very likely soon, either, as it requires significant investment and research in material science and the overcoming of technical and operational difficulties.

Assessing the likelihood of tax subsidies is challenging, as they are highly dependent on the plant's location, the prevailing policies, and the broader political landscape. In practice, tax rates may exceed the assumptions made in this study or fall within the considered range. However, their impact on the overall economics is relatively minor compared to other key parameters.

## 4.6. CONCLUSIONS

The purpose of this work was to bridge the gap between academic studies and the practical challenges regarding the co-production of $H_2O_2$ via water electrolysis. The high cost of hydrogen production via water electrolysis led to some studies recommending the substitution of oxygen production for $H_2O_2$, which has a higher value. However, no studies explored the feasibility and costs of separating $H_2O_2$ from the electrolyte. Hydrogen peroxide separation was found to be extremely difficult due to the presence of other ions that cannot be easily removed. Thus, this study presented a novel conceptual process design as well as a techno-economic evaluation for the valorization of $H_2O_2$ into SPC. This decision was driven by the market feasibility of SPC and the availability of necessary raw materials in the electrolyzer outlet stream.

For the plant location Sweden was chosen, leveraging its low electricity costs, market accessibility, and port availability. The plant's capacity was selected based on a modular 2 MW electrolyzer stack, employing a recirculating structure to achieve higher $H_2O_2$ concentrations. A boron-doped diamond anode was selected due to its better performance at high current densities and extended lifetime.

An economic analysis was conducted, and results revealed a projected CAPEX of 64.52 M€ and an annual OPEX of 21.59 M€ for a 2 MW electrolyzer stack (production rate of 2.5 kt $yr^{-1}$ of sodium percarbonate). With an anticipated annual revenue of 2.54 M€ per stack, a capacity of 308 stacks (616 MW) was required to breakeven with operating expenditure, representing a substantial portion of the global SPC market share (39%).

A more detailed economic evaluation of IRR and NPV considering a capacity 10% above breakeven of 339 stacks (678 MW) also revealed less favorable results. With a CAPEX of 3.2 B€ and OPEX of 870 M€, the IRR was 7.9%, and the NPV after 10 years was -509.25 M€.

While the proposed process design faces economic challenges using existing technologies, further exploration was carried out through sensitivity analysis to highlight the key targets for future advancements. It was seen that adjusting cost drivers including product prices, electricity price, anode price, and $FE_{H_2O_2}$ can lead to a significant reduction in the breakeven point as well as a considerable increase in the IRR and the NPV. $FE_{H_2O_2}$ followed by SPC sale price were found to be the most crucial parameters. In the 2 MW base case, an ideal $FE_{H_2O_2}$ of 100% resulted in around 20% IRR and 447 M€ NPV. These numbers were calculated to be around 13% and 69 M€, respectively, for the 100% increase in SPC sale price. The electricity price, however, was found to be the least influential parameter, contrary to what is the case for alkaline water electrolysis. The multi-parameter sensitivity analysis demonstrated that favorable change in multiple cost drivers has a significant impact on the economics. For a 0 to 100% increase in the price of SPC, with an 80% decrease in the anode price, the NPV ranges from -290 to 490 M€ with IRR ranging from 2.5 to 25.4%, whereas, with an increase from 40% to 75% $FE_{H_2O_2}$, the NPV ranges from -75 to 1383 M€ with IRR ranging from 10.6% to 35.8%.

While sensitivity analysis and adjustments to individual and multiple parameters can be used to enhance the economic viability of the process, it is crucial to note

that there is room for additional exploration and optimization. First, delving deeper into the analysis of critical parameters, particularly focusing on the influence of raw material prices and the utilization of chemical stabilizers. Additionally, since the economic analysis involves assumptions to reduce complexity, it is suggested to consider a broader spectrum of economic indicators related to the efficiency and sustainability of the process. Finally, it is recommended to investigate the current market dynamics to understand whether sodium percarbonate can also replace other products in the market and investigate whether there are new applications which can leverage the overall market capitalization.

## 4.A. Appendix - Process Design Details

The following tables give details of the process design.

Table 4.A.1: Chemicals and Energy Prices

| Material | Price |
|---|---|
| Deionized Water | 7 € $tonne^{-1}$ |
| Sodium Carbonate | 250 € $tonne^{-1}$ |
| HCl | 150 € $tonne^{-1}$ |
| $H_2$ Gas (Compressed) | 5000 € $tonne^{-1}$ |
| Sodium Percarbonate | 780 € $tonne^{-1}$ |
| Electricity | 60 € $MWh^{-1}$ |
| Low-Pressure Steam | 5.4 € $tonne^{-1}$ |



Table 4.A.2: More detailed breakdown of operating costs

| Category | Amount (M€ $yr^{-1}$) | Percent of TMC (%) |
|---|---|---|
| Direct Production Costs | 6.10 | 28.25 |
| •Fixed Costs | 0.05 | 0.23 |
| Patents | 0.05 | 0.23 |
| •Variable Costs | 6.05 | 28.02 |
| Utilities | 1.36 | 6.30 |
| Maintenance & Repairs | 1.13 | 5.23 |
| Raw Materials | 1.75 | 8.11 |
| Operating Labor | 1.81 | 8.38 |
| Capital Charges | 11.42 | 52.89 |
| Plant Overhead | 0.68 | 3.15 |
| General Expenses | 3.39 | 15.70 |
| •Fixed (Sales & Marketing, Engineering, R&D) | 1.36 | 6.30 |
| •Variable (Distribution, Training, Management) | 2.03 | 9.40 |
| Total Manufacturing Costs (TMC) | 21.59 | 100.00 |

Table 4.A.3: Operational expenses per unit

| Unit or Component | Quantity | Hourly Price (€ $hr^{-1}$) | Yearly Price (€ $hr^{-1}$) |
|---|---|---|---|
| **Electrolyzer (2 MW)** | | | **1,401,798** |
| Electricity | 2 MWh $hr^{-1}$ | 120.00 | 960,000 |
| Make-Up Water | 268.71 kg $hr^{-1}$ | 1.88 | 15,048 |
| Sodium Carbonate | 211.98 kg $hr^{-1}$ | 52.99 | 423,960 |
| Cathode Material (1 year) | | | 2,790 |
| **Water Evaporator** | | | **281,473** |
| Electricity | 25 kWh $hr^{-1}$ | 1.50 | 12,000 |
| LP Steam | 6.23 ton $hr^{-1}$ | 33.68 | 269,473 |
| **Acidifier (Mixer)** | | | **763,211** |
| Estimated Costs | 100% CAPEX | | 54,011 |
| HCl | 591 kg/hr | 88.65 | 709,200 |
| **Ion Exchange Column** | | | **50,928** |
| Resin (1 per year) | 60,847 kg $yr^{-1}$ | | 50,928 |
| **Filter (1 per year)** | | | **140,000** |
| **Dryer** | | | **21,504** |
| Centrifuge Power | 30 kW | 1.80 | 14,400 |
| Dryer Power | 14.8 kW | 0.89 | 7,104 |
| **Pumps** | | | **1,844** |
| Pump 1 Power | 1.91 kW | 0.115 | 917 |
| Pump 2 Power | 1.91 kW | 0.115 | 917 |
| Pump 3 Power | 0.02 kW | 0.00 | 10 |
| **Coolers** | | | **21,695** |
| Cooling Water 1 | 3.25 MW | 2.31 | 18,481 |
| Cooling Water 2 | 0.566 MW | 0.40 | 3,214 |
| **Compressor** | | | 1,400 |
| Power | 30 kW | 1.80 | 1,400 |

Table 4.A.4: Full equipment list and costs

| Equipment | Quantity | Cost (M€) | Total Cost (M€) |
|---|---|---|---|
| Electrolyzer (2 MW) | 1 | 14.636 | 14.636 |
| Water Evaporator | 1 | 2.633 | 2.633 |
| Acidifier (Mixer) | 1 | 0.054 | 0.054 |
| Ion-Exchange | 2 | 0.199 | 0.397 |
| Crystallizer | 1 | 0.384 | 0.384 |
| Flash 1 | 1 | 0.097 | 0.097 |
| Flash 2 | 1 | 0.085 | 0.085 |
| Filter | 1 | 0.140 | 0.140 |
| Filtration and Drier | 1 | 0.222 | 0.222 |
| Pump 1 | 1 | 0.014 | 0.014 |
| Pump 2 | 1 | 0.014 | 0.014 |
| Pump 3 | 1 | 0.088 | 0.088 |
| Cooler 1 | 1 | 0.279 | 0.279 |
| Cooler 2 | 1 | 0.099 | 0.099 |
| Degasifier | 1 | 0.168 | 0.168 |
| Blower | 1 | 0.031 | 0.031 |
| Donnan Dialysis | 1 | 2.177 | 2.177 |
| Compressor | 1 | 0.072 | 0.072 |
| Electrolyte Tank 1 | 1 | 0.046 | 0.046 |
| Electrolyte Tank 2 | 1 | 0.046 | 0.046 |

Table 4.A.5: Summary of stream contents as labeled in Figure 4.2.1, with each component in kg $h^{-1}$

| Stream | $H_2O$ | $H_2$ | $H_2O_2$ | $Na_2CO_3$ | $O_2$ | HCl | $CO_2$ | NaCl | SPC | Total |
|---|---|---|---|---|---|---|---|---|---|---|
| 1 | 268.710 | 0.000 | 0.000 | 0.000 | 0.000 | 0.000 | 0.000 | 0.000 | 0.000 | 268.710 |
| 2 | 49638.986 | 0.000 | 0.000 | 0.000 | 0.000 | 0.000 | 0.000 | 0.000 | 0.000 | 49638.986 |
| 3 | 49638.986 | 0.000 | 0.000 | 0.000 | 0.000 | 0.000 | 0.000 | 0.000 | 0.000 | 49638.986 |
| 4 | 49370.276 | 14.916 | 0.000 | 0.000 | 0.000 | 0.000 | 0.000 | 0.000 | 0.000 | 49385.192 |
| 5 | 49370.276 | 14.916 | 0.000 | 0.000 | 0.000 | 0.000 | 0.000 | 0.000 | 0.000 | 49385.192 |
| 6 | 0.000 | 14.916 | 0.000 | 0.000 | 0.000 | 0.000 | 0.000 | 0.000 | 0.000 | 14.916 |
| 7 | 49370.276 | 0.000 | 0.000 | 0.000 | 0.000 | 0.000 | 0.000 | 0.000 | 0.000 | 49370.276 |
| 8 | 0.000 | 14.916 | 0.000 | 0.000 | 0.000 | 0.000 | 0.000 | 0.000 | 0.000 | 14.916 |
| 9 | 2454.388 | 0.000 | 0.000 | 512.420 | 0.000 | 0.000 | 0.000 | 0.000 | 0.000 | 2966.807 |
| 10 | 49638.986 | 0.000 | 0.000 | 5262.000 | 0.000 | 0.000 | 0.000 | 0.000 | 0.000 | 54900.986 |
| 11 | 49638.986 | 0.000 | 0.000 | 5262.000 | 0.000 | 0.000 | 0.000 | 0.000 | 0.000 | 54900.986 |
| 12 | 49719.599 | 0.000 | 101.473 | 5262.000 | 71.596 | 0.000 | 0.000 | 0.000 | 0.000 | 55154.668 |
| 13 | 35000.000 | 0.000 | 0.000 | 0.000 | 71.596 | 0.000 | 0.000 | 0.000 | 0.000 | 35071.596 |
| 14 | 0.000 | 0.000 | 0.000 | 0.000 | 71.596 | 0.000 | 0.000 | 0.000 | 0.000 | 71.596 |
| 15 | 35000.000 | 0.000 | 0.000 | 0.000 | 0.000 | 0.000 | 0.000 | 0.000 | 0.000 | 35000.000 |
| 16 | 15174.798 | 0.000 | 0.000 | 4749.580 | 0.000 | 0.000 | 0.000 | 315.190 | 0.000 | 20239.569 |
| 17 | 15174.798 | 0.000 | 0.000 | 5050.573 | 0.000 | 0.000 | 0.000 | 0.000 | 0.000 | 20225.371 |
| 18 | 14719.599 | 0.000 | 101.473 | 5262.020 | 0.000 | 0.000 | 0.000 | 0.000 | 0.000 | 20083.091 |
| 19 | 384.600 | 0.000 | 0.000 | 0.000 | 0.000 | 207.092 | 0.000 | 0.000 | 0.000 | 591.692 |
| 20 | 384.600 | 0.000 | 0.000 | 0.000 | 0.000 | 207.092 | 0.000 | 0.000 | 0.000 | 591.692 |
| 21 | 0.000 | 0.000 | 0.000 | 0.000 | 0.000 | 0.000 | 125.166 | 0.000 | 0.000 | 125.166 |
| 22 | 15174.798 | 0.000 | 101.473 | 4960.484 | 0.000 | 0.000 | 125.166 | 315.190 | 0.000 | 20677.111 |
| 23 | 15174.798 | 0.000 | 101.473 | 4960.484 | 0.000 | 0.000 | 0.000 | 315.190 | 0.000 | 20551.945 |
| 24 | 0.000 | 0.000 | 0.000 | 0.000 | 0.000 | 0.000 | 125.166 | 0.000 | 0.000 | 125.166 |
| 25 | 15174.798 | 0.000 | 101.473 | 411.263 | 0.000 | 0.000 | 0.000 | 5078.997 | 0.000 | 20766.531 |
| 26 | 15174.798 | 0.000 | 101.473 | 411.263 | 0.000 | 0.000 | 0.000 | 5078.997 | 0.000 | 20766.531 |

Table 4.A.5: Summary of stream contents as labeled in Figure 4.2.1, with each component in kg $h^{-1}$

| Stream | $H_2O$ | $H_2$ | $H_2O_2$ | $Na_2CO_3$ | $O_2$ | HCl | $CO_2$ | NaCl | SPC | Total |
|---|---|---|---|---|---|---|---|---|---|---|
| 27 | 15174.798 | 0.000 | 0.000 | 200.359 | 0.000 | 0.000 | 0.000 | 5078.997 | 0.000 | 20454.154 |
| 28 | 0.000 | 0.000 | 0.000 | 0.000 | 0.000 | 0.000 | 0.000 | 0.000 | 312.377 | 312.377 |
| 29 | 50174.798 | 0.000 | 0.000 | 5050.573 | 0.000 | 0.000 | 0.000 | 0.000 | 0.000 | 55225.371 |
| 30 | 47184.598 | 0.000 | 0.000 | 4749.580 | 0.000 | 0.000 | 0.000 | 0.000 | 0.000 | 51934.179 |
| 31 | 2990.200 | 0.000 | 0.000 | 300.992 | 0.000 | 0.000 | 0.000 | 0.000 | 0.000 | 3291.192 |
| 32 | 2990.200 | 0.000 | 0.000 | 0.000 | 0.000 | 0.000 | 0.000 | 315.190 | 0.000 | 3305.390 |

# 5

# CONCLUDING REMARKS

## 5.1. CONCLUSIONS

The electrochemical engineering to produce anodic $H_2O_2$ alongside cathodic $H_2$ in alkaline water electrolysis was studied using experiments, numerical analysis, and computational simulations. These findings were then used to design and analyze a scaled-up process that could convert the produced $H_2O_2$ into sodium percarbonate for final sale.

We began with exploring the behavior of ionic species in a recirculating electrolyzer system using bi(carbonate) electrolyte in Chapter 2. The typical behavior seen in experiments without reservoir recombination was an initially higher current that then roughly linearly decayed as the experiment continued, until the experiment was stopped due to electro-osmotic flow emptying the anolyte reservoir. The simulations revealed that the current in these systems is dominated by anionic migration towards the anode rather than diffusion of anionic species. However, this ionic transport is insufficient to meet the demands that the applied voltage imposes, and the electrolyte itself is consumed as a source of $OH^-$ ions for the anodic reactions. As the reactions continued, $CO_3^{2-}$ equilibrated to $HCO_3^-$ and then further to $CO_2$(g), assisted by the physical gas stripping of dissolved $CO_2$ by $O_2$ bubbles. Eventually, without remixing of electrolyte or the injection of $OH^-$ to the anolyte, the current dropped further as the reactions stalled. While the anolyte depleted of anionic species and its pH dropped to near neutral, the catholyte conversely concentrated with $OH^-$ and $Na^+$ and its pH increased. Some of the $CO_3^{2-}$ that was initially present in the catholyte is transported to the anolyte, but as the alkalinity of the catholyte increased, $CO_2$ was captured from the air and immediately converted into $CO_3^{2-}$. We would therefore expect that, in a gas-tight system, the dissolved carbon concentration would decay to zero as all of the initially present $CO_3^{2-}$ transports to the anolyte and is equilibrated away to $CO_2$(g). This work could be extended to examine other membranes, electrolyte compositions, and electrolyte concentrations, to explore other strategies for mitigating electrolyte depletion. In particular, examining the use of bipolar membranes to mitigate electrolyte depletion and how their use affects ion movement could prove valuable.

With an understanding of the ion transport dynamics in the proto-typical system, a lab-scale setup with recirculating electrolyte was constructed to produce anodic $H_2O_2$ in Chapter 3. The setup included the frequent injection of 5 M NaOH in order to maintain a supply of $OH^-$ for the anodic reactions. This lowered the amount of volume change due to electro-osmotic flow and also maintained the anodic reactions. In contrast to the setup of Chapter 2, where the $H_2O_2$ concentration sharply increased and then quickly decreased towards zero, the $H_2O_2$ concentration in this setup first increased linearly and then plateaued to a steady state value. This result is consistent with a steady generation of $H_2O_2$ with competing degradation processes that are $H_2O_2$ concentration dependent, with improved $H_2O_2$ stability due to the inclusion of $Na_2SiO_3$. The system was mathematically described using mole balances to derive analytical equations that predict the $H_2O_2$ concentrations over time given certain electrochemical and geometric parameters. The geometry of the device should be known, and a procedure was outlined to find the electrochemical parameters for any anode used. The electrochemical parameters that can be found by simple experimentation are the generation rate of $H_2O_2$ and the bulk disproportionation rate constant of $H_2O_2$ in electrolyte. The last electrochemical parameter, the rate constant of anodic oxidation of $H_2O_2$ to $H_2O$ and $O_2$, can only be found by fitting the analytical equations to a concentration curve. The derived equations were then used to make predictions as to the behavior of the system for varying reservoir volumes. As expected, using a smaller volume of electrolyte reaches steady-state more quickly at a higher concentration, but actually lowers the total amount of $H_2O_2$ product generated. This is due to anodic oxidation playing a greater role as the concentration increases. The final selections for operating current density, recirculation time, and electrolyte volumes must be balanced as longer recirculation times and higher current densities mean higher $H_2O_2$ concentrations at the expense of higher operating costs. Again, this work focused on a prototypical case using a fixed electrolyte composition and one separator material, but could also be performed with other anodes, membranes, electrolytes, or electrolyzer geometries to make more generalized expressions and compare different systems.

In Chapter 4, we combined the previous findings to design a full-scale process that both generates anodic $H_2O_2$ in alkaline water electrolysis and detailed how it might be separated for sale, an often ignored consideration by electrochemists. Because $H_2O_2$ decomposes more quickly above ambient temperature and has a boiling point greater than water, vacuum distillation is an inefficient separation technique, requiring significant energy usage to evaporate enormous amounts of water to make a concentrated $H_2O_2$ solution. It also neglects the presence of $CO_3^{2-}$ and $HCO_3^-$ ions in the resulting bottoms solution. We instead conceptualized a full separation train to convert $H_2O_2$ into sodium percarbonate by first recirculating an anolyte reservoir's content and charging it with $H_2O_2$, before crystallizing the product out as sodium percarbonate. As a result, the process runs in semi-batch operation, with batch-wise charging of $H_2O_2$ in the anolyte, but a continuously operating separation train. Analyzing the techno-economics of the full process on the basis of a 2 MW electrolyzer showed that a significant portion of the estimated capital cost is dominated by the anode price. As the base case stands, the process loses many millions

of euros per year, with an unrealistic breakeven point in terms of market capacity and electrolyzer size. Improvements to the anode cost, faradaic efficiency, $H_2$ sale price, sodium percarbonate sale price, or a combination thereof, can lead to a commercially viable process, but the targets should be realistic. For example, a faradaic efficiency to $H_2O_2$ of 100% is likely impossible given the equilibrium voltages of $H_2O_2$ generation and oxygen evolution reactions. Additionally, the process already used a premium, green $H_2$ sale price of €5 per kg. This value should ideally be much lower to compete with steam-methane reforming, which means that the overall process must have an even lower operating cost. The selection of sodium percarbonate as the valorized form of anodic $H_2O_2$ therefore requires further investigation given the current technological capabilities.

## 5.2. RECOMMENDATIONS

The majority of the literature on anodic $H_2O_2$ focuses on the electrochemistry of this reaction, but not on its application. The electrochemical engineering of the reaction reveals significant problems for increasing the technology's technology readiness level, a metric that describes the maturation of a technology from basic hypothesis to commercial production. Running the system at relevant current densities with porous separator materials inevitably leads to anolyte depletion and the migration of $CO_3^{2-}$ ions from the catholyte. It is therefore advised that future work should examine how novel components such as bipolar membranes may mitigate this issue. The recirculation of the anolyte can increase the $H_2O_2$ concentration, easing downstream separation, but this increases the operating costs. Most significantly, the separation of $H_2O_2$ for sale is a far more complex topic than previously addressed, as it entails concentrating the $H_2O_2$ along with removing the ionic species from the electrolyte. The process described in this work is not the only conceivable method for valorizing $H_2O_2$, but it demonstrates that the challenges with separation may not have solutions that enable application of the reaction.

While future research into the reaction mechanism can be useful, it does not overcome the obstacle of selling a product that may never recover the final separation costs. A better approach would be to shift research focus to exploring new process designs or separation methods for anolyte charged with $H_2O_2$. In particular, discussions with end-users of $H_2O_2$ solutions or sodium percarbonate may reveal different criteria or targets that must be met with respect to minimum concentration, minimum purity, or the presence of other ions. There may also be a premium that could be paid by the customers for this "green" $H_2O_2$, which improves the economic outlook. But the product stream specifications should be firmly established and then back calculated as to what can be achieved at the output of a paired electrolysis system. If the minimum requirements of the output stream cannot be met even in an ideal case, then the concept of offsetting the high green $H_2$ sale price by co-producing anodic $H_2O_2$ will require a new technological breakthrough. These technological breakthroughs could come in the form of novel electrolyzer geometries that avoid electrolyte depletion effects, cheaper anode materials with years-long stability, or processes designs that valorize $H_2O_2$ by a different method. Perhaps there are

other forms of $H_2O_2$ that are viable products for sale, or other applications of the co-produced $H_2O_2$ such as wastewater treatment that can use the $H_2O_2$ in-situ. But any further research into the topic should be informed by the principles of electrochemical engineering and by the deeper understanding of the process developed in this dissertation.

# BIBLIOGRAPHY


[1] Intergovernmental Panel on Climate Change. *Working Group I: The Physical Science Basis*. IPCC Sixth Assessment Report. 2021. Chap. 11.

[2] Intergovernmental Panel on Climate Change. *Working Group III: Mitigation of Climate Change*. IPCC Sixth Assessment Report. 2022.

[3] International Energy Agency. *Direct $CO_2$ emissions from primary chemical production in the Net Zero Scenario, 2010-2030*. 2023. URL: https://www.iea.org/data-and-statistics/charts/direct-co2-emissions-from-primary-chemical-production-in-the-net-zero-scenario-2010-2030-2.

[4] International Energy Agency. *$CO_2$ Emissions in 2023*. 2024.

[5] International Energy Agency. *Net Zero Roadmap: A Global Pathway to Keep the 1.5 °C Goal in Reach*. 2023.

[6] International Energy Agency. *World Energy Outlook 2025*. 2025.

[7] International Energy Agency. *Global Hydrogen Review 2025*. 2025.

[8] T. Smolinka, H. Bergmann, J. Garche and M. Kusnezoff. *Electrochemical Power Sources: Fundamentals, Systems, and Applications: Hydrogen Production by Water Electrolysis*. Elsevier, 2022. ISBN: 978-0-12-819424-9.

[9] A. Deasy-Millar, D. Fraile, M. Muron, G. Pawelec, S. Santos and O. Staudenmayer. *2025 Clean Hydrogen Monitor*. 2025.

[10] United States Department of Energy. *U.S. National Hydrogen Strategy and Roadmap*. 2023.

[11] Clean Hydrogen Partnership. *Clean Hydrogen JOINT UNDERTAKING WORK PROGRAMME 2025*. 2024.

[12] J. Ferdush, K. Nahar, T. Akter, M. J. Ferdoush, N. Jahan and S. M. F. Iqbal. 'Effect of Hydrogen Peroxide Concentration on 100% Cotton Knit Fabric Bleaching'. In: *European Scientific Journal* 15.33 (2019), pp. 254–263. DOI: 10.19044/esj.2019.v15n33p254.

[13] Q. Chen. 'Development of an anthraquinone process for the production of hydrogen peroxide in a trickle bed reactor–From bench scale to industrial scale'. In: *Chemical Engineering and Processing: Process Intensification* 47.5 (2008), pp. 787–792. DOI: 10.1016/j.cep.2006.12.012.

[14] S. Y. Park, H. Abroshan, X. Shi, H. S. Jung, S. Siahrostami and X. Zheng. '$CaSnO_3$: An Electrocatalyst for Two-Electron Water Oxidation Reaction to Form $H_2O_2$'. In: *ACS Energy Letters* 4.1 (2018), pp. 352–357. DOI: 10.1021/acsenergylett.8b02303.

[15] V. Viswanathan, H. A. Hansen and J. K. Nørskov. 'Selective Electrochemical Generation of Hydrogen Peroxide from Water Oxidation'. In: *Journal of Physical Chemistry Letters* 6.21 (2015), pp. 4224–4228. DOI: 10.1021/acs.jpclett.5b02178.

[16] S. Mavrikis, S. C. Perry, P. K. Leung, L. Wang and C. Ponce de León. 'Recent Advances in Electrochemical Water Oxidation to Produce Hydrogen Peroxide: A Mechanistic Perspective'. In: *ACS Sustainable Chemistry and Engineering* 9.1 (2021), pp. 76–91. DOI: 10.1021/acssuschemeng.0c07263.

[17] J. H. Baek, T. M. Gill, H. Abroshan, S. Park, X. Shi, J. Nørskov, H. S. Jung, S. Siahrostami and X. Zheng. 'Selective and Efficient Gd-Doped $BiVO_4$ Photoanode for Two-Electron Water Oxidation to $H_2O_2$'. In: *ACS Energy Letters* 4.3 (2019), pp. 720–728. DOI: 10.1021/acsenergylett.9b00277.

[18] T. Kang, B. Li, Q. Hao, W. Gao, F. Bin, K. N. Hui, D. Fu and B. Dou. 'Efficient Hydrogen Peroxide ($H_2O_2$) Synthesis by $CaSnO_3$ via Two-Electron Water Oxidation Reaction'. In: *ACS Sustainable Chemistry and Engineering* 8.39 (2020), pp. 15005–15012. DOI: 10.1021/acssuschemeng.0c05449.

[19] J. Baek, Q. Jin, N. S. Johnson, Y. Jiang, R. Ning, A. Mehta, S. Siahrostami and X. Zheng. 'Discovery of $LaAlO_3$ as an efficient catalyst for two-electron water electrolysis towards hydrogen peroxide'. In: *Nature Communications* 13 (2022), p. 7256. DOI: 10.1038/s41467-022-34884-4.

[20] S. Siahrostami, G.-L. Li, V. Viswanathan and J. K. Nørskov. 'One- or Two-Electron Water Oxidation, Hydroxyl Radical, or $H_2O_2$ Evolution'. In: *Journal of Physical Chemistry Letters* 8.6 (2017), pp. 1157–1160. DOI: 10.1021/acs.jpclett.6b02924.

[21] C. Xia, S. Back, S. Ringe, K. Jiang, F. Chen, X. Sun, S. Siahrostami, K. Chan and H. Wang. 'Confined local oxygen gas promotes electrochemical water oxidation to hydrogen peroxide'. In: *Nature Catalysis* 3.2 (2020), pp. 125–134. DOI: 10.1038/s41929-019-0402-8.

[22] A. Venugopal, L. H. T. Egberts, J. Meeprasert, E. A. Pidko, B. Dam, T. Burdyny, V. Sinha and W. A. Smith. 'Polymer Modification of Surface Electronic Properties of Electrocatalysts'. In: *ACS Energy Letters* 7.5 (2022), pp. 1586–1593. DOI: 10.1021/acsenergylett.2c00199.

[23] P. J. Espinoza-Montero, P. Alulema-Pullupaxi, B. A. Frontana-Uribe and C. E. Barrera-Diaz. 'Electrochemical production of hydrogen peroxide on Boron-Doped diamond (BDD) electrode'. In: *Current Opinion in Solid State and Materials Science* 26.3 (2022), p. 100988. DOI: 10.1016/j.cossms.2022.100988.

[24] S. Mavrikis, M. Göltz, S. Rosiwal, L. Wang and C. Ponce de León. 'Boron-Doped Diamond Electrocatalyst for Enhanced Anodic $H_2O_2$ Production'. In: *ACS Applied Energy Materials* 3.4 (2020), pp. 3169–3173. DOI: 10.1021/acsaem.0c00093.

[25] F. Kuttassery, S. Mathew, S. Sagawa, S. Nybin Remello, A. Thomas, D. Yamamoto, S. Onuki, Y. Nabetani, H. Tachibana and H. Inoue. 'One Electron-Initiated Two-Electron Oxidation of Water by Aluminum Porphyrins with Earth's Most Abundant Metal'. In: *ChemSuschem* 10.9 (2017), pp. 1909–1915. DOI: 10.1002/cssc.201700322.

[26] C. McDonnell-Worth and D. R. MacFarlane. 'Ion effects in water oxidation to hydrogen peroxide'. In: *RSC Advances* 4.58 (2014), p. 30551. DOI: 10.1039/c4ra05296j.

[27] A. Izgorodin, E. Izgorodina and D. R. MacFarlane. 'Low overpotential water oxidation to hydrogen peroxide on a $MnO_x$ catalyst'. In: *Energy & Environmental Science* 5.11 (2012), pp. 9496–9501. DOI: 10.1039/C2EE21832A.

[28] P.-A. Michaud, M. Panizza, L. Ouattara, T. Diaco, G. Foti and C. Comninellis. 'Electrochemical oxidation of water on synthetic boron-doped diamond thin film anodes'. In: *Journal of Applied Electrochemistry* 33 (2003), pp. 151–154. DOI: 10.1023/A:1024084924058.

[29] N. Vatistas. 'Electrocatalytic Properties of BDD Anodes: Its Loosely Adsorbed Hydroxyl Radicals'. In: *International Journal of Electrochemistry* 2012 (2011). DOI: 10.1155/2012/507516.

[30] S. Velazquez-Peña, C. Sáez, P. Cañizares, I. Linares-Hernández, V. Martínez-Miranda, C. Barrera-Díaz and M. Rodrigo. 'Production of oxidants via electrolysis of carbonate solutions with conductive-diamond anodes'. In: *Chemical Engineering Journal* 230 (2013), pp. 272–278. DOI: 10.1016/j.cej.2013.06.078.

[31] T. M. Gill, L. Vallez and X. Zheng. 'The Role of Bicarbonate-Based Electrolytes in $H_2O_2$ Production through Two-Electron Water Oxidation'. In: *ACS Energy Letters* 6.8 (2021), pp. 2854–2862. DOI: 10.1021/acsenergylett.1c01264.

[32] F. Kuttassery, A. Sebastian, S. Mathew, H. Tachibana and H. Inoue. 'Promotive Effect of Bicarbonate Ion on Two-Electron Water Oxidation to Form $H_2O_2$ Catalyzed by Aluminum Porphyrins'. In: *ChemSusChem* 12.9 (2019), pp. 1939–1948. DOI: 10.1002/cssc.201900560.

[33] T. M. Gill, L. Vallez and X. Zheng. 'Enhancing Electrochemical Water Oxidation toward $H_2O_2$ via Carbonaceous Electrolyte Engineering'. In: *ACS Applied Energy Materials* 4.11 (2021), pp. 12429–12435. DOI: 10.1021/acsaem.1c02258.

[34] D. Pangotra, L.-I. Csepei, A. Roth, V. Sieber and L. Vieira. 'Anodic generation of hydrogen peroxide in continuous flow'. In: *Green Chemistry* 24.20 (2022), pp. 7931–7940. DOI: 10.1039/d2gc02575b.

[35] A. Vass, M. Göltz, H. Ghanem, S. Rosiwal, T. Franken, R. Palkovits, G. Mul, M. N. Tsampas, G. Katsoukis and M. Altomare. 'Pulsed-Current Operation Enhances $H_2O_2$ Production on a Boron-Doped Diamond Mesh Anode in a Zero-Gap PEM Electrolyzer'. In: *ChemSusChem* 18.9 (2025), e202401947. DOI: 10.1002/cssc.202401947.

[36] I. A. Bashmakov, L. J. Nilsson, A. Acquaye, C. Bataille, J. M. Cullen, S. de la Rue du Can, M. Fischedick, Y. Geng and K. Tanaka. *Industry. In IPCC, 2022: Climate Change 2022: Mitigation of Climate Change. Contribution of Working Group III to the Sixth Assessment Report of the Intergovernmental Panel on Climate Change*. Intergovernmental Panel on Climate Change, 2022. DOI: 10.1017/9781009157926.013.

[37] B. Chang, H. Pang, F. Raziq, S. Wang, K.-W. Huang, J. Ye and H. Zhang. 'Electrochemical reduction of carbon dioxide to multicarbon ($C_{2+}$) products: challenges and perspectives'. In: *Energy & Environmental Science* 16.11 (2023), pp. 4714–4758. DOI: 10.1039/d3ee00964e.

[38] L. Li, R. P. Antony, C. Santana Santos, N. Limani, S. Dieckhöfer and W. Schuhmann. 'Anodic $H_2O_2$ Generation in Carbonate-Based Electrolytes - Mechanistic Insight from Scanning Electrochemical Microscopy'. In: *Angewandte Chemie International Edition* 63.38 (2024), e202406543. DOI: 10.1002/anie.202406543.

[39] J. A. Dean. *Lange's Handbook of Chemistry, Fifteen Edition*. McGraw-Hill, 1999. ISBN: 0-07-016384-7.

[40] H. Ito, N. Kawaguchi, S. Someya, T. Munakata, N. Miyazaki, M. Ishida and N. Akihiro. 'Experimental investigation of electrolytic solution for anion exchange membrane water electrolysis'. In: *International Journal of Hydrogen Energy* 43.36 (2018), pp. 17030–17039. DOI: 10.1016/j.ijhydene.2018.07.143.

[41] J. W. Haverkort and H. Rajaei. 'Electro-osmotic flow and the limiting current in alkaline water electrolysis'. In: *Journal of Power Sources Advances* 6 (2020), p. 100034. DOI: 10.1016/j.powera.2020.100034.

[42] G. O. Larrazábal, P. Strøm-Hansen, J. P. Heli, K. Zeiter, K. T. Therkildsen, I. Chorkendorff and B. Seger. 'Analysis of Mass Flows and Membrane Crossover in $CO_2$ Reduction at High Current Densities in an MEA-Type Electrolyzer'. In: *ACS Applied Materials and Interfaces* 11.44 (2019), pp. 41281–41288. DOI: 10.1021/acsami.9b13081.

[43] P. Mardle, S. Cassegrain, F. Habibzadeh, Z. Shi and S. Holdcroft. 'Carbonate Ion Crossover in Zero-Gap, KOH Anolyte $CO_2$ Electrolysis'. In: *The Journal of Physical Chemistry C* 125.46 (2021), pp. 25446–25454. DOI: 10.1021/acs.jpcc.1c08430.

[44] R. L. Garcia Barros, J. T. Kraakman, C. Sebregts, J. van der Schaaf and M. T. de Groot. 'Impact of an electrode-diaphragm gap on diffusive hydrogen crossover in alkaline water electrolysis'. In: *International Journal of Hydrogen Energy* 49.C (2024), pp. 886–896. DOI: 10.1016/j.ijhydene.2023.09.280.

[45] M. Ma, S. Kim, I. Chorkendorff and B. Seger. 'Role of ion-selective membranes in the carbon balance for $CO_2$ electroreduction via gas diffusion electrode reactor designs'. In: *Chemical Science* 11.33 (2020), pp. 8854–8861. DOI: 10.1039/D0SC03047C.

[46] G. O. Larrazábal, M. Ma and B. Seger. 'A Comprehensive Approach to Investigate $CO_2$ Reduction Electrocatalysts at High Current Densities'. In: *Accounts of Materials Research* 2.4 (2021), pp. 220–229. DOI: 10.1021/accountsmr.1c00004.

[47] M. Ramdin, O. A. Moultos, L. J. P. van den Broeke, P. Gonugunta, P. Taheri and T. J. H. Vlugt. 'Carbonation in Low-Temperature $CO_2$ Electrolyzers: Causes, Consequences, and Solutions'. In: *Industrial & Chemical Engineering Research* 62.18 (2023), pp. 6843–6864. DOI: 10.1021/acs.iecr.3c00118.

[48] Y. C. Li, Z. Yan, J. Hitt, R. Wycisk, P. N. Pintauro and T. E. Mallouk. 'Bipolar Membranes Inhibit Product Crossover in $CO_2$ Electrolysis Cells'. In: *Advanced Sustainable Systems* 2.4 (2018), p. 1700187. DOI: 10.1002/adsu.201700187.

[49] M. Ma, E. L. Clark, K. T. Therkildsen, S. Dalsgaard, I. Chorkendorff and B. Seger. 'Insights into the Carbon Balance for $CO_2$ Electroreduction on Cu using Gas Diffusion Electrode Reactor Designs'. In: *Energy & Environmental Science* 13.3 (2020), pp. 977–985. DOI: 10.1039/D0EE00047G.

[50] A. B. Moss, S. Garg, M. Mirolo, C. A. Giron Rodriguez, R. Ilvonen, I. Chorkendorff, J. Drnec and B. Seger. 'In operando investigations of oscillatory water and carbonate effects in MEA-based $CO_2$ electrolysis devices'. In: *Joule* 7.2 (2023), pp. 350–365. DOI: 10.1016/j.joule.2023.01.013.

[51] Q. Xu, S. Liu, F. Longhin, G. Kastlunger, I. Chorkendorff and B. Seger. 'Impact of Anodic Oxidation Reactions in the Performance Evaluation of High-Rate $CO_2$/CO Electrolysis'. In: *Advanced Materials* 36.2 (2023), p. 2306741. DOI: 10.1002/adma.202306741.

[52] J. W. Haverkort. 'Modeling and Experiments of Binary Electrolytes in the Presence of Diffusion, Migration, and Electro-Osmotic Flow'. In: *Physical Review Applied* 14.044047 (2020). DOI: 10.1103/PhysRevApplied.14.044047.

[53] P. M. v. d. Wiel, L. J. J. Janssen and J. G. Hoogland. 'ELECTROLYSIS OF A CARBONATE-BORATE SOLUTION WITH A PLATINUM ANODE-I. CURRENT EFFICIENCY AT PERBORATE CONCENTRATION OF ZERO'. In: *Electrochimica Acta* 16.8 (1971), pp. 1217–1226. DOI: 10.1016/0013-4686(71)85110-1.

[54] A. Ziogas, J. Belda, H.-J. Kost, J. Magomajew, R. A. Sperling and P. Wernig. 'Peroxodicarbonate: Electrosynthesis and first directions to green industrial applications'. In: *Current Research in Green and Sustainable Chemistry* 5 (2022), p. 100341. DOI: 10.1016/j.crgsc.2022.100341.

[55] T. Rücker, N. Schupp, F. Sprang, T. Horsten, B. Wittgens and S. R. Waldvogel. 'Peroxodicarbonate – a renaissance of an electrochemically generated green oxidizer'. In: *Chemical Communications* 60.56 (2024), pp. 7136–7147. DOI: 10.1039/d4cc02501f.

[56] T. M. Gill and X. Zheng. 'Comparing Methods for Quantifying Electrochemically Accumulated $H_2O_2$'. In: *Chemistry of Materials* 32.15 (2020), pp. 6285–6294. DOI: 10.1021/acs.chemmater.0c02010.

[57] L.-C. Weng, A. T. Bell and A. Z. Weber. 'Modeling gas-diffusion electrodes for $CO_2$ reduction'. In: *Physical Chemistry Chemical Physics* 20.25 (2018), pp. 16973–16984. DOI: 10.1039/c8cp01319e.

[58] J. W. Blake, J. T. Padding and J. W. Haverkort. 'Analytical modelling of $CO_2$ reduction in gas-diffusion electrode catalyst layers'. In: *Electrochimica Acta* 393.10 (2021), p. 138987. DOI: 10.1016/j.electacta.2021.138987.

[59] M. Ramdin, B. De Mot, A. R. T. Morrison, T. Breugelmans, L. J. P. van den Broeke, J. P. M. Trusler, R. Kortlever, W. de Jong, O. A. Moultos, P. Xiao, P. A. Webley and T. J. H. Vlugt. 'Electroreduction of $CO_2$/CO to $C_2$ Products: Process Modeling, Downstream Separation, System Integration, and Economic Analysis'. In: *Industrial & Engineering Chemical Research* 60.49 (2021), pp. 17862–17880. DOI: 10.1021/acs.iecr.1c03592.

[60] H. Zhong, K. Fujii, Y. Nakano and F. Jin. 'Effect of $CO_2$ Bubbling into Aqueous Solutions Used for Electrochemical Reduction of $CO_2$ for Energy Conversion and Storage'. In: *Journal of Physical Chemistry C* 119.1 (2014), pp. 55–61. DOI: 10.1021/jp509043h.

[61] J. A. Rabinowitz and M. W. Kanan. 'The future of low-temperature carbon dioxide electrolysis depends on solving one basic problem'. In: *Nature Communications* 11.5231 (2020). DOI: 10.1038/s41467-020-19135-8.

[62] H. H. B. Lee, A.-H. Park and C. Oloman. 'Stability of Hydrogen Peroxide in Sodium Carbonate Solutions'. In: *Tappi Journal* 83 (8 2000).

[63] D. Henkensmeier, W. Cho, P. Jannasch, J. Stojadinovic, Q. Li, D. Aili and J. O. Jensen. 'Separators and Membranes for Advanced Alkaline Water Electrolysis'. In: *Chemical Reviews* 124.10 (2024), pp. 6393–6443. DOI: 10.1021/acs.chemrev.3c00694.

[64] L. Ge, H. Rabiee, M. Li, S. Subramanian, Y. Zheng, J. H. Lee, T. Burdyny and H. Wang. 'Electrochemical $CO_2$ reduction in membrane-electrode assemblies'. In: *Chem* 8.3 (2022), pp. 663–692. DOI: 10.1016/j.chempr.2021.12.002.

[65] J. Herranz, A. Pătru, E. Fabbri and T. J. Schmidt. 'Co-electrolysis of $CO_2$ and $H_2O$: From electrode reactions to cell-level development'. In: *Current Opinion in Electrochemistry* 23 (2020), pp. 89–95. DOI: 10.1016/j.coelec.2020.05.004.

[66] B. Pan, J. Fan, J. Zhang, Y. Luo, C. Shen, C. Wang, Y. Wang and Y. Li. 'Close to 90% Single-Pass Conversion Efficiency for $CO_2$ Electroreduction in an Acid- Fed Membrane Electrode Assembly'. In: *ACS Energy Letters* 7.12 (2022), pp. 4224–4231. DOI: 10.1021/acsenergylett.2c02292.

[67] Y. Xu, R. K. Miao, J. P. Edwards, S. Liu, C. P. O'Brien, C. M. Gabardo, M. Fan, J. E. Huang, A. Robb, E. H. Sargent and D. Sinton. 'A microchanneled solid electrolyte for carbon-efficient $CO_2$ electrolysis'. In: *Joule* 6.6 (2022), pp. 1333–1343. DOI: 10.1016/j.joule.2022.04.023.

[68] C. S. Wong, P. Y. Tishchenko and W. K. Johnson. 'Solubility of Carbon Dioxide in Aqueous HCl and $NaHCO_3$ Solutions from 278 to 298 K'. In: *Journal of Chemical & Engineering Data* 50.3 (2005), pp. 817–821. DOI: 10.1021/je049716q.

[69] K. G. Schulz, U. Riebesell, B. Rost, S. Thoms and R. E. Zeebe. 'Determination of the rate constants for the carbon dioxide to bicarbonate interconversion in pH-buffered seawater systems'. In: *Marine Chemistry* 100.1-2 (2006), pp. 53–65. DOI: 10.1016/j.marchem.2005.11.001.

[70] A. A. Kulikovsky. *Analytical Modeling of Fuel Cells*. Elsevier, 2019. ISBN: 978-0-444-64222-6. DOI: 10.1016/C2018-0-01182-2.

[71] J. Newman and K. E. Thomas-Alyea. *Electrochemical Systems, Third Edition*. Wiley, 2004. ISBN: 0-471-47756-7.

[72] K. Kigoshi and T. Hashitani. 'The Self-diffusion Coefficients of Carbon Dioxide, Hydrogen Carbonate Ions and Carbonate Ions in Aqueous Solutions'. In: *Bulletin of the Chemical Society of Japan* 36.10 (1963), p. 1372. DOI: 10.1246/bcsj.36.1372.

[73] E. L. Cussler. *Diffusion: Mass Transfer in Fluid Systems*. Cambridge University Press, 1984. ISBN: 978-0-521-87121-1.

[74] S. A. M. van Stroe-Biezen, F. M. Everaerts, L. J. J. Janssen and R. A. Tacken. 'Diffusion coefficients of oxygen, hydrogen peroxide and glucose in a hydrogel'. In: *Analytica Chimica Acta* 273.1-2 (1993), pp. 553–560. DOI: 10.1016/0003-2670(93)80202-V.

[75] J. W. Haverkort. *Electrolysers, Fuel Cells and Batteries: Analytical Modelling*. TU Delft OPEN Books, 2025. ISBN: 978-94-6366-855-2. DOI: 10.59490/tb.93.

[76] S. A. Phadke, W. de Jong and J. W. Haverkort. 'An experimentally validated model for anodic $H_2O_2$ production in alkaline water electrolysis and its implications for scaled-up operation'. In: *Electrochimica Acta* 491 (2024), p. 144258. DOI: 10.1016/j.electacta.2024.144258.

[77] P. Bajpai. *Biermann's Handbook of Pulp and Paper: Raw Material and Pulp Making*. Elsevier, 2018. ISBN: 978-0-12-814240-0. DOI: 10.1016/C2017-0-00513-X.

[78] Q. Chen. 'Toward Cleaner Production of Hydrogen Peroxide in China'. In: *Journal of Cleaner Production* 14.8 (2006), pp. 708–712. DOI: 10.1016/j.jclepro.2005.03.025.

[79] A. T. Murray, S. Voskian, M. Schreier, T. A. Hatton and Y. Surendranath. 'Electrosynthesis of Hydrogen Peroxide by Phase-Transfer Catalysis'. In: *Joule* 3.12 (2019), pp. 2942–2954. DOI: 10.1016/j.joule.2019.09.019.

[80] A. J. Shih, M. C. O. Monteiro, F. Datilla, D. Pavesi, M. Philips, A. H. M. da Silva, R. E. Vos, K. Ojha, S. Park, O. van der Heijden, G. Marcandalli, A. Goyal, M. Villalba, X. Chen, G. T. K. K. Gunasooriya, I. McCrum, R. Mom, N. López and M. T. M. Koper. 'Water electrolysis'. In: *Nature Reviews Methods Primers* 2 (2022), p. 84. DOI: 10.1038/s43586-022-00164-0.

[81] C. Qu and D.-w. Liang. 'Novel electrochemical advanced oxidation processes with $H_2O_2$ generation cathode for water treatment: A review'. In: *Journal of Environmental Chemical Engineering* 10.3 (2022), p. 107896. DOI: 10.1016/j.jece.2022.107896.

[82] X. Shi, S. Siahrostami, G.-L. Li, Y. Zhang, P. Chakthranont, F. Studt, T. F. Jaramillo, X. Zheng and J. K. Nørskov. 'Understanding activity trends in electrochemical water oxidation to form hydrogen peroxide'. In: *Nature Communications* 8 (2017), p. 701. DOI: 10.1038/s41467-017-00585-6.

[83] K. Fuku, Y. Miyase, Y. Miseki, T. Gunji and K. Sayama. 'Enhanced Oxidative Hydrogen Peroxide Production on Conducting Glass Anodes Modified with Metal Oxides'. In: *Chemistry Select* 1.18 (2016), pp. 5721–5726. DOI: 10.1002/slct.201601469.

[84] Y. Miyase, S. Iguchi, Y. Miseki, T. Gunji and K. Sayama. 'Electrochemical $H_2O_2$ Production and Accumulation from $H_2O$ by Composite Effect of $Al_2O_3$ and $BiVO_4$'. In: *Journal of the Electrochemical Society* 166.13 (2019), H644–H649. DOI: 10.1149/2.0561913jes.

[85] S. Mavrikis, M. Göltz, S. C. Perry, F. Bogdan, P. K. Leung, S. Rosiwal, L. Wang and C. Ponce de León. 'Effective Hydrogen Peroxide Production from Electrochemical Water Oxidation'. In: *ACS Energy Letters* 6.7 (2021), pp. 2369–2377. DOI: 10.1021/acsenergylett.1c00904.

[86] D. Pickett. 'THE ANALYSIS OF A BATCH ELECTROCHEMICAL REACTOR WITH CONTINUOUSLY RECIRCULATING ELECTROLYTE'. In: *Electrochimica Acta* 18.11 (1973), pp. 835–837. DOI: 10.1016/0013-4686(73)85035-2.

[87] L. Li, Z. Hu, Y. Kang, S. Cao, L. Xu, L. Yu, L. Zhang and J. C. Yu. 'Electrochemical Generation of Hydrogen Peroxide From a Zinc Gallium Oxide Anode with Dual Active Sites'. In: *Nature Communications* 14 (2023), p. 1890. DOI: 10.1038/s41467-023-37007-9.

[88] M. Mohajeri, S. Shanbhag, E. Trasias, F. Mousazadeh, W. de Jong and S. A. Phadke. 'Valorization of Hydrogen Peroxide for Sodium Percarbonate and Hydrogen Coproduction via Alkaline Water Electrolysis: Conceptual Process Design and Techno-Economic Evaluation'. In: *Industrial & Engineering Chemistry Research* 64.5 (2025), pp. 2801–2815. DOI: 10.1021/acs.iecr.4c03408.

[89] L. Mosca, J. A. Medrano Jimenez, S. Assefa Wassie, F. Gallucci, E. Palo, M. Colozzi, S. Taraschi and G. Galdieri. 'Process design for green hydrogen production'. In: *International Journal of Hydrogen Energy* 45.12 (2020), pp. 7266–7277. DOI: 10.1016/j.ijhydene.2019.08.206.

[90] G. Kakoulaki, I. Kougias, N. Taylor, F. Dolci, J. Moya and A. Jäager-Waldau. 'Green hydrogen in Europe – A regional assessment: Substituting existing production with electrolysis powered by renewables'. In: *Energy Conversion and Management* 228 (2021), p. 113649. DOI: 10.1016/j.enconman.2020.113649.

[91] G. Squadrito, G. Maggio and A. Nicita. 'The green hydrogen revolution'. In: *Renewable Energy* 216 (2023), p. 119041. DOI: 10.1016/j.renene.2023.119041.

[92] B. S. Zainal, P. J. Ker, H. Mohamed, H. C. Ong, I. M. R. Fattah, S. M. Ashrafur Rahman, L. D. Nghiem and T. M. Indra Mahlia. 'Recent advancement and assessment of green hydrogen production technologies'. In: *Renewable and Sustainable Energy Reviews* 189 (Part A 2024), p. 113941. DOI: 10.1016/j.rser.2023.113941.

[93] L. Zhang, C. Jia, F. Bai, W. Wang, S. An, K. Zhao, Z. Li, J. Li and H. Sun. 'A comprehensive review of the promising clean energy carrier: Hydrogen production, transportation, storage, and utilization (HPTSU) technologies'. In: *Fuel* 355 (2024), p. 129455. DOI: 10.1016/j.fuel.2023.129455.

[94] J. Moore, J. Durham, A. Eijk, E. Karakas, R. Kurz, J. Lesak, M. McBain, P. McCalley, L. Moroz, Z. Mohamed, B. Pettinato, G. Phillippi, H. Watanabe and B. Williams. *Machinery and Energy Systems for the Hydrogen Economy*. Elsevier, 2022. ISBN: 978-0-323-90394-3. DOI: 10.1016/C2020-0-03643-1.

[95] F. Kreith and R. West. 'Fallacies of a Hydrogen Economy: A Critical Analysis of Hydrogen Production and Utilization'. In: *Journal of Energy Resources Technology* 126.4 (2004), pp. 249–257. DOI: 10.1115/1.1834851.

[96] U. Bossel. 'Does a Hydrogen Economy Make Sense?' In: *Proceedings of the IEEE* 94.10 (2006), pp. 1826–1837. DOI: 10.1109/JPROC.2006.883715.

[97] K. Wenderich, B. A. M. Nieuweweme, G. Mul and B. T. Mei. 'Selective Electrochemical Oxidation of $H_2O$ to $H_2O_2$ Using Boron-Doped Diamond: An Experimental and Techno-Economic Evaluation'. In: *ACS Sustainable Chemistry & Engineering* 9.23 (2021), pp. 7803–7812. DOI: 10.1021/acssuschemeng.1c01244.

[98] A. M. Oliveira, R. R. Beswick and Y. Yan. 'A green hydrogen economy for a renewable energy society'. In: *Current Opinion in Chemical Engineering* 33 (2021), p. 100701. DOI: 10.1016/j.coche.2021.100701.

[99] B.-J. Jesse, G. J. Kramer, V. Koning, S. Vögele and W. Kuckshinrichs. 'Stakeholder perspectives on the scale-up of green hydrogen and electrolyzers'. In: *Energy Reports* 11 (2024), pp. 208–217. DOI: 10.1016/j.egyr.2023.11.046.

[100] S. Mavrikis, M. Göltz, S. Rosiwal, L. Wang and C. Ponce de León. 'Carbonate-Induced Electrosynthesis of Hydrogen Peroxide via Two-Electron Water Oxidation'. In: *ChemSusChem* 15.4 (2021), e202102137. DOI: 10.1002/cssc.202102137.

[101] Z. Gao, Y. Cao, Q. Zhu, C. Wang, W. Bai and J. Zhu. 'Electrochemical water oxidation for hydrogen peroxide production: Focus on catalyst and reaction medium design'. In: *Journal of Environmental Chemical Engineering* 12.2 (2024), p. 111960. DOI: 10.1016/j.jece.2024.111960.

[102] Y. Jiang, P. Ni, C. Chen, Y. Lu, P. Yang, B. Kong, A. Fisher and X. Wang. 'Selective Electrochemical $H_2O_2$ Production through Two-Electron Oxygen Electrochemistry'. In: *Advanced Energy Materials* 8.31 (2018), p. 1801909. DOI: 10.1002/aenm.201801909.

[103] S. Yang, A. Verdaguer-Casadevall, L. Arnarson, L. Silvioli, V. Čolić, R. Frydendal, J. Rossmeisl, I. Chorkendorff and I. E. L. Stephens. 'Toward the Decentralized Electrochemical Production of $H_2O_2$: A Focus on the Catalysis'. In: *ACS Catalysis* 8.5 (2018), pp. 4064–4091. DOI: 10.1021/acscatal.8b00217.

[104] Y. Zhou, G. Chen and J. Zhang. 'A review of advanced metal-free carbon catalysts for oxygen reduction reactions towards the selective generation of hydrogen peroxide'. In: *Journal of Materials Chemistry A* 8.40 (2020), p. 20849. DOI: 10.1039/D0TA07900F.

[105] N. Wang, S. Ma, P. Zuo, J. Duan and B. Hou. 'Recent Progress of Electrochemical Production of Hydrogen Peroxide by Two-Electron Oxygen Reduction Reaction'. In: *Advanced Science* 8.15 (2021), p. 2100076. DOI: 10.1002/advs.202100076.

[106] H. He, S. Liu, Y. Liu, L. Zhou, H. Wen, R. Shen, H. Zhang, X. Guo, J. Jiang and B. Li. 'Review and perspectives on carbon-based electrocatalysts for the production of $H_2O_2$ via two-electron oxygen reduction'. In: *Green Chemistry* 25.23 (2023), pp. 9501–9542. DOI: 10.1039/D3GC02856A.

[107] S. C. Perry, D. Pangotra, L. Vieira, L.-I. Csepei, V. Sieber, L. Wang, C. Ponce de León and F. C. Walsh. 'Electrochemical synthesis of hydrogen peroxide from water and oxygen'. In: *Nature Reviews Chemistry* 3 (2019), pp. 442–458. DOI: 10.1038/s41570-019-0110-6.

[108] Y. Xue, Y. Wang, Z. Pan and K. Sayama. 'Electrochemical and Photoelectrochemical Water Oxidation for Hydrogen Peroxide Production'. In: *Angewandte Chemie International Edition* 60.19 (2020), pp. 10469–10480. DOI: 10.1002/anie.202011215.

[109] S. Anantharaj, S. Pitchaimuthu and S. Noda. 'A review on recent developments in electrochemical hydrogen peroxide synthesis with a critical assessment of perspectives and strategies'. In: *Advances in Colloid and Interface Science* 287 (2021), p. 102331. DOI: 10.1016/j.cis.2020.102331.

[110] S. C. Perry, S. Mavrikis, L. Wang and C. Ponce de León. 'Future perspectives for the advancement of electrochemical hydrogen peroxide production'. In: *Current Opinion in Electrochemistry* 30 (2021), p. 100792. DOI: 10.1016/j.coelec.2021.100792.

[111] D. Pangotra, L.-I. Csepei, A. Roth, C. Ponce de León, V. Sieber and L. Vieira. 'Anodic production of hydrogen peroxide using commercial carbon materials'. In: *Applied Catalysis B: Environmental* 303 (2022), p. 120848. DOI: 10.1016/j.apcatb.2021.120848.

[112] S. Li, J. Ma, F. Xu, L. Wei and D. He. 'Fundamental principles and environmental applications of electrochemical hydrogen peroxide production: A review'. In: *Chemical Engineering Journal* 452 (Part 3 2023), p. 139371. DOI: 10.1016/j.cej.2022.139371.

[113] J. Qi, Y. Du, Q. Yang, N. Jiang, J. Li, Y. Ma, Y. Ma, X. Zhao and J. Qiu. 'Energy-saving and product-oriented hydrogen peroxide electrosynthesis enabled by electrochemistry pairing and product engineering'. In: *Nature Communications* 14 (2023), p. 6263. DOI: 10.1038/s41467-023-41997-x.

[114] K. Wenderich, W. Kwak, A. Grimm, G. J. Kramer, G. Mul and B. Mei. 'Industrial feasibility of anodic hydrogen peroxide production through photoelectrochemical water splitting: a techno-economic analysis'. In: *Sustainable Energy & Fuels* 4.6 (2020), pp. 3143–3156. DOI: 10.1039/D0SE00524J.

[115] L. Li, R. Guo, S. Zhang and Y. Yuan. 'Sustainable and effective degradation of aniline by sodium percarbonate activated with UV in aqueous solution: Kinetics, mechanism and identification of reactive species'. In: *Environmental Research* 207 (2022), p. 112176. DOI: 10.1016/j.envres.2021.112176.

[116] S. J. Choi, U. S. Shin and S.-H. Kim. 'Bench-stable oxidant sodium percarbonate for functional group transformation of arylboronic acids'. In: *Tetrahedron Letters* 117 (2023), p. 154378. DOI: 10.1016/j.tetlet.2023.154378.

[117] S. Yazici Guvenc, O. K. Turk, E. Can-Güven, N. Garazade and G. Varank. 'Norfloxacin removal by ultraviolet-activated sodium percarbonate and sodium hypochlorite: process optimization and anion effect'. In: *Water Science & Technology* 87.11 (2023), pp. 2872–2889. DOI: 10.2166/wst.2023.159.

[118] L. Zhao, Y.-G. Zhao, C. Jin, D. Yang, Y. Zhang and M. Progress. 'Removal of tetracycline by ultraviolet/sodium percarbonate (UV/SPC) advanced oxidation process in water'. In: *Environmental Research* 247 (2024), p. 118260. DOI: 10.1016/j.envres.2024.118260.

[119] B. R. Insights. *Sodium Percarbonate Market Size, Share, Growth, And Industry Analysis By Type (Coated, Uncoated, Tablet) By Application (Detergent Agent, Bleaching Agent, Cleaning Agent, Water Treatment, Others), Regional Insights and Forecast From 2026 To 2035*. 2026. URL: https://www.businessresearchinsights.com/market-reports/sodium-percarbonate-market-108907.

[120] IRENA. *Green Hydrogen Cost Reduction: Scaling up Electrolysers to Meet the 1.5°C Climate Goal*. 2020.

[121] S. W. Sharshir, A. Joseph, M. M. Elsayad, A. A. Tareemi, A. W. Kandeal and M. R. Elkadeem. 'A review of recent advances in alkaline electrolyzer for green hydrogen production: Performance improvement and applications'. In: *International Journal of Hydrogen Energy* 49 (Part C 2024), pp. 458–488. DOI: 10.1016/j.ijhydene.2023.08.107.

[122] Q.-N. Ha, C.-H. Yeh, N. S. Gultom and D.-H. Kuo. 'Industrial-scale efficient alkaline water electrolysis achieved with sputtered NiFeV-oxide thin film electrodes for green hydrogen production'. In: *Journal of Materials Chemistry A* 12.1 (2024), pp. 460–474. DOI: 10.1039/D3TA05699F.

[123] Ember. *European electricity prices and costs*. URL: https://ember-energy.org/data/european-electricity-prices-and-costs/.

[124] A. P. James, G. R. Horne, R. Roesler, L. Signorini, R. Owen, S. Parvaneh, R. Pardini, S. Bigini, M. Mathes, U. Droste and P.-L. Deli. 'Process for producing sodium percarbonate'. US6231828B1. 2001.

[125] Veolia. *Handbook of Industrial Water Treatment*. URL: https://www.watertechnologies.com/handbook/handbook-industrial-water-treatment.

[126] SAMCO Technologies. *Brine Treatment Processes for Reuse or Disposal*. URL: https://samcotech.com/brine-waste-treatment-processes-for-reuse-or-disposal/.

[127] J. Harmsen, A. B. de Haan and P. L. J. Swinkels. *Product and Process Design: Driving Innovation*. De Gruyter, 2018. ISBN: 978-3-11-046774-1.

[128] H. Lang. 'Engineering approach to preliminary cost estimates'. In: *Chemical Engineering* 54 (1947), pp. 130–133.

[129] Matches. *Matches' Process Equipment Cost Estimates*. 2014. URL: https://www.matche.com/equipcost/Default.html.

[130] W. D. Seider, D. R. Lewin, J. D. Seader, S. Widagdo, R. Gani and K. M. Ng. *Product and Process Design Principles: Synthesis, Analysis and Evaluation, Fourth Edition*. Wiley, 2016. ISBN: 9781119282631.

[131] Claight Corporation (Expert Market Research). *Sodium Percarbonate Supply and Demand Analysis - Market Outlook 2026-2035*. URL: https://www.expertmarketresearch.com/industry-statistics/sodium-percarbonate-market.

[132] V. M. Caselli, J. Thieme, H. J. Jöbsis, S. A. Phadke, J. Zhao, E. M. Hutter and T. J. Savenije. 'Traps in the spotlight: How traps affect the charge carrier dynamics in $Cs_2AgBiBr_6$ perovskite'. In: *Cell Reports Physical Science* 3.10 (2022), p. 101055. DOI: 10.1016/j.xcrp.2022.101055.

[133] A. Kumar, S. Phadke and A. Bhan. 'Acetic acid hydrodeoxygenation on molybdenum carbide catalysts'. In: *Catalysis Science & Technology* 8.11 (2018), pp. 2938–2953. DOI: 10.1039/C8CY00358K.

# ACKNOWLEDGEMENTS

*If you want to go fast, travel alone; if you want to go far, travel together.*

-Proverb

I can't quite believe that this book is printed. Everyone calls the PhD a journey, and I finally understand that. It's a twisting, turning path filled with struggles, successes, failures, fascinations, ruminations, doubt, setbacks, triumphs, and everything else that comes along with great undertakings. And this journey is very different for everyone. But one common aspect is that no one can complete such an undertaking alone. Modern scientific work is just too advanced and too complicated for any one person to have all of the knowledge, skills, and capacity to execute so much work in what feels like too little time. It has taken multiple layers of teams, management, supervision, and administration for this book to be printed. A short message here is insufficient, but I'd like to thank the people that provided me so much support and assistance along the way.

I'll start by thanking my supervisors, **Wiebren de Jong** and **Willem Haverkort**. I've been told that PhD supervisors can make or break the entire experience. I don't know what I did to deserve so much luck by joining a project under your guidance, but I'm very grateful for your efforts. It was clear from the beginning that we had the same goal: to publish high-quality, necessary, scientific research, and to do so while treating everyone around us with mutual respect and integrity. My PhD began with a slow start, where I was afraid to get into the lab and try new things, lest I risk wasting time with fruitless experiments. But with your encouragement and reminders that failure itself can be an excellent teacher, I finally started improving. Then came the inevitable period of self-doubt following a lack of concrete results. And after giving me enough time to keep flapping about and trying new, wacky ideas, you began guiding me a bit more firmly to make sure I focused on where I should be. Once we started using BDD, it seemed like everything fell into place for me to study the topic from an electrochemical engineering perspective. It wasn't exactly what was set out by the project description at the beginning, but your flexibility allowed me to use everything I had learned over the past years to start outputting proper research work. At every step of the journey, I was supported both professionally and personally. You gave me the freedom to grow as a scientist, gently nudged me forward when my bad habits were slowing me down, and stood up for me as a researcher and as a co-author. This dissertation could not have been completed without you. There are always regrets about the PhD journey, but having you both as my supervisory team was never on the list.

Next I'd like to thank my committee members, **Atsushi Urakawa**, **Guido Mul**, **Paolo Pescarmona**, and **Mar Pérez-Fortes**, for taking the time to look over my dissertation and certifying that this work has met the criteria necessary for me to join their ranks. Anodic $H_2O_2$ production is only a curiosity for most electrochemistry researchers, and it costs significant time and energy to assess something only tangentially related to your field. So I want to extend my thanks for agreeing to be a part of my doctoral committee and take on that effort.

There are a few people that I shared an office with for many years that deserve special mention. **Jelmer Postma**, **Gilles Deiters**, **Iris Burgers**, and **Katie Lawrence**. I was rarely anything more than a distraction to you all, constantly interrupting to get your scientific opinion on a problem, to look at a figure, to get a coffee, to get some tea, to go for a walk, or to do just about anything that wasn't your own PhD work. You may not know it, but all those chats, walks, brainstorms, Dutch language lessons, and debates kept me sane during my PhD. I knew that if I ever needed help that I could turn to one of you, and I'm so grateful for your continued friendship. I hope I managed to at least partially return the favor. And now is a great time to thank the rest of my office mates, **Madhuri Manila**, **Shahid Khan**, **Cheng Liang**, **Anamika Ghosh**, and **Victory Abada** for their fun conversations and stories, and also to apologize for interrupting their work as the office chatter bug. **Jelmer** and **Iris**, thank you two for also agreeing to wear formal clothes on a July day and stand as my paranymphs.

I also want to thank the rest of my group, both former and current members. **Nikhilesh Kodur Venkatesh**, **Ali Yahyaee Nujukambari**, **Nico Valle Marchante**, **Davide Bordignon**, **Wouter van der Does**, **Elsa Best**, **Joe Blake**, **Aviral Rajora**, **Hadi Rajaei**, **Sofen Kumar Jena**, **Araz Sheibani Aghdam**, **Mehmet Pektas**, **Emile Craye**, and **Bart de Rooij**, it's been a pleasure to be a part of the Bubble Brigade with you all. I enjoyed our scientific discussions and our frequent lunch breaks to the Mexican food truck after group meetings. The PhD is such a solitary endeavor, but the moments as a group really made a difference for me. And **Wouter** and **Joe** deserve a special thank you for their assistance with numerical modeling. I hounded them with questions far beyond what was polite and they very kindly kept answering.

But there is another research group that I (unofficially) belonged to. I am very grateful to **Ruud Kortlever** that he allowed me to have a foot in his group for meetings, discussions, group outings, and even brief moments of supervision. There was a period when I had no idea what I needed in order to get started with experiments, and his group was very happy to offer their expertise and wisdom. I want to thank the other members of the Kortlever group, past and present, **Shilong Fu**, **Katherine Encalada Flores**, **Kevin Fernández-Caso**, **Hengameh Farahmandazad**, **Boaz Izelaar**, **Asvin Sajeev**, **Nandalal Girichandran**, **Aleksandra Misar**, **Ahmed Mohamed**, **Simone Asperti**, and **Daniël van den Berg**, for freely providing their support and knowledge. Whether it was electrochemical understanding, where to find something in the lab, or even just finding out who to talk to, they always had time for me.

I want to extend my gratitude to the members of the PhD Council and the Pro-

cess & Energy Board here in the Faculty of Mechanical Engineering at TU Delft for organizing so many interesting talks, fun activities, and opportunities for our voices to be heard. **Marko Draškić**, I am especially grateful for all of our discussions in the frame, whether it was about politics, social safety at the university, or the PhD process. It was extremely valuable for me to have someone validate what I was feeling. You never once put me down for opening up, and I hope you continue to carry that wonderful trait with you. I also want to thank my colleagues from the RELEASE consortium, especially **Onno van der Heijden**, **Maaike van Ittersum**, **Matt Peerlings**, **Bianca Ligt**, **Nadia Boulif**, **Svenja Bielefeld**, **Naveen Guruprasad**, and **Matteo Miola**, for commiserating and motivating me to keep pushing through this journey. There are too many RELEASE members to list them all, but I want you all to know that I enjoyed our consortium meetings and the chance to get to know so many motivated researchers and wonderful people. The consortium allowed me to expand my scope of knowledge beyond my narrow topic and mature as a researcher, and I am grateful for your feedback during progress presentations, where a fresh perspective can help someone who is hopelessly stuck in place. And I should thank my co-authors, **Mahdi Mohajeri**, **Shachi Shanbhag**, **Eleftherios Trasias**, and **Farzad Mousazadeh**, for their great work on the process design paper. I'm very glad that our collaboration could yield an interesting and insightful publication.

Some unsung heroes that should be mentioned include the teams of technicians and secretaries that keep all of the infrastructure in orbit: **Michel van den Brink**, **Martijn Karsten**, **Daniël van Baarle**, **Bart van der Lubbe**, **Bart Hoek**, **Eveline de Bruyn - van der Veer**, **Caroline Legierse**, and **Linda Starrenburg - Hannewijk**. Their work is rarely seen in these books, but every one of them contributed to this dissertation's completion, through advice, technical support, administration, and organization. Another name in the same category is **Ivan Buijnsters**. He lent me a small piece of BDD for some experiments, and those experiments ended up being the foundation of this entire dissertation. I wish that we could have had a full collaboration, but the timing just never aligned. Nonetheless, I appreciate your openness and enthusiasm for my project.

A few names that didn't have a direct influence on this work but still certainly helped are the ones who have supervised my past research work: **Aditya Bhan** at the University of Minnesota - Twin Cities, **Kumar Varoon Agrawal** at EPFL in Switzerland, **Tim Jones** at CSIRO in Australia, and **Tom Savenije** in the Faculty of Applied Sciences at TU Delft. Each one of these people taught me how to be a better researcher and have shaped how I approach problems, how I think about the world, and the standards that I should hold for myself as a scientist.

I want to thank my family for their support. **Dad**, **Mom**, **Pop**, **Siddharth**, and **Neha**, you guys all gave me so much encouragement and advice. Even though I'm far away, I hope you know I still love and appreciate every one of you so much. At times, it's tough for me to be separated from you all, but I hope you can see that it's worth it for the chance to grow and have wonderful opportunities here. I also want to thank my friends, both here and abroad, for their support and for listening to me whine about the PhD for the past five years. I tend to make only a few very close friends rather than many superficial friendships, and I hope you all know how much

I cherish each and every one of you. **Gerard**, **Anita**, and **Carlos**, I also appreciate your continued support through this endeavor.

There are so many more names to be mentioned. I can't possibly list them all, and for that I apologize. Everyone that I've interacted with, supervised, or studied under has taught me something. But one name that must be written here is **Laura Donk**. I have no idea how to thank you. Even with your own PhD journey to struggle through, you found your way to support me in everything I did. Professionally, personally, in my hobbies, in every which way. I'm very lucky to have a teammate like you. No one else knows how much I've gone through over these years, or how much I've grown and changed. I hope to continue doing so with you. Thank you for all you've done for me, including helping with the beautiful cover to this dissertation!

# CURRICULUM VITÆ

## Sohan Abhay Phadke

Born on the 9th of August, 1996 in Burnsville, Minnesota, United States of America

## EDUCATION

2014–2017 Bachelor of Chemical Engineering
2014–2018 Bachelor of Science in Chemistry
University of Minnesota - Twin Cities

2018–2020 Master of Science in Chemical Engineering, *cum laude*
Delft University of Technology

*Thesis:* Exploring the Synthesis and Optoelectronic Properties of $Cs_2AgSb_xBi_{1-x}Br_6$ Double Perovskites
*Supervisors:* dr. ir. Tom Savenije
dr. ir. Valentina Caselli

2021–2026 Doctor of Philosophy in Mechanical Engineering
Delft University of Technology

*Dissertation:* The Electrochemical Engineering of Anodic Peroxide Production in Alkaline Water Electrolysis
*Promotors:* Prof. dr. ir. Wiebren de Jong
dr. ir. J. Willem Haverkort

# LIST OF PUBLICATIONS

## ARTICLES RELEVANT TO THIS DISSERTATION

- S. A. Phadke, J. W. Haverkort and W. de Jong. 'Recirculating carbonate and bicarbonate based electrolyzers cannot operate continuously without in-line separation due to electrolyte depletion and ion crossover.' *(Submitted)*

- M. Mohajeri, S. Shanbhag, E. Trasias, F. Mousazadeh, W. de Jong and S. A. Phadke. 'Valorization of Hydrogen Peroxide for Sodium Percarbonate and Hydrogen Coproduction via Alkaline Water Electrolysis: Conceptual Process Design and Techno-Economic Evaluation'. In: *Industrial & Engineering Chemistry Research* 64.5 (2025), pp. 2801–2815. DOI: 10.1021/acs.iecr.4c03408

- S. A. Phadke, W. de Jong and J. W. Haverkort. 'An experimentally validated model for anodic $H_2O_2$ production in alkaline water electrolysis and its implications for scaled-up operation'. In: *Electrochimica Acta* 491 (2024), p. 144258. DOI: 10.1016/j.electacta.2024.144258

## ARTICLES OUTSIDE OF THIS DISSERTATION

- J. W. Haverkort, W. L. van der Does, M. G. H. Klein, M. C. Pektaş, S. A. Phadke, D. I. Roest and B. E. de Rooij. 'A Validated Multiphase Shunt Current Model for Alkaline Water Electrolysers.' *(In Preparation)*

## PREVIOUS ARTICLES

- V. M. Caselli, J. Thieme, H. J. Jöbsis, S. A. Phadke, J. Zhao, E. M. Hutter and T. J. Savenije. 'Traps in the spotlight: How traps affect the charge carrier dynamics in $Cs_2AgBiBr_6$ perovskite'. In: *Cell Reports Physical Science* 3.10 (2022), p. 101055. DOI: 10.1016/j.xcrp.2022.101055

- A. Kumar, S. Phadke and A. Bhan. 'Acetic acid hydrodeoxygenation on molybdenum carbide catalysts'. In: *Catalysis Science & Technology* 8.11 (2018), pp. 2938–2953. DOI: 10.1039/C8CY00358K

## CONFERENCE PRESENTATIONS

- TU Delft Research & Innovation Event: Hydrogen & Green Chemistry. Poster in Delft, the Netherlands (2024)

- 1st Electrochemical Conversion National Symposium. Presentation in The Hague, the Netherlands (2024)
- 245th Meeting of The Electrochemical Society. Presentation in San Francisco, United States of America (2024)
- 74th Meeting of the International Society of Electrochemistry. Presentation in Lyon, France (2023)